

**Embeddable Wireless Strain Sensor**  
**Based on RF Resonant Cavity for**  
**Civil Structural Health Monitoring Applications**

By

**Jenny Chuang**

A thesis

submitted to the Faculty of Graduate Studies

in partial fulfillment of the requirements

for the degree of

**Master of Science**

Department of Electrical and Computer Engineering

University of Manitoba

June 2004

© Jenny Chuang

**THE UNIVERSITY OF MANITOBA**  
**FACULTY OF GRADUATE STUDIES**  
\*\*\*\*\*  
**COPYRIGHT PERMISSION**

**Embeddable Wireless Strain Sensor Based on RF Resonant Cavity for Civil Structural  
Health Monitoring Applications**

**BY**

**Jenny Chuang**

**A Thesis/Practicum submitted to the Faculty of Graduate Studies of The University of  
Manitoba in partial fulfillment of the requirement of the degree  
Of  
MASTER OF SCIENCE**

**Jenny Chuang © 2004**

**Permission has been granted to the Library of the University of Manitoba to lend or sell copies of this thesis/practicum, to the National Library of Canada to microfilm this thesis and to lend or sell copies of the film, and to University Microfilms Inc. to publish an abstract of this thesis/practicum.**

**This reproduction or copy of this thesis has been made available by authority of the copyright owner solely for the purpose of private study and research, and may only be reproduced and copied as permitted by copyright laws or with express written authorization from the copyright owner.**

## Abstract

In this thesis we describe a new type of strain sensor which can be used to measure strain in civil structures. This strain sensor is a passive resonant cavity that can be embedded in a structure with an antenna attached. Changes in strain will by definition change dimensions of the sensor cavity, and hence change the sensor's resonant frequency. The resonant frequency of this device can be remotely interrogated using RF signals. Such a system has the advantage of requiring no permanent physical connection between the sensor and the data acquisition system. The design presented here is a coaxial cavity resonator that exhibits electromagnetic resonance for wavelengths two times its cavity length and operates at a frequency of approximately 2.4 GHz, and exhibits a shift in resonance of 2.4 kHz per microstrain. Methods of noise reduction are presented including time domain gating in the detector circuit and also using phase sensitive detection techniques. A power budget and error calculations are presented demonstrating that noise limits can still be improved upon. Experimental results have shown high linearity, low hysteresis, and a strain resolution of better than 1 microstrain with a bandwidth of 30 Hz on this sensor. Strain tests have also shown good agreement with measurements from metal foil strain sensors. This new class of embeddable sensor will have application in monitoring the health of and assessing damage in civil structures.

## Acknowledgements

First, I would like to gratefully acknowledge the support and guidance of my advisor, Dr. Douglas Thomson for his patience, understanding, and supervision in the pursuit of this degree. Without whom, I don't think I would have ever considered the idea of pursuing graduate studies. I would like to thank you for easy going nature, your encouragement, and your willingness to let me learn on my own. Also, I'm grateful to you for having a sense of humour, and making sure that I didn't end up as a squeegee kid on the corner of River and Osborne... (And just for the record, I never did go to Hawaii...) As well, I would like to acknowledge the assistance that I received from other faculty and staff in the ECE department, including, but not limited to Professors Greg Bridges and Lot Shafai, technicians Al Symmons, Al McKay, and office staff Karin, Marcia, and Judy. As well, I would like to thank ISIS Canada and the technicians in the Department of Civil Engineering at the University of Manitoba for their cooperation and assistance in embedding and testing of the sensors in concrete. I also want to thank my family and friends for supporting me in this endeavour. A huge thank you for your helping hands, for being understanding, and for not being (too) offended when I was not (ever?!) the most pleasant person to be around due to lack of sleep, or lack of time due to the never ending stream of deadlines. And last but not least, I would like to acknowledge the financial support of the NSERC and Iders in supporting this research project.

## Table of Contents

Abstract .....	1
Acknowledgements .....	3
Table of Contents .....	4
List of Figures .....	6
List of Tables.....	10
Chapter 1 - Introduction.....	11
1.1    Background to Structural Health Monitoring (SHM).....	12
1.2    Current Strain Sensors.....	15
1.3    Wireless Sensors .....	18
1.3.1    Active Wireless Sensors.....	18
1.3.2    Surface Acoustic Wave (SAW) Devices.....	21
1.3.2.1    SAW Wireless Sensor .....	25
1.3.3    Inductively Coupled Wireless Sensor .....	30
1.3.3.1    Inductively Coupled Strain Sensor.....	31
1.3.3.2    Other Applications of Inductively Coupled Wireless Sensors.....	32
1.4    Wireless Strain Sensing System Under Investigation.....	33
Chapter 2 - Sensor .....	37
2.1    Resonance .....	37
2.2    Transmission Lines .....	38
2.2.1    Transmission Line Parameters .....	39
2.2.2    Resonant Transmission Lines .....	44
2.3    Resonant Cavities.....	47
2.4    Sensor Used in this System .....	48

2.4.1	Capacitive Coupling Effect on Sensor Cavity .....	52
2.4.2	Transmission Line Model of Sensor Cavity.....	54
2.4.2.1	Equivalent Lumped Circuit Model.....	65
2.5	Compression Test.....	69
2.5.1	Press Fit Sensor .....	71
2.5.2	Welded Sensor .....	73
2.6	Sensor Installation.....	75
2.7	Chapter Summary.....	76
Chapter 3 - Interrogation System for Wireless Sensing.....		78
3.1	Basic Interrogation System .....	79
3.2	Gated Interrogation system .....	86
3.2.1	Effects of Increasing Time Delay Between Switches.....	94
3.2.2	Signal Level vs. Antenna Separation Distance .....	97
3.2.3	Measuring Q with Effects of Coupling Capacitance.....	101
3.3	Phase Sensitive Detection .....	106
3.3.1	Calculation of System Resolution.....	113
3.3.2	Measured Resolution.....	117
3.4	Results from Compression Test .....	120
3.5	Chapter Summary.....	123
Chapter 4 - Conclusions and Future Work.....		124
References .....		129
Appendix A .....		135

## List of Figures

Figure 1.1 Two implementations of wireless infrastructure for sensing networks [26].	19
Figure 1.2 – Surface wave propagating will mechanically deform the material. [38].	22
Figure 1.3 Simple IDT configuration for SAW generation on piezoelectric substrate showing finger period $p$ [41].	23
Figure 1.4 Two port SAW sensing device.	26
Figure 1.5 Two port SAW used in conjunction with impedance varying classical sensor [47].	28
Figure 1.6 One port SAW sensing device [41].	28
Figure 1.7 Time domain separation of request pulse and RF response from SAW device [41].	30
Figure 1.8 Applied strain on the structure deforms the solenoidal inductor [56].	31
Figure 1.9 Diagram of a MEMs based inductively coupled pressure sensor with planar inductor and diaphragm based capacitor [58].	33
Figure 1.10 Schematic of strain sensing system based on RF coaxial cavity resonator.	34
Figure 2.1 – Electric circuit representing a small section of transmission line with length $\Delta z$ [67].	40
Figure 2.2 – Typical TEM transmission lines include coaxial, two wire, and planar configurations showing physical dimensions necessary for distributed parameter calculations [64].	41
Figure 2.3 – Transmission line of characteristic $\gamma$ and $Z_0$ , showing input impedance at the input ( $z=0$ ), and at an arbitrary point on the line.	44
Figure 2.4 – Diagram of shorted transmission line of various lengths and equivalent input impedance [68].	46
Figure 2.5 - Diagram of transmission line with E and I shown for shorted and open circuit ends and equivalent resonant circuit [68].	47
Figure 2.6 – Diagram of resonant cavity sensor under strain and resulting effects on resonant frequency.	50
Figure 2.7 – Shop drawing of coaxial cavity resonator construction.	51
Figure 2.8 - Photograph of a resonant cavity sensor.	51
Figure 2.9 – Plot of $S_{11}$ for varying connector depth into resonant cavity under constant strain.	53
Figure 2.10 – Equivalent circuit model of coaxial cavity resonator.	54
Figure 2.11 – Diagram of total input impedance $Z_{IN}$ from the connector of the resonant cavity when coaxial cavity sensor is modeled as a coupling capacitor ( $Z_C$ ) and two shorted transmission lines ( $Z_{SC}$ ).	57
Figure 2.12 – Plot of transmission line model of resonant cavity with varying input capacitance.	59

Figure 2.13 – Plot of measured data vs. modeled results showing significantly lower Q in measured results. .....	61
Figure 2.14 – Figure showing 3 dB bandwidth used for calculations of Q for comparing measured and modeled results. ....	62
Figure 2.15 – Plot of transmission line model with of resonant cavity with varying input capacitance and additional R losses. ....	63
Figure 2.16 – Plot showing measured data vs. augmented model showing improved agreement. ....	64
Figure 2.17 – Plot of simulated natural response for equivalent lumped RLC circuit for cavity resonator. ....	69
Figure 2.18 – Casting of sensor in concrete cylinder .....	71
Figure 2.19 – $-S_{11}$ of resonant cavity as read from network analyzer showing predicted effects of compressive strain. ....	71
Figure 2.20 – Plot of frequency vs. strain for press fit sensor. ....	72
Figure 2.21 – Plot of frequency vs. strain for welded sensor compared to press fit sensor. ....	74
Figure 2.22 – Plot of max frequency shift with max strain for first 5 cycles. ....	75
Figure 2.23- Photograph showing sensor installation in scale model bridge deck. ....	76
Figure 3.1 – Block diagram of the basic interrogation system discussed. ....	80
Figure 3.2 – Signal at nodes N1 and N2 as marked in the block diagram. ....	80
Figure 3.3 – Figure showing expected time domain signal from the RF detector. ....	82
Figure 3.4 – Plots of (normalized) typical output signal of the RF detector. ....	83
Figure 3.5 – Block diagram of basic interrogation system with low pass filter. ....	84
Figure 3.6 – Plot of typical output signal of low pass filter over a range of frequencies. ....	85
Figure 3.7 – Plot showing time domain signal from RF detector with and without sensor connected. ....	86
Figure 3.8 – Block diagram of circuit and control signals for time domain gating. ....	87
Figure 3.9 – Time domain signals at nodes N1 and N2 and N3 as marked in the block diagram showing effects of time domain gating. ....	88
Figure 3.10 – Photograph of interrogation system and experimental setup. ....	88
Figure 3.11 – Block diagram showing use of HP 8011A pulse generator for timing control of two switches. ....	89
Figure 3.12 – Diagram showing TTL control signals for the two switches and the resulting signals at N2 and N3 as marked on the block diagram using a HP 8011A pulse generator. ....	90
Figure 3.13 – Diagram showing TTL control signals for the two switches and the resulting signals at N2 and N3 as marked on the block diagram using a HP 8016A word generator. ....	91
Figure 3.14 – Plot showing environmental noise at output of RF detector with and without gating. ....	92
Figure 3.15 – Plot showing time domain signal from RF detector output with and without gating. ....	93

Figure 3.16 – Plot showing frequency sweep of sensor without gating, and with gating showing results much closer to ideal .....	94
Figure 3.17 – Composite plots of frequency sweeps with increasing time delay .....	95
Figure 3.18 – Plot of maximum amplitude vs. gating delay showing inverse exponential relationship.....	96
Figure 3.19 – Composite plot showing effect of increasing separation distance between two antennae. All y-axis in mV, all x-axis span 2.4 GHz to 2.44 GHz sweep.....	98
Figure 3.20 – Plot of maximum amplitude vs. antenna separation distance (in air) showing inverse $x^4$ relationship.....	99
Figure 3.21 – Plot of maximum amplitude vs. antenna separation distance (in air) showing inverse $x^4$ relationship for far field region only. ....	100
Figure 3.22 – Plot of detector output through low pass filter with varied pin depth. Frequency decreases with increasing pin depth (increased coupling capacitance). ....	102
Figure 3.23 – Plot showing 3 dB and full width half max thresholds and bandwidths. ....	103
Figure 3.24 – Plot showing data normalized and inverted before and after smoothing filter.....	104
Figure 3.25 – Plot of output bandwidth for pin depth. Frequency decreases with increasing pin depth (increased coupling capacitance). ....	105
Figure 3.26 – Plot of Q for varying pin depth. Frequency decreases with increasing pin depth (increased coupling capacitance).....	105
Figure 3.27 – Block diagram of the interrogation system modified to use phase sensitive detection techniques using a lock-in amplifier. ....	107
Figure 3.28 – Diagram of sinusoidal frequency modulation. ....	108
Figure 3.29 – Diagram of FM rate.....	108
Figure 3.30 – Figure showing frequency modulation effect of detector output through low pass filter.....	109
Figure 3.31 – Figure showing time domain output signal of RF detector through low pass filter with FM modulation applied to signal. ....	109
Figure 3.32 – Figure showing frequency spectrum of RF detector signal with FM modulation. ....	110
Figure 3.33 – Diagram of changing $f_{mod}$ with respect to peak of detector power curve and effects on time domain output of detector and frequency spectrum of output signal. ....	111
Figure 3.34 – Figure showing magnitude of low frequency component $f$ of detector output signals for varying values of $f_{mod}$ .....	112
Figure 3.35 – Block diagram showing typical output of low pass filter and lock-in amplifier for a wideband sweep in frequencies. ....	113
Figure 3.36 – Diagram of square wave frequency modulation on RF signal. ....	114
Figure 3.37 – Plot of lock-in amplifier output with 100 kHz steps in input RF frequency. Gated system showing much lower signal level, but improved signal to noise ratio. ....	118

Figure 3.38 – Plot of background noise measurement vs. time constant on lock-in amplifier with theoretical noise limits.....119

Figure 3.39 – Photograph of equipment set up for compressive load test of sensor with measurements obtained using wireless interrogation system. ....120

Figure 3.40 – Plot showing typical output from the lock-in amplifier and metal foil strain gauge plotted together showing good agreement between measurements (negative values indicate compressive strain).....121

Figure 3.41 – Plot of strain measurement from wireless interrogation system plotted vs. metal foil strain gauge measurement.....122

## List of Tables

Table 2.1 Distributed coaxial line parameters for high frequency signals [63].	41
Table 2.2 – Table summarizing Q measured from 3 dB bandwidths for measured results, t-line model, and augmented loss t-line model.	64
Table 3.1 – Summary of calibration test for lock-in output with 100 kHz steps in input frequency.	118

## Chapter 1 Introduction

The purpose of this thesis is to investigate a novel strain measuring system for use in civil Structural Health Monitoring (SHM) applications. SHM is a major interdisciplinary research area that involves collaboration between industry, government policymakers, and researchers in civil, mechanical, electrical and computer engineering. An SHM system is denoted by the ability to detect and interpret adverse changes in a structure in an attempt to reduce life-cycle costs and to improve reliability of the structure [1] by detecting and localizing damage in a structure, estimating the extent of damage, and predicting the residual life of the structure.

Strain is a unitless quantity which is defined by an object's change in length over its nominal length. This quantity in particular is of interest in civil infrastructure because it is a fundamental measure of structural performance. It provides information as to how well a structure is able to support itself and the extra load applied to it under cyclic loading conditions [2]. As SHM products are gradually progressing from demonstration projects into engineering practice, it is becoming evident that having sensors which are suitable for use in civil applications is crucial to their successful deployment and integration. Civil requirements for a SHM system demand a robust sensor which can be easily handled on a construction site, withstand the pouring and curing of concrete, tolerate the freeze thaw cycle of seasonal changes [3], with an overall lifespan that can meet or exceed that of the

structure in which it is to be used. Ideally a strain sensor should offer an unambiguous measurement of strain with high resolution over a range of several hundred microstrain. The system should provide information that is useful and easy to use, be comprised of widely available low cost technology, have low manufacturing and deployment costs, be scalable, allow for many sensors to be integrated to provide sufficient data for modeling and analysis of the structure, and have minimal power requirements [4].

The scope of this thesis will involve devising, constructing, testing, and validating a prototype wireless strain sensing system that would be suitable and viable for use in civil infrastructure monitoring applications.

### ***1.1 Background to Structural Health Monitoring (SHM)***

New civil engineering construction is the world's largest industry – accounting for more than 10% of the world's gross domestic product [4]. Currently, civil infrastructure investment in the United States alone is estimated to be over \$25 trillion [5]. However, these investments are rapidly deteriorating due to overuse, overloading, age, and damage from natural hazards [4]. Of the 40,000 bridges in Canada, approximately 40% will need to be replaced in the next 10 to 20 years. In the United States, approximately 50% of bridges were constructed prior to the 1940's, and of those, between 35% [6] to 42% are now considered to be structurally deficient [7] - requiring repair, reinforcing, widening or replacement. Of the approximately 600,000 bridges in the US, roughly 10,000 bridges are constructed, rehabilitated, or replaced each year [8].

This deterioration is not a phenomenon that is isolated to the United States or North America. The deterioration of civil infrastructure in North America, Europe, and Japan [7] has been well documented and publicized. Part of the problem is the increasing demands of bearing capacity and traffic loads that in many cases, exceeds original design plans [9]. This plight is also mirrored in other countries such as Korea [10] and Columbia [11], where catastrophic failures within the past decade have brought the situation to public attention.

Because of the importance of civil infrastructure on the economical life of a country, governments have put considerable resources into repairing and maintaining them. In 2003, the Safe, Accountable, Flexible and Efficient Transportation Equity Act (SAFTEA) in the US allocated US\$179 billion to highway and safety programs and US\$22 billion for bridge replacement and rehabilitation over a six year period.

The coincidence of expiring lifespan of current structures, and newly available technology has allowed governments to investigate tools which can enhance life cycle performance and decrease the maintenance costs of new civil infrastructure. For this reason, governments have demonstrated interest in implementing SHM systems in these structures as they repair and replace them. The numerous reasons include being able to localize and quantify any degradation and/or damage to a structure such that the structure's reliability, performance, safety, residual service life and life cycle costs can be

accurately assessed. Information could be obtained regarding structural safety for use under various conditions such as high axle loads and high wind conditions, and whether the structures remained sufficiently stable after fractures appear and earthquakes occur.

Currently, the predominant method of structural assessment still relies on visual inspection by trained technicians. This is costly, inefficient, and highly prone to error. Use of SHM systems may enable a reduction of scheduled inspections while improving the efficiency and accuracy of maintenance. In many cases, serious damage is not visually obvious, and impossible to determine without destructive methods. This was demonstrated after the Hyogoken-Nambu earthquake in 1995, where many of the structure's supporting piles were severely damaged although the superstructure on top did not show any serious flaws [12]. As well, employing SHM would allow designers and engineers to more fully understand loading effects of structures – enhancing future designs.

Several long term monitoring projects have already evolved into SHM systems in place in several locations world wide including North America, Japan [12-14], Hong Kong, Europe [9,15], China [16], and Taiwan [17] amongst others [18]. Global governments may eventually pass legislation that requires the implementation of SHM as a cost effective measure of validating design specifications, as well for assessing structural performance, servicing requirements, and residual lifetime. Singapore's current program of major infrastructure upgrades already includes a provision for SHM in tender

specifications – making it the contractor’s responsibility to provide satisfactory evidence of performance improvement [18].

At present, some of the key obstacles to widespread adoption of SHM include the lack of suitable sensing systems for easy deployment, and the high costs of implementation.

## **1.2 Current Strain Sensors**

Metal foil, fiber optic and vibrating wire sensors are currently the predominant strain sensor products used for civil SHM. Metal foil strain sensors are small, thin, metallic devices whose electrical resistance changes with applied strain. In order to measure strain with these sensors they are typically connected to a Wheatstone Bridge [27] - an electric circuit that is capable of measuring the minute changes in resistance corresponding to strain. Though resistance is a quantity that is easy to measure, one of the significant drawbacks of metal foil sensors is their susceptibility to effects such as corrosion and gas diffusion over long periods of time. As these effects will also affect their electrical resistance, the accuracy of this sensor’s strain measurements will decrease over time.

A vibrating wire strain gauge consists of a tensioned steel wire between two end blocks that are bonded, welded, or embedded in a structure. A vibrating wire is read by using voltage pulses in a magnetic assembly located at the center of the wire. The magnet ‘plucks’ the wire like a guitar string and then measures the resulting frequency of

oscillation. As the structure undergoes strain, the tension in the wire will change – resulting in a change in the resonant frequency of the wire. The advantages of vibrating strain gauges are their insensitivity to electrical noise, capability for operation of the sensor in wet operating conditions, and capability of signal transmission over long distances without extensive loss of signal.

Fiber optic sensors, meanwhile, measure strain by detecting variations of laser wavelengths entering and exiting a glass fiber. There are numerous ways of using fiber optic sensors for strain measurement, including Brillouin scattering [19], Fiber Bragg Grating (FBG), and SOFO (Surveillance d'Ouvrages par Fiber Optiques) [13], to name just a few techniques. Fiber optic sensors have recently garnered a lot of attention because of several inherent advantages that include resistance to corrosion, and insensitivity to electromagnetic interference (EMI). Additionally, the sensors are very compact and very sensitive [20-22]. However, they are expensive, and fragile. Typical costs of a fiber interrogation system are between \$40,000 and \$60,000. The maximum sweep speed of a tunable or variable wavelength laser also imposes an upper limit on the strain measurement rate of a few hundred Hz [23] which is insufficient for some applications.

Existing sensors' operating deficiencies are dwarfed by their installation costs, which is currently a chief constraint to widespread SHM adoption. Metal foil and fiber optic sensor both require that the sensors be physically bonded to the structure. This time

consuming work requires expensive skilled labour and disrupts construction activity. The biggest disadvantage to metal foil, vibrating wire, and fiber optic sensors is that they must all be physically connected to their interrogators. This necessitates the laying of large amounts of conduit to carry and organize the cables connecting the sensor and the interrogation unit and then manually pulling the cables through the conduit. The structure design must further include a designated location where all the cables exit the structure and connect to an interrogation system. This location requires a power supply for the interrogator and must also be accessible to field technicians. Because all cables exit a single area, clear documentation must identify the individual sensors. Field installations have shown that the cost of installing the conduit and cables can more than double the combined costs of the actual sensors and interrogation system. For example, the cost of installing a monitoring system in the Tsing Ma suspension bridge in Hong Kong was reported to be over \$27,000 per sensor channel [24].

For both metal foil and fiber optic sensors, because an adhesive material sits between the sensors and the strained surface, the installation is sensitive to creep due to degradation of the bond, temperature influences, and hysteresis caused by thermo-elastic strain [25]. Despite all this cost and effort, the sensors may debond from the concrete during the surrounding structure's long lifetime, rendering them useless. The connections themselves are also susceptible to damage from weathering, wear, and moisture, and, in colder climates, ice as well. Additionally, the wired connection is also the subject of

added complexities when servicing or repairing sections of the structure because they are prone to damage [26].

A wireless strain system eliminates many of the costs and complexities introduced by physical connections by completely separating the sensor from the interrogator.

### **1.3 Wireless Sensors**

Obviously, wireless technology can present many advantages over wired systems. As in the case of cordless and cellular telephones, television and stereo remote controllers, wireless internet connectivity, and even some computer mice and keyboards, freedom from wires can provide convenience by adding flexibility and relaxing constraints on the user. However, in the absence of an inexhaustible portable power supply, constraints in battery life leads to heightened interest in passive sensors for situations where lifespan are concerns. In this section, a brief discussion of current wireless sensing technologies is presented. This discussion will cover active and passive devices including Surface Acoustic Wave (SAW) based and Radio Frequency (RF) sensors.

#### **1.3.1 Active Wireless Sensors**

Wireless sensing systems can be achieved by simply connecting a wireless transceiver to a sensor node – making use of currently existing wireless communications channels such as Cellular Digital Packet Data (CDPD) or General Packet Radio Service (GPRS) [28] for long range transmission and Bluetooth or Wireless Ethernet [24] for short range

transmission. The sensor node communicates with a base station or receiver which can accumulate and process the data provided by the sensor.

These wireless networks can operate by having sensors physically connected to a simple, rugged Data Acquisition System (DAQ) which then communicates wirelessly to the central host as shown in Figure 1.1a, or with individual sensors and transmitters and a single host receiver which interrogates the sensors locally as shown in Figure 1.1b [26] with the wireless advantage in the former being limited as it still suffers from many of the same problems that plague wired sensor networks.

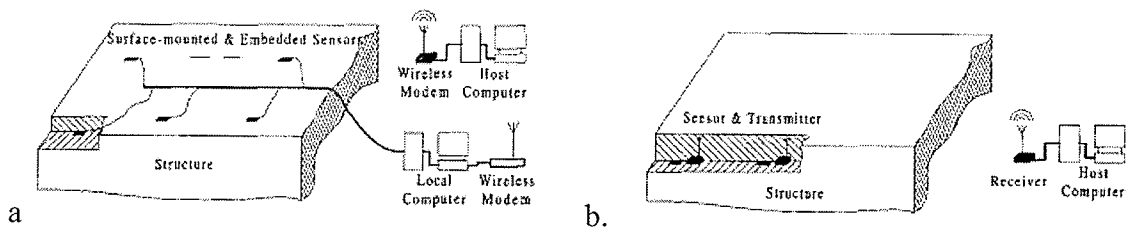


Figure 1.1 Two implementations of wireless infrastructure for sensing networks [26].

The larger problems of this system include supplying power to the transmitter, and the large amounts of data which must be passed through a wireless communication channel, which is a highly power intensive process when data quantities and transmission distances are large [29]. As well, it is computationally intensive for a single unit to deal with large amounts of data provided by several data acquisition nodes [30]. A method of dealing with this is to add computational capabilities at each of the nodes – allowing data to be pre-processed and decimated before being sent to the main data acquisition system [31]. However, this requires that complex circuitry with computational capabilities exist

at each node [32,33]. As well, loss of information in the processing and decimation may hinder subsequent analysis of significant events.

This kind of system might be appropriate for applications where power supply is readily available in the sensor's general vicinity, and wireless communication is only implemented as a method of simplifying consolidated data collection - such as the case for monitoring vibrations on light standards [24] or traffic flow [28]. However, in the cases where a power supply is not readily available, either by design omission, or because the sensor is a retrofitted sensing system on an existing structure, using existing wireless infrastructure is not a very practical solution as the system would necessitate the heavy use of battery power [24,32]. As battery technology has not advanced to the point where electronic transmission devices can run continuously for years without replacement of the power supply [34], this can pose a huge problem for sensors that are embedded in inaccessible locations such as in bridges, roadways and subway systems.

It is not a economically viable, nor is it an environmentally attractive option to implement wireless sensing at the cost of continually replacing batteries. Because it is not always possible to provide a constant supply of power to the sensor node, research in wireless sensing has looked towards extending sensor life by reducing power requirements for the wireless transceiver units. These efforts have included reducing the operating voltage of the circuitry, reducing the clock frequency in the microchip, making energy aware

systems that can make intelligent processing and transmission decisions [34]. and reducing power through the use of sleep modes [24].

As well, interest has been demonstrated in the development of alternative methods of powering circuitry. Some techniques which have been investigated include using inductive coupling to send power to the sensor by the continuous or periodic transmission of an RF signal from a nearby source [3,35], and also systems which scavenge power from the environment [36,37].

### **1.3.2 Surface Acoustic Wave (SAW) Devices**

Acoustic wave devices are fabricated to generate mechanical waves that propagate through (Bulk Acoustic Wave), or along the surface (Surface Acoustic Wave) of a solid material. Surface acoustic waves were first characterized in 1885 by Lord Raleigh as waves could be propagated over the plane boundary between a linearly elastic half-space and a vacuum (or a sufficiently rarefied medium such as air) [38] as a hypothesis to the effects of earthquakes. This prediction was confirmed in the 1920's with the invention of the seismograph.

Also known as Raleigh waves, surface acoustic waves travel along the surface of the material. These waves are comprised of a longitudinal and vertical shear component that can couple with a medium in contact with the device's surface – allowing the use of such a device as a sensing element. The amplitude of surface acoustic waves decays

exponentially with depth, with virtually all of the acoustic energy confined within a one wavelength distance from the materials surface. The mechanical deformation of the material is shown in Figure 1.2. The vertices in the lattice show where material particles would have been equidistant horizontally and vertically in the absence of wave motion [38].

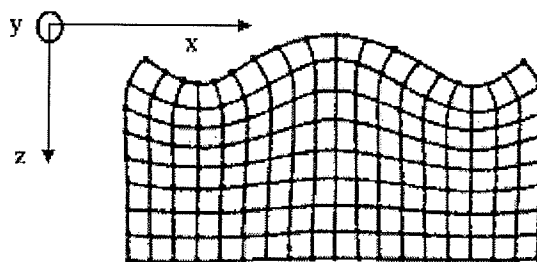


Figure 1.2 – Surface wave propagating will mechanically deform the material. [38]

Electronic SAW devices are produced by patterning an Interdigital Transducer (IDT) onto a piezoelectric substrate. A piezoelectric material is one that generates an electric charge when mechanically deformed [39,40]. Conversely, when an external electric field is applied, the piezoelectric materials will mechanically deform. The IDT allows mechanical oscillations to be induced in the material with application of a AC electrical signal to the conductor on the material's surface.

The simplest IDT's are composed of periodically spaced planar metal lines with alternate lines connected via a common bus bar. The bus bar provides the electrical input to the IDT. These devices can operate as wireless devices if the signal is coupled into the IDT bus bar via an attached antenna. An illustration of a simple IDT is shown below in Figure

1.3 (left), with a cross sectional view shown to the right. Because the IDT is a simple planar structure on top of the surface, it can be patterned by photolithographic process standard to IC fabrication; making fabrication of these devices relatively inexpensive.

Applying a DC voltage to the two bus bars will generate a static electrical field between alternate IDT fingers, stimulating an elastic deformation in the piezoelectric material as shown in Figure 1.3 (right). If an AC voltage is applied to the bus bars, an oscillating harmonic deformation is generated, resulting in elastic surface waves radiating out of the transducer in a direction normal to the electrodes. Conversely, the IDT can also be used to sense surface acoustic waves. An acoustic wave entering an IDT will generate an oscillating electrical potential in the IDT, and therefore an electrical RF output signal between the two electrode combs. If an antenna is connected to the bus bars, the RF signal will be coupled into free space where it can be picked up by a receiver.

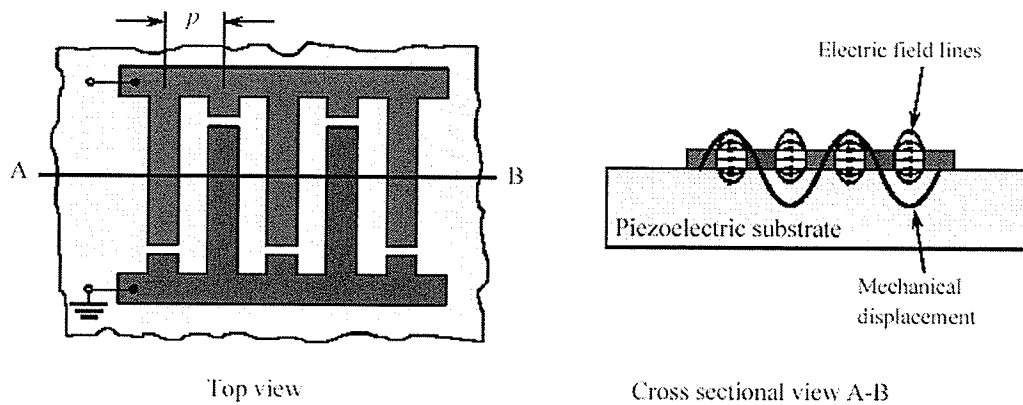


**Figure 1.3 Simple IDT configuration for SAW generation on piezoelectric substrate showing finger period  $p$  [41].**

Typical piezoelectric substrates for SAW devices are Quartz ( $\text{SiO}_2$ ), Lithium Niobate ( $\text{LiNbO}_3$ ) and Lithium Tantalite ( $\text{LiTaO}_3$ ) [41], as well as gallium arsenide (GaAs), zinc oxide (ZnO) and lead zirconium titanate (PZT) [43]. The acoustic loss in these materials is nearly negligible at 434 MHz, but at 2.45 GHz, the loss of SAW on Quartz or Lithium tantalite is extremely high [41]. For this reason, typical SAW devices operate in the 25-500 MHz range. Typical SAW amplitudes are approximately 1 nm [42,43], with wavelengths that range from 1 – 100 microns.

The efficiency of the IDT for generating and receiving surface waves is a maximum when the finger period  $p$  coincides with one half of the acoustic wavelength [41]:

$$\lambda = v_{ph}/f \tag{1.1}$$

where  $v_{ph}$  is the phase velocity of the wave. Hence, the fundamental resonance, or synchronous, frequency of the IDT for a given substrate is dependant only on the interdigital period  $p$ , and is given by the expression:

$$f_0 = v_{ph}/2p \tag{1.2}$$

Changing the length, width, position or thickness of the IDT will change the operating characteristics of the SAW device.

### 1.3.2.1 SAW Wireless Sensor

Surface Acoustic Wave (SAW) devices have shown great promise for a variety of wireless sensing applications. These applications include but are not limited to sensing pressure, force, temperature, strain, torque, pH, electric fields, chemical vapours, and humidity [44-54]. The achievable device access rate is  $10^5$  readings/s, with a range of a few meters. This allows SAW devices to be used for communication and sensing in fast moving objects or vehicles, such as in monitoring braking wheel temperatures of trains, as well as pressure and friction in automobile tires [41]. A complete wireless sensor system consists of a passive (SAW) transponder and a local Radio Frequency (RF) transceiver working as reader or interrogator unit.

To begin, an RF burst transmitted by the interrogator is received by the antenna of the (SAW) transponder. The antenna is typically a dipole, loop, or patch configuration [41]. The received RF energy is coupled into the IDT of the SAW device where it generates a surface wave that will propagate for some distance through the material before being transformed back into RF form and retransmitted to the radio transceiver. Small changes in the propagation path by physical phenomenon will be reflected in wave properties such as amplitude, velocity, phase and frequency [45], which can be detected and interpreted in the returned RF signal.

SAW sensors can be one port or two port devices. In a two port configuration, the IDTs are placed at opposite ends of the SAW device. One IDT generates the surface wave, and the other IDT receives the wave and transforms it back to an RF signal.

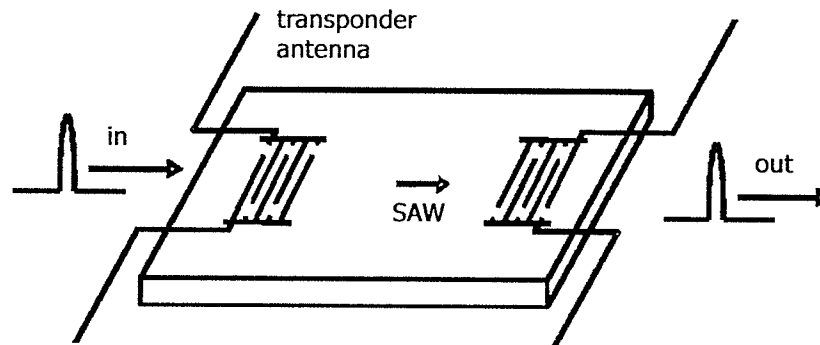


Figure 1.4 Two port SAW sensing device

Amplitude, frequency, phase, and time delay of the RF response are affected by properties of the SAW propagation mechanism. As SAW velocities are strongly influenced by factors such as pressure and temperature, they can be used to sense both. To separate the two effects, temperature sensors are contained in hermetically sealed packages to remove the effects of mass loading and pressure changes. These temperature sensors have been shown to have millidegree resolution, good linearity, and low hysteresis [42]. To compensate for temperature changes in a pressure sensor, a second SAW device is located in close proximity but isolated from the stresses acting on the pressure sensor. The effects of temperature can then be effectively subtracted out from the overall reading, resulting in a temperature compensate pressure sensor.

SAW propagation is also highly sensitive to mass loading on the surface of the material. This can be exploited to form particulate, thickness and chemical vapour sensors. Coating the surface of the SAW device with an adhesive material can cause any particulate landing on the surface to remain in place, perturbing wave propagation. In the case of film thickness sensors, the surface is uncoated, but left exposed in a film deposition chamber. As the device frequency is proportional to the mass of the deposited film, the sensor provides data by measuring the deposition rate of mass on its surface. Chemical vapour sensors operate on the same principle. However, in this case, the surface of the sensor is again coated with a material that will selectively absorb or react with vapours of interest which again results in mass loading or unloading of the sensor [42].

Two port SAW devices can also be used in conjunction with a conventional sensor where the output will vary impedance [47] as shown below in Figure 1.5. In this configuration, the load impedance acts as a variable reflector. Changes in properties of the external sensor will result in varying impedance of the IDT, changing the acoustic reflection properties. In some configurations, the impedance can vary from almost infinity in the open circuit case to almost zero in the short circuit case.

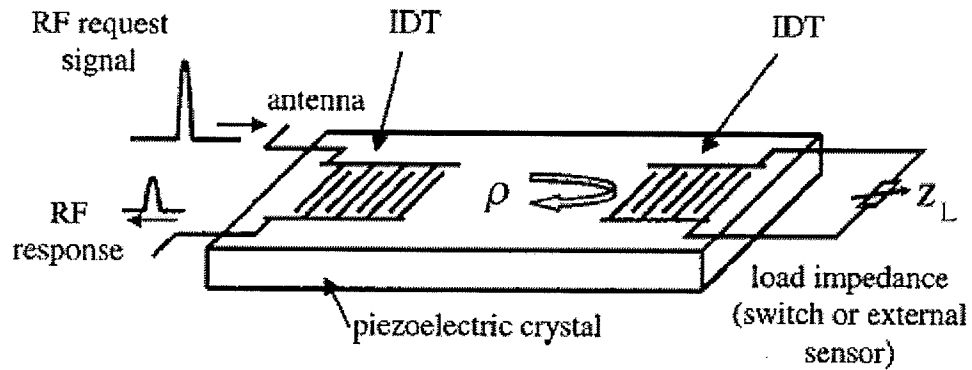


Figure 1.5 Two port SAW used in conjunction with impedance varying classical sensor [47]

In a one port device, also known as Reflective Delay Line device, the IDT is located at one end of the device. Reflective lines are placed such that as the surface waves propagate in one direction, they are partially reflected at each reflector. When the reflected wave returns to the source IDT it is transformed back into an RF signal and returned to the interrogator as shown below in Figure 1.6.

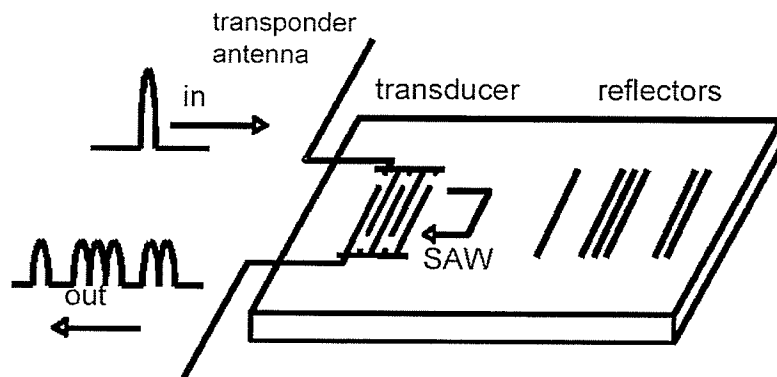


Figure 1.6 One port SAW sensing device [41]

This response signal contains information about the number and relative position of reflectors as well as the propagation properties of the SAW wave. This is a popular use of SAW devices because it allows easy integration of sensor tagging.

In some cases, the entire function of the SAW device is ID tagging. With a sufficiently large number of reflectors, a unique identification sequence can be coded through their placement on the SAW device. In this way, devices can be uniquely identified by a particular sequence of reflected pulses. This idea has been implemented in the form of “smart cards” for keyless entry systems, automobiles for toll collection in Norway, parts tracking in automobile production lines and also subway car identification in Germany [41].

Other applications of reflective delay lines for sensing systems include monitoring temperature, force, displacement, torque, pressure amongst many others. Temperature measurement can be accomplished by measuring the phase difference between the first and last reflection. Torque pressure, and displacement measure changes in the reflected signal due to changes in the surface propagation length and elasticity constants.

One problem with using SAW devices as wireless sensors is separation of the interrogation system from the response signal. However, because SAW waves travel very slowly compared to RF signals in free space, this can be accomplished by time domain separation as shown below in Figure 1.7.

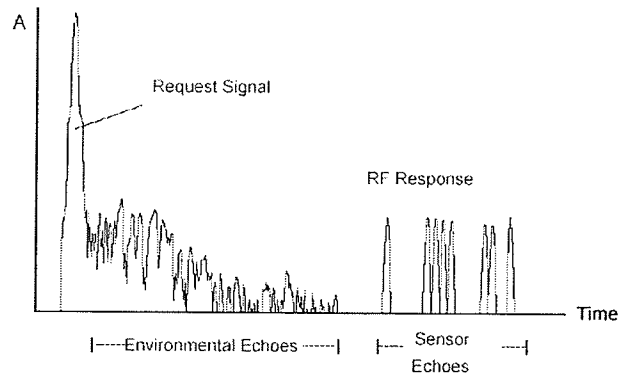


**Figure 1.7 Time domain separation of request pulse and RF response from SAW device [41]**

Although SAW sensing devices have demonstrated low cost, high sensitivity, reliability, ruggedness and remarkable versatility [42], they are not appropriate for all situations. Civil applications demand that devices and sensors can be protected from weathering, wear and damage over a prolonged lifespan. One way of accomplishing this is by embedding devices into the concrete structure itself. However, it is logistically difficult to envision how a SAW device might be put into practice in civil SHM systems.

### **1.3.3 Inductively Coupled Wireless Sensor**

Inductive coupling is defined as the transfer of energy between two circuits through a shared magnetic field [55]. The two devices may be part of a single unit such as the primary and secondary sides of a transformer, or separated as in the case of two antennas on a transmitter receiver pair. In some cases, inductive coupling is an undesirable effect (such as crosstalk in circuits), and in others, such as this, it is a highly desirable quality enabling a wireless connection for sensing capabilities.

Wireless sensors have been developed based on inductive coupling between an embedded sensor and an external detector antenna. In some cases, inductive coupling is used simply to remotely power microsensors integrated with microelectronics [3].

When inductive coupling is used as a sensor, the systems typically involve the use of a resonant LC sensing circuit where either the inductance [56] or capacitance [57-59] of the circuit changes with the physical parameter being measured. This will result in changes the overall resonant frequency of the sensor circuit which can be easily detected and measured. Effectively, the sensor will act as a filter for an incoming radio wave [59]. This type of sensing network exists in many forms with various detection schemes.

### 1.3.3.1 Inductively Coupled Strain Sensor

A stress field causing strain on a structure can also deform a capacitor or inductive coil of an embedded LC circuit. In one implementation, the sensor is a hollow, core-less multi-turn solenoidal inductor 1.5 cm in diameter, soldered to a fixed bulk capacitor designed to be used in monitoring of composite structures [56]. Applied strain on the structure deforms the inductive coil from its nominal circular shape as shown below in Figure 1.8.

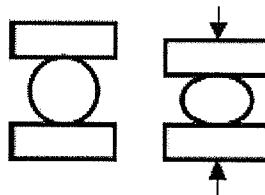


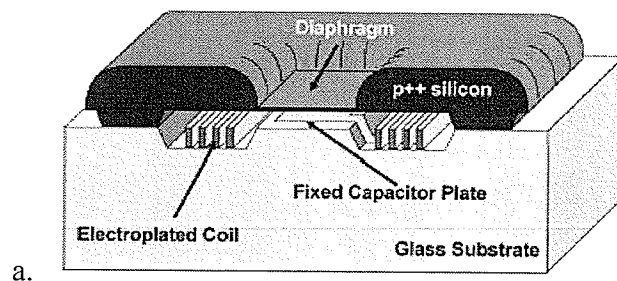
**Figure 1.8** Applied strain on the structure deforms the solenoidal inductor [56].

In this example, a gate dip meter used to detect changes in the resonant frequency of the sensor. A gate dip meter operates by sweeping an RF signal over a fixed frequency band while monitoring RF power. A LC circuit in close proximity to the meter will absorb a portion of the RF power at its resonant frequency – resulting in a measurable dip in the meter’s level. The measured value can then be used to calculate change in dimension of the inductor, and hence applied strain.

Another implementation of a strain sensor has been designed for monitoring strain in a automobile tire by detecting change in capacitance between steel wires embedded in the tire [59]. This system made use of a telemetric system for detection of resonant frequency.

### 1.3.3.2 Other Applications of Inductively Coupled Wireless Sensors

Other examples of inductively coupled sensors include small IC and MEMs based devices with variable capacitance in the LC circuit. For example, a wireless capacitive pressure sensor can be fabricated using a diaphragm based capacitor with planar coil as shown in Figure 1.9. [58].



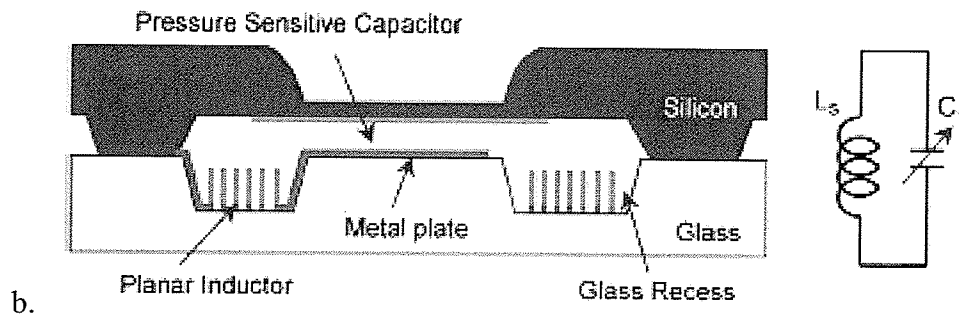


**Figure 1.9** Diagram of a MEMS based inductively coupled pressure sensor with planar inductor and diaphragm based capacitor [58].

A design based on a planar inductor and a variable capacitance Interdigital Capacitor (IDC) has also been demonstrated [57]. By coating the IDC with specific materials, change in dielectric constant and hence capacitance can be observed with the effects of temperature, humidity, complex permittivity, chemical agents and biological growth such as yeast or bacteria cultures in a way directly analogous to SAW devices.

In general, inductively coupled wireless sensors can be made with an embedded LC circuit and external circuit to determine resonant frequency. Resonant frequency can be determined by impedance meters, inductive telemetry systems, and/or dip meter type devices.

#### **1.4 Wireless Strain Sensing System Under Investigation**

The focus of this thesis will be a wireless, passive strain sensing device based on a RF coaxial cavity resonator. Changes in strain are measured through shifts in the sensor's resonant frequency. A simplified diagram of the system's operation is shown below in Figure 1.10. Similar to SAW devices, this sensor is interrogated by first sending an RF

request signal, and then measuring the sensor response to the request. The theoretical basis of the sensor's operation and the relationship between applied strain and the sensor's frequency response will be discussed in Chapter 2.

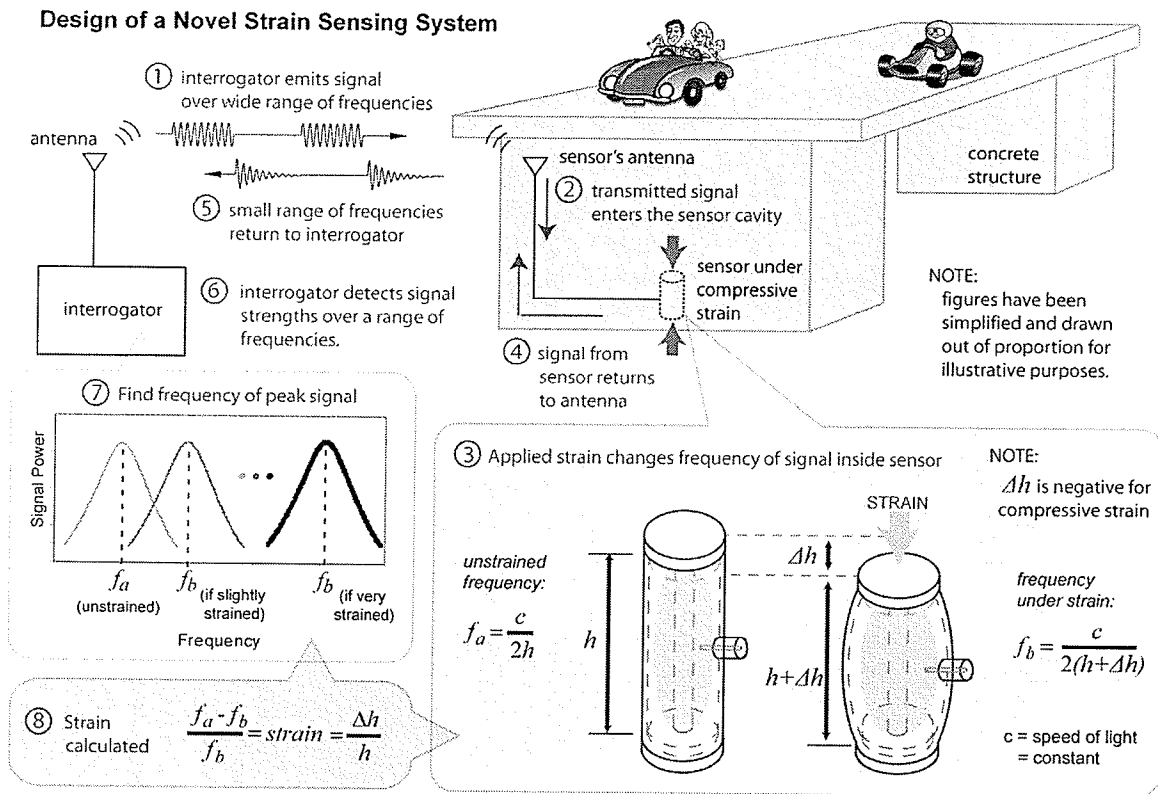


Figure 1.10 Schematic of strain sensing system based on RF coaxial cavity resonator.

This novel design leads to several unique advantages. Unlike metal foil strain sensors that measure strain indirectly through change in resistance, the resonant cavity sensor measures strain by measuring a fundamental change. Because the resonant frequency of the sensor is only a function of cavity length, and a fundamental constant, we can see that the effects of temperature, and humidity will have a minimal effect on the sensor's accuracy. Unlike laser sources, RF signals can be generated easily and accurately [60],

we can see that almost all sources of measurement drift have been accounted for and removed. The standard electronic components employed by this system are much more economical than their optical counterparts and can be purchased from vendors who supply cellular phone manufacturers. Parts are therefore inexpensive, reliable, and readily available. This overall system is robust, easy to implement and protect, and will have low deployment and maintenance costs.

Because the interrogator is detached from the structure under measurement, it can be developed independently and is not required to last as long as the sensors. The interrogator can also be updated to profit from newer and cheaper technology. This is advantageous because the interrogator is the most complex and expensive part of the system.

The prototype sensors are passive, so power connections are not required. Bonding is not required because the concrete conforms around the sensor when it is cast, and it transfers strain from the structure to the sensor once it sets. Installation involves simply placing the sensors in the desired position and orientation. With the appropriate choice of material, sensors can easily be expected to outlive the surrounding structure.

This design's scalability is one of its key benefits. Because it is inherently portable, a single interrogation system can be used to service multiple sites. This sensor system is economical regardless of the size of infrastructure being monitored because the sensors

are inexpensive and installation costs are expected to be much lower than for currently existing technologies. The cost of monitoring structures using existing systems, in contrast, increases non-linearly with size due to the complexities involved in laying conduit and organizing cables. The wireless sensors can also be installed individually, so they can be either added to the structure during initial construction or added and gradually updated in repair and retrofit projects. Although a single sensor failure might reduce the amount of data obtainable from a structure, it will not necessitate the choice between replacing or losing data from entire sections, which would typically occur in fiber optic systems.

This thesis will focus on sensor characterization and development of a wireless interrogation system. Although a preliminary investigation into antennas which can be embedded with the sensor has conducted, it will not be discussed in this thesis.

## Chapter 2      Sensor

The strain sensor under development is a simple RF resonant cavity. The sensor has been specifically designed such that the cavity resonates at convenient microwave frequencies. It can be connected to an antenna and hence signals can be transmitted and received from it remotely. This chapter will first cover a general explanation of resonators and resonant cavities. A theoretical basis of the sensor design in this strain sensing system will be presented along with a model of the sensor showing expected results. As well, details of the sensor's use, performance, and installation procedure will be discussed.

### **2.1 Resonance**

Resonance is a condition that can be found in electrical, mechanical and optical systems. It is characterized by a system's behavior in response to input energy of various frequencies, and particularly the frequency at which an input signal will result in maximum amplitude. In the case of a driven system, this point is marked by maximum power transfer to the system and an increasing amplitude of the output up to a steady state condition where the oscillations continue with constant amplitude [61, 62, 63, 64].

Quality factor, or Q factor, is a measure of how resonant a system is. For a high Q circuit, it is most often defined as  $2\pi$  times the ratio of mean stored energy over the energy loss

per cycle of oscillation [61], and can be measured as the product of resonant frequency in radians/second, and the time constant describing the decay rate of power in the system.

Systems and devices which exhibit resonance are called resonators. In electronics, a resonant circuit is a combination of frequency sensitive elements connected in such a way as to provide a frequency selective response [65]. Electrical resonators are used in many applications including filters, oscillators, frequency meters, tuned amplifiers and for energy storage [63]. A basic electronic resonator is composed of either a series or parallel arrangement of two reactive elements – inductance and capacitance. Depending on the resonant frequencies desired, these elements can be in the form of discrete inductors and capacitors, or may exist in distributed form in a transmission line of specific length.

## ***2.2 Transmission Lines***

Later in this chapter, a transmission line model will be used to describe the behaviour of the sensor. In this section, a brief introduction to transmission line theory is presented. Transmission lines are a means of guiding energy propagation between a source and a load [64]. Transmission lines that consist of two or more conductors in parallel can support waves where the electric field and magnetic field are both perpendicular to the direction of wave propagation. These waves are known as Transverse Electro Magnetic (TEM) waves, and are uniquely defined by voltage, current and characteristic impedance [63]. Typical TEM transmission lines include two wire, coaxial line and planar lines, wire above conducting line, and microstrip lines (Figure 2.2). Of particular interest are coaxial

lines which consist of a central insulated conductor mounted inside a tubular outer conductor. The chief advantage of a coaxial line is minimal radiation losses as compared to two wire and planar transmission lines because electrical and magnetic fields are contained within the outer conductor and do not extend into space.

Ordinary circuit analysis with discrete elements requires that the physical dimensions of each component be much smaller than the electrical wavelength transmitted through them. That is, the wavelength must be large enough that there is insignificant phase variation of the wave propagating across the dimensions of the component.

Microwave frequencies encompass signals between 300 MHz and 300 GHz which correspond to electrical wavelengths of 1 m and 1 mm respectively. At these frequencies, the signal wavelength can be on the same scale as the dimensions of components and connecting lines. Hence, the magnitude and phase of the voltage and current waves can vary significantly over the length of the transmission line. A simple conductor will exhibit effects of inductance, resistance, capacitance and conductance, and therefore lumped element models are insufficient to describe their behaviour.

### **2.2.1 Transmission Line Parameters**

To describe the effects of microwave propagation through a conductor, a distributed transmission line model can be used. In a distributed model, the effects of resistance,

capacitance, inductance and conductance are spread along the transmission line and are given as per unit length quantities. These parameters are described as follows [64]:

$R$  = resistance in both conductors per unit length in  $\Omega /m$

$L$  = inductance in both conductors per unit length in  $H/m$

$G$  = conductance of the dielectric media per unit length in  $S/m$

$C$  = capacitance between the conductors per unit length in  $F/m$

The behaviour of a small segment of the transmission line with the length  $\Delta z$  can then be approximated with an electric circuit (Figure 2.1) with component values described by the parameters  $R$ ,  $L$ ,  $G$  and  $C$ .

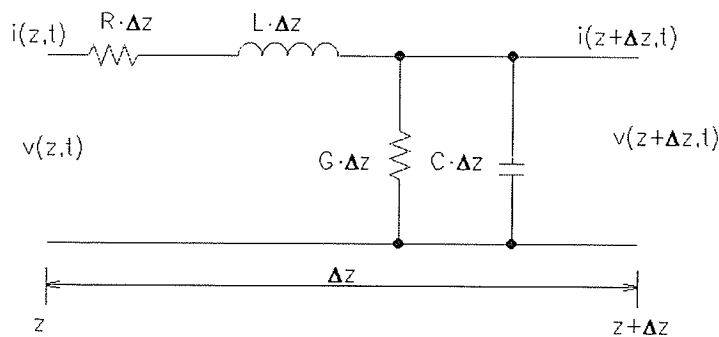


**Figure 2.1** – Electric circuit representing a small section of transmission line with length  $\Delta z$  [67].

The values of these parameters can be calculated from the physical dimensions and material properties of the transmission line. Equations governing these values for coaxial transmission lines are summarized in Table 2.1 where the dimensions are shown in Figure 2.2. With the exception of the distributed resistance, and hence loss, each of the parameters can be determined independently of the operating frequency.

Parameter	Coaxial Line	Units
R = Series Resistance	$\frac{1}{2\pi\delta\sigma_c} \left[ \frac{1}{a} + \frac{1}{b} \right]$ given that: $(\delta \ll a, c - b)$	( $\Omega/m$ )
L = Series Inductance	$\frac{\mu_d}{2\pi} \ln \frac{b}{a}$	(H/m)
G = Shunt Conductance	$\frac{2\pi\sigma_d}{\ln \frac{b}{a}}$	(S/m)
C = Shunt Capacitance	$\frac{2\pi\epsilon_d}{\ln \frac{b}{a}}$	(F/m)
$\delta$ = Skin Depth	$\delta = \frac{1}{\sqrt{f\pi\mu_c\sigma_c}}$	(m)

Table 2.1 Distributed coaxial line parameters for high frequency signals [63].

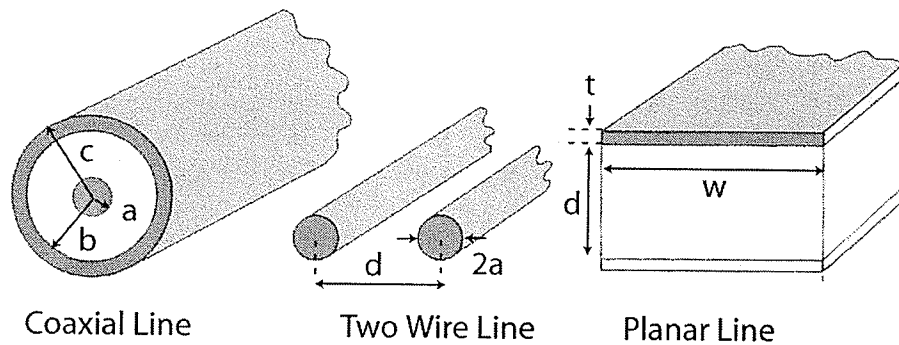


Figure 2.2 – Typical TEM transmission lines include coaxial, two wire, and planar configurations showing physical dimensions necessary for distributed parameter calculations [64].

For a coaxial line, the dimension  $a$  is the radius of the center conductor,  $b$  is the inner radius of the outside conductor, and  $c$  is the outer radius of the outer conductor. The quantity  $\epsilon_d$  is the electrical permittivity of dielectric separating the two conductors. In this case  $\epsilon_d$  is equal to the permittivity of free space  $\epsilon_0$  since there is no dielectric between the

two conductors. The constants  $\sigma_c$ , and  $\mu_c$  refer to the conductivity and magnetic permeability of the center conductor respectively, and  $\sigma_d$ , and  $\mu_d$  refer respectively to the conductivity and permeability of the dielectric between the two conductors. Skin depth of the conductor is denoted by  $\delta$ , which represents the depth of the current carrying portion in the conductor.

Knowing the parameters of R, L, G and C for an arbitrary transmission line is sufficient to describe wave propagation characteristics along the line. Specifically, the characteristic impedance of the line,  $Z_0$ , and a complex wave propagation constant  $\gamma = \alpha + j\beta$  can be determined if the distributed parameters and the input frequency are known. Having these values allows instantaneous values of current and voltage to be found for a point on any length of transmission line if boundary conditions are known. Characteristic impedance is defined by the ratio of forward traveling voltage to current waves at any point on the transmission line, and can be found by the following equation [64]:

$$Z_0 = \sqrt{\frac{R(\omega) + j\omega L}{G + j\omega C}} \quad (2.1)$$

where  $R(\omega)$  indicates that R is a frequency dependant quantity. The propagation constant and can be similarly calculated from the values of the distributed parameters using the equation:

$$\gamma = \alpha + j\beta = \sqrt{(R(\omega) + j\omega L)(G + j\omega C)} \quad (2.2)$$

where  $\alpha$  and  $\beta$  represent the real and imaginary parts of  $\gamma$  respectively. The real component represents the attenuation constant of the wave propagating through the transmission line, and the imaginary portion represents the phase constant of the traveling wave. A special case of the transmission line exists when  $R = G = 0$ . In this case, the attenuation factor of the propagation constant is also zero, and no losses occur in the line and hence the special case is termed “lossless”. However, since losses and signal power are of importance to a wireless sensing system, the general case of a “lossy” transmission line will be considered.

The voltage at an arbitrary point on the transmission line can be expressed as the sum of a forward and reverse traveling wave [63, 64] as:

$$V_s(z) = V_o^+ e^{-\gamma z} + V_o^- e^{+\gamma z} \quad (2.3)$$

where  $V_o^+ e^{-\gamma z}$  and  $V_o^- e^{+\gamma z}$  represent the waves traveling in the  $+z$  and  $-z$  directions respectively, and  $V_s(z)$  is the phasor form of  $v(z,t)$ , where  $v(z,t)$  is the voltage at time  $t$  on the point  $z$  on the transmission line. The current at a point on the transmission line can be similarly expressed as:

$$I_s(z) = I_o^+ e^{-\gamma z} + I_o^- e^{+\gamma z} \quad (2.4)$$

and  $V_s$  and  $I_s$  are related through the  $Z_0$  by the relationship:

$$\begin{aligned}
 I_o^+ &= \frac{V_o^+}{Z_o} \\
 I_o^- &= \frac{V_o^-}{Z_o}
 \end{aligned}
 \tag{2.5}$$

Hence, with  $\gamma$  and  $Z_o$ , the behaviour of a transmission line can be fully described.

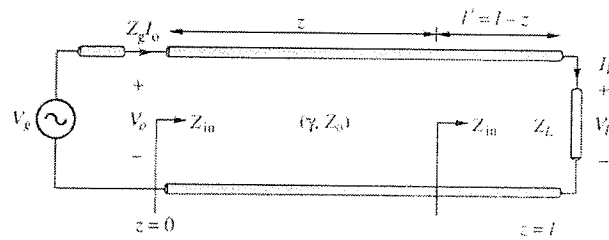


Figure 2.3 – Transmission line of characteristic  $\gamma$  and  $Z_o$  showing input impedance at the input ( $z=0$ ), and at an arbitrary point on the line.

Considering a transmission line of length  $\ell$  that is characterized by  $\gamma$  and  $Z_o$  that is inserted in a circuit between the source and a load of impedance  $Z_L$  (Figure 2.3), for the general case, the input impedance into the transmission line is given by the equation [63,64]:

$$Z_{in} = Z_o \left[ \frac{Z_L + Z_o \tanh(\gamma \ell)}{Z_o + Z_L \tanh(\gamma \ell)} \right]
 \tag{2.6}$$

## 2.2.2 Resonant Transmission Lines

Considering again the transmission line of length  $\ell$ , A voltage reflection coefficient  $\Gamma_L$  is defined by the ratio of the reverse traveling wave to the incident voltage wave at the end of the line and is given as:

$$\Gamma_L = \frac{V_o^- e^{+\gamma l}}{V_o^+ e^{-\gamma l}} \quad (2.7)$$

and can be found by the equation:

$$\Gamma_L = \frac{Z_L - Z_o}{Z_L + Z_o} \quad (2.8)$$

If a section transmission line is terminated with a load that is equal to its characteristic impedance  $Z_o$ , all power is transferred from the transmission line to the load, and zero reflection occurs at the junction of the two. Therefore, the voltage reflection coefficient at the load ( $\Gamma_L$ ) is zero. When the transmission line is not terminated in  $Z_o$ , the incident energy that is not transmitted or absorbed is reflected back along the transmission line and hence results in a non-zero reflection coefficient. Reflections will occur on all transmission lines of finite length that are not terminated by an impedance equal to their  $Z_o$ . A resonant line exists where standing waves in voltage and current result from the combination of incident and reflected waves.

Considering a shorted line of various lengths (Figure 2.4), we can see that at the shorted end, voltage potential must be at a minimum and current must be at a maximum. Therefore, working towards the generator, for a fixed wavelength input, we can see that at  $\lambda/4$  multiples in length, a standing waves in both current (dashed line) and voltage (solid line) will be produced on the transmission line. Therefore we can see how a transmission line can be a resonant element.

The same effects can also be seen for a open circuit waveform, however, in this case, at the open circuit, voltage potential is a maximum and current is a minimum. The equivalent circuit of the lossless cases for an open circuit and short circuit transmission line are shown (Figure 2.5).

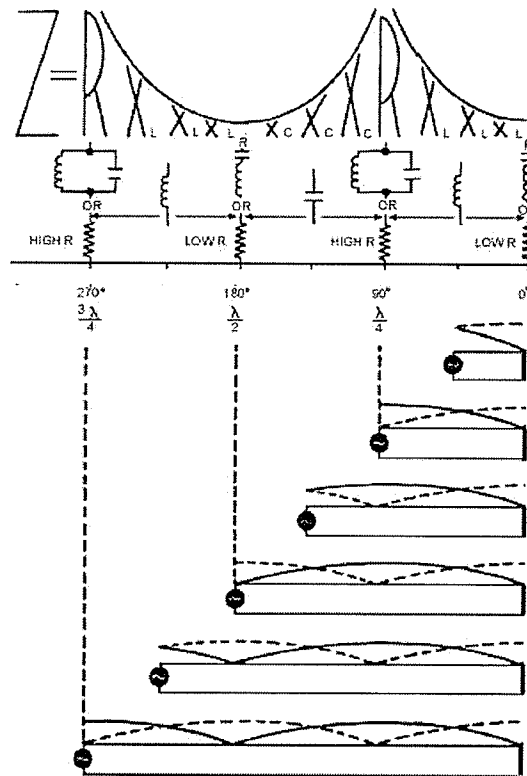


Figure 2.4 – Diagram of shorted transmission line of various lengths and equivalent input impedance[68].

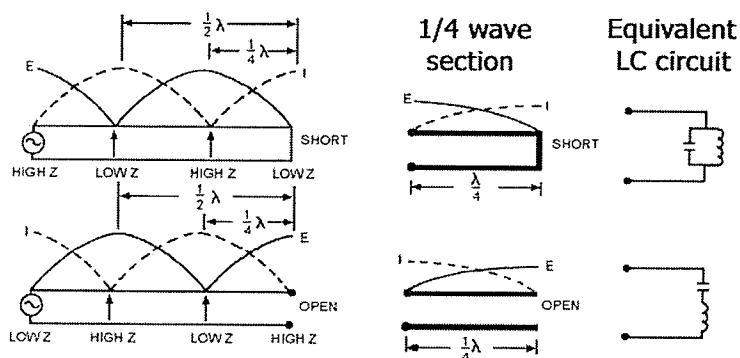


Figure 2.5 - Diagram of transmission line with E and I shown for shorted and open circuit ends and equivalent resonant circuit [68]

### 2.3 Resonant Cavities

Just as TEM transmission lines are used to guide an EM wave from one point to another in high frequency circuits [64], a general waveguide can be similarly used to transmit energy but with a few fundamental differences. For one, whereas TEM transmission lines consist of at least two parallel conductors, a waveguide can be comprised of a single conductor. Although transmission lines can only support the TEM mode of wave propagation, waveguides can support many propagation modes including TE, TM and TEM. Transmission lines can operate between DC and high frequencies, but become less efficient at high frequencies because of skin effects and dielectric losses. On the other hand, non-TEM waveguides can only operate above a certain frequency. Another advantage of waveguides is that they are capable of handling high power transmission with low loss, however, they are bulky and cumbersome to work with.

Despite all their differences, an important similarity between transmission lines and waveguides exists. Just as sections of transmission lines are able to function as resonant elements in a circuit, a terminated waveguide can also be found to resonate at particular frequencies. When used for such a purpose, the device is called a cavity resonator. Cavity resonators are structures which can confine an oscillating electromagnetic field in the form of standing waves, and are usually completely enclosed by conducting walls. A cavity's resonant frequency can be changed by altering the physical dimensions of the cavity, and can be designed with movable plates, screws, and other mechanical elements to be used for tuning and coarse adjustment.

## **2.4 Sensor Used in this System**

The sensor we have chosen to pursue is a simple coaxial cavity with length  $h$  selected to be a half wavelength long. The reason for choosing this design include a uniaxial sensitivity, and results which are simple to interpret. A schematic diagram of the sensor is shown in Figure 2.1. A small wire extending into the cavity excites an electromagnetic field within the cavity. The cavity can have many possible resonant modes. The simplest and most dominant mode is the  $TE_{001}$  [63] mode which occurs when the field is a maximum at the center of the cavity and zero at the edges. For the lossless case of a vacuum filled cavity, the resonant frequency for this mode is given by [63, 64]:

$$f_{res} = \frac{c}{2h} \tag{2.9}$$

where  $c$  is the speed of light in vacuum and  $h$  is the length of the cavity. When the material in which the sensor is encased is strained it will force a change in dimensions of the cavity. Strain is a unitless quantity defined as the ratio of an object's change in length over its nominal length and can be expressed as:

$$strain = \frac{\Delta h}{h} \quad (2.10)$$

As shown in equation 2.1, the resonant frequency of the cavity is only dependant on the speed of light and the cavity dimensions. Since the speed of light is a well known fundamental constant, any change in resonant frequency that can be used to unambiguously determine the change in the cavity length of the sensor, and hence the strain can be directly inferred from the resonant frequency of the cavity. To find the relationship between the resonant frequency in the strained and unstrained case, manipulation of the equation (1) governing the resonant frequency in the presence of a small strain  $\varepsilon$  of the cavity gives:

$$f_{strained} = \frac{c}{2(h + \Delta h)} = \frac{c}{2l\left(1 + \frac{\Delta h}{h}\right)} = \frac{c}{2h(1 + \varepsilon)} = \frac{c}{2h} \left(\frac{1}{1 + \varepsilon}\right)$$

$$f_{strained} = f_{unstrained} \left(\frac{1}{1 + \varepsilon}\right) \quad (2.11)$$

This can be approximated by the following equation when strain is small:

$$f_{strained} = f_{unstrained} (1 - \varepsilon) \quad (2.12)$$

which can be rearranged to give:

$$\varepsilon = \frac{f_{\text{strained}} - f_{\text{unstrained}}}{f_{\text{unstrained}}} = \frac{\Delta f}{f_{\text{res}}} \quad (2.13)$$

and

$$\Delta f = \varepsilon f_{\text{res}} \quad (2.14)$$

Clearly as long as the unstrained resonant frequency is known then the strain in the sensor can be determined with high accuracy and very little ambiguity. If the elastic properties of the sensor material differ from the material in which it is embedded, a gauge factor may be required to determine strain in the structure. Under compressive strain, it would be expected that as the cavity length decreases, the resulting resonant frequency increases (Figure 2.6).

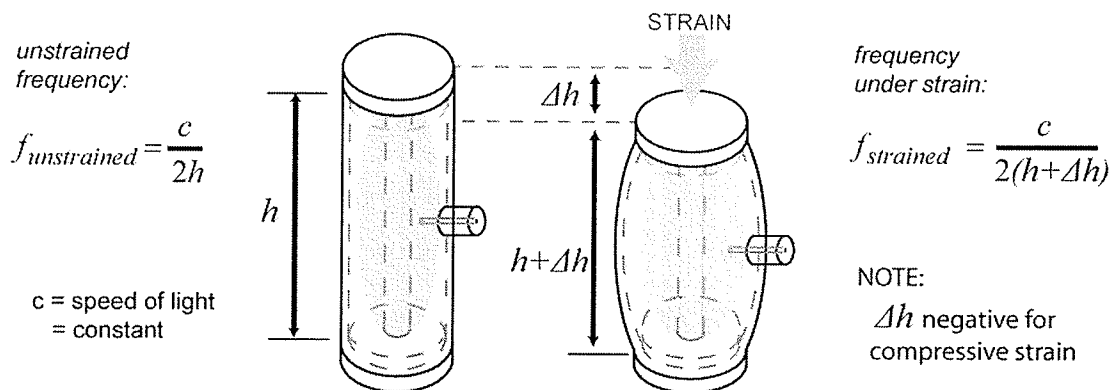


Figure 2.6 – Diagram of resonant cavity sensor under strain and resulting effects on resonant frequency.

The sensor can be fabricated from numerous conductive materials. The sensor described in this thesis is machined from brass. Two similar designs are presented. The first is constructed with the ends press fit on. In the second, an identical design is used however, the ends are additionally secured with a heliarc weld to reduce the effects of hysteresis

and unpredictable dimension change. A mechanical drawing of the sensor's construction shows dimensions of the sensor (Figure 2.7).

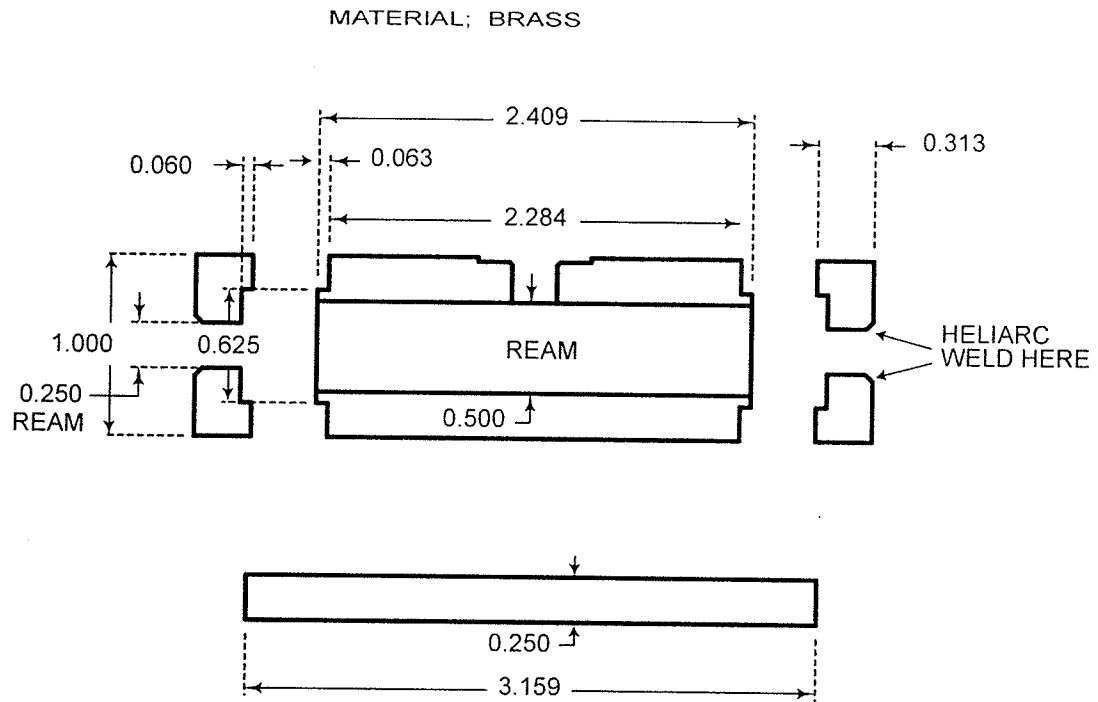


Figure 2.7 – Shop drawing of coaxial cavity resonator construction

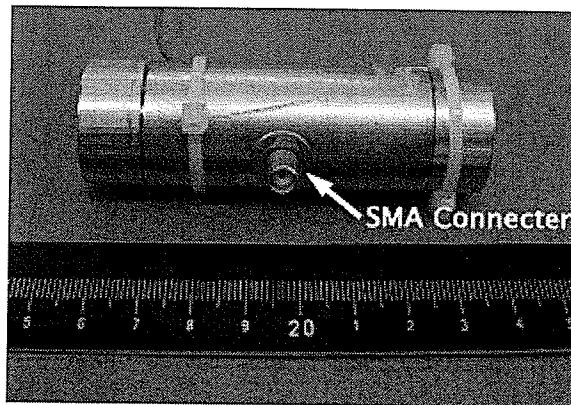


Figure 2.8 - Photograph of a resonant cavity sensor.

The hollow cavity in the center is approximately 61 mm long resulting in a resonant frequency of approximately 2.45 GHz and therefore an expected shift in resonant frequency of  $\Delta f \cong 2.45 \text{ kHz}/\mu\epsilon$ . The signal is coupled in and out of the sensor cavity through the connector such as the one shown in the photograph (Figure 2.8).

One advantage of this approach to measure strain is that RF signals, unlike optical sources for fiber optic sensors, can be generated with very high accuracy and stability relatively easily and inexpensively. RF signal generating sources can be easily frequency locked to quartz crystal oscillators which are easily obtained with error less than 1 part per million and stability within a few parts per billion [60].

#### **2.4.1 Capacitive Coupling Effect on Sensor Cavity**

S-Parameters are a measure of voltage reflection in an RF network. In a one port network,  $S_{11}$  is a measure of the ratio of reflected voltage wave to incident voltage wave at a single port. By observing  $S_{11}$  of the resonant cavity under constant strain via the HP 8753E Network Analyzer, it was found that by varying positions of the SMA connector, changes in the sensor's apparent resonance, could be observed. Changes in frequency location of the minimum reflection coefficient, minimum value of the reflection coefficient, as well as changes in bandwidth of the curve could be observed with varying connector depth.

As the connector was pushed into the cavity the resonant frequency was observed to decrease significantly. As well, it was observed that the  $S_{11}$  would exhibit different Q

factors for varying coupling capacitance, first increasing as the connector entered further into the cavity, and then decreasing again with continued increases in pin depth. A plot of  $S_{11}$  traces for varying pin depths is shown in Figure 2.9.

Although it is difficult to quantify the actual proximity of the pin from the center conductor, we can approximate the changes in distance by the known number of quarter turns of the connector into the cavity. Starting from the far right, each successive curve represents a quarter turn of the threaded SMA connector into the resonant cavity. The thread pitch of the connector is known to be 36 grooves/inch. Therefore, the total distance moved through each trace can be approximated to be  $\frac{1}{4}(.7055 \text{ mm/turn}) \sim .176 \text{ mm}$ .

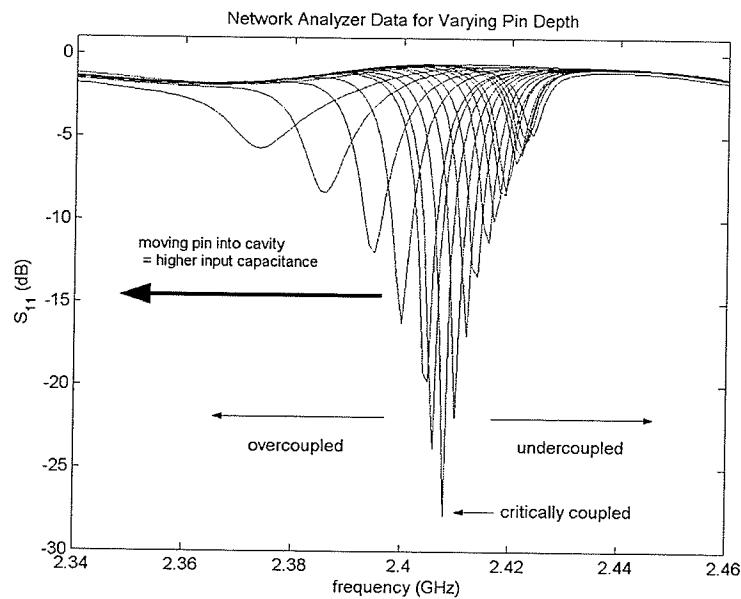


Figure 2.9 – Plot of  $S_{11}$  for varying connector depth into resonant cavity under constant strain.

## 2.4.2 Transmission Line Model of Sensor Cavity

To understand the effect of shifting resonant frequency with coupling capacitance, the sensor cavity can be modeled as a coaxial transmission line that is shorted at both ends. As the SMA connector that couples in the energy into the cavity does not actually touch the center conductor, the equivalent circuit of the transmission line is capacitively coupled at the input. The equivalent transmission line is shown in Figure 2.10.

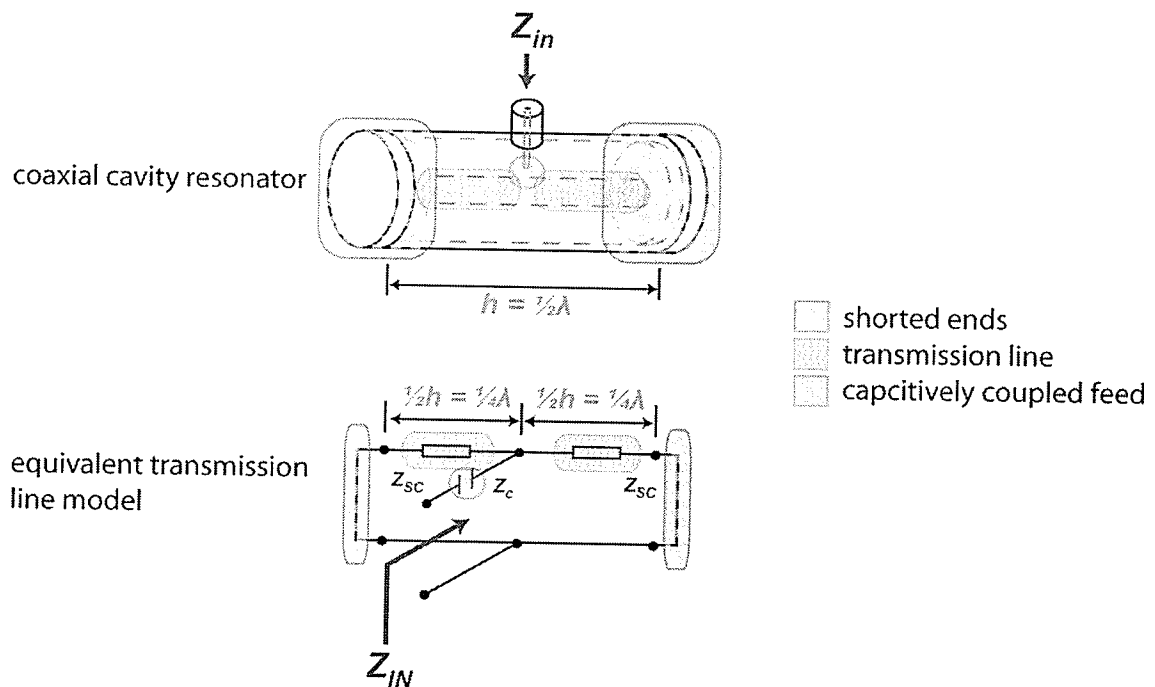


Figure 2.10 – Equivalent circuit model of coaxial cavity resonator.

The coaxial cavity resonator can therefore be represented by a center fed, gap coupled transmission line that is shorted at both ends. This combination can be represented by the series sum of an input capacitance and two parallel sections transmission line of length  $h/2$  where  $h$  is the inner length of the cavity resonator. Since capacitance is inversely

proportional to the separation between two conductors, as the pin protrudes into the resonant cavity, the capacitance of the connection increases. This changes the input impedance by changing the overall reactance of the equivalent circuit as viewed from the input end.

To model the equivalent circuit, the input impedance of each of the parallel transmission line sections must first be determined. These impedances are then combined in parallel, and then summed with the effect of the series capacitance which will be varied over several values.

Using Matlab to generate the mathematical model to match the measured data, a frequency space,  $f$ , was first defined to be a vector of linearly spaced values between 2.34 and 2.46 GHz. This vector was then multiplied by a factor of  $2\pi$  to yield the angular frequency  $\omega$ . Knowing the physical dimensions and the material properties of the resonant cavity, the distributed transmission line parameters  $R$ ,  $L$ ,  $G$  and  $C$ , were determined using the equations in Table 2.1. It can be seen that  $R$  is a function of frequency and can be expressed as  $R(\omega)$ . From Equations 2.1 and 2.2 it is clear that as a result of varying  $R$ ,  $\gamma$  and  $Z_0$  will also be functions of frequency. Therefore, each of the quantities  $R$ ,  $\gamma$  and  $Z_0$  were stored as vectors with each point in the vector corresponding to a value of  $\omega$ .

The input impedance to any section of a transmission line of length  $\ell$  is given by then given by the equation [64]:

$$Z_{in} = Z_0 \left[ \frac{Z_L + Z_0 \tanh(\gamma\ell)}{Z_0 + Z_L \tanh(\gamma\ell)} \right] \quad (2.15)$$

where  $Z_L$  is the impedance of the load terminating the transmission line, and  $Z_0$  is the characteristic impedance of the line. In this case,  $\ell = h/2$ . Therefore, for this particular resonant cavity, we can rewrite the expression as:

$$Z_{in} = Z_0 \left[ \frac{Z_L + Z_0 \tanh(\gamma h/2)}{Z_0 + Z_L \tanh(\gamma h/2)} \right] \quad (2.16)$$

where  $Z_L$  is the impedance of the load, and  $h/2$  is the length of transmission line from the input to where the load is connected, or equivalently, the distance from the input connector to one end of the cavity. Since the load impedance for a short circuit section of transmission line is  $0 \Omega$ , the expression for the input impedance of one of the parallel sections can be reduced to:

$$Z_{SC} = Z_0 \tanh(\gamma h/2) \quad (2.17)$$

where  $Z_{SC}$  denotes the input impedance into a section of line that is shorted at the load end. Since there are two sections of transmission line in parallel, we can combine them into one effective input impedance  $Z_{eff}$ . From basic circuit theory [65], we know that two parallel sections of impedance  $Z_A$  and  $Z_B$  can be combined into a single effective impedance  $Z_{eff}$  by the relationship:

$$Z_{eff} = \frac{Z_A Z_B}{Z_A + Z_B} \quad (2.18)$$

Therefore, for two identical sections of transmission line:

$$Z_{eff} = \frac{1}{2} Z_0 \tanh(\gamma h / 2) \quad (2.19)$$

Since the values of  $Z_{eff}$  are dependant on  $\gamma$  and  $Z_0$ , and therefore  $R$  and  $\omega$ , a corresponding vector for  $Z_{eff}$  was computed and stored.

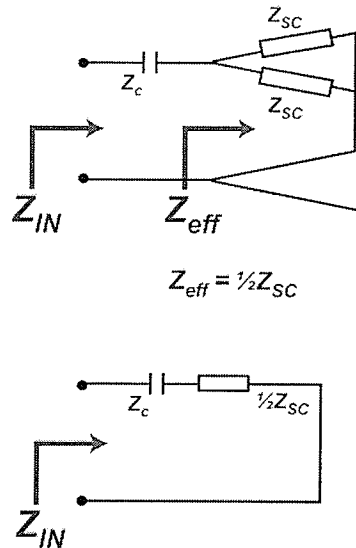


**Figure 2.11 – Diagram of total input impedance  $Z_{IN}$  from the connector of the resonant cavity when coaxial cavity sensor is modeled as a coupling capacitor ( $Z_C$ ) and two shorted transmission lines ( $Z_{SC}$ ).**

The total input impedance  $Z_{IN}$  into the cavity is then the series sum of the two impedances  $Z_C$  and  $Z_{eff}$ . Knowing the effective impedance  $Z_C$  of a gap capacitance  $C_g$  is expressed as:

$$Z_C = \frac{1}{j\omega C_g} \quad (2.20)$$

The total input impedance  $Z_{IN}$  into the cavity can then be written as:

$$Z_{IN} = Z_C + Z_{eff} = \frac{1}{j\omega C} + \frac{Z_0}{2} \tanh\left(\frac{\gamma h}{2}\right) \quad (2.21)$$

Where  $Z_{eff}$  is the effective input impedance of two parallel shorted sections of transmission line of length  $\ell = h/2 = \lambda/4$ .

The parameter  $\Gamma$  is the Voltage Reflection Coefficient and is defined by the reflected voltage over incident voltage. It is described by the mismatch of the input impedance of a load and the transmission line that preceded it. In this case, we are concerned with the energy that is coupled into the cavity, therefore, we consider the load to be the total input impedance looking into the resonator and the transmission line to be a 50 ohm transmission line feeding the cavity. For every value of capacitance, a vector for  $\Gamma$  can be found by application of Equation 2.8 in which each value in the vector corresponds to a single value of  $\omega$ . Since  $\Gamma$  is simply a ratio of two voltages, it can be converted to a dB value. The resulting vector of  $\Gamma$  is plotted vs.  $\omega$ , to yield a single curve. The calculations are then repeated for several values of coupling capacitance  $C_g$ .

Plotting the results of varying input capacitance on the reflection coefficient of the resonant cavity we get the curves shown in Figure 2.12.

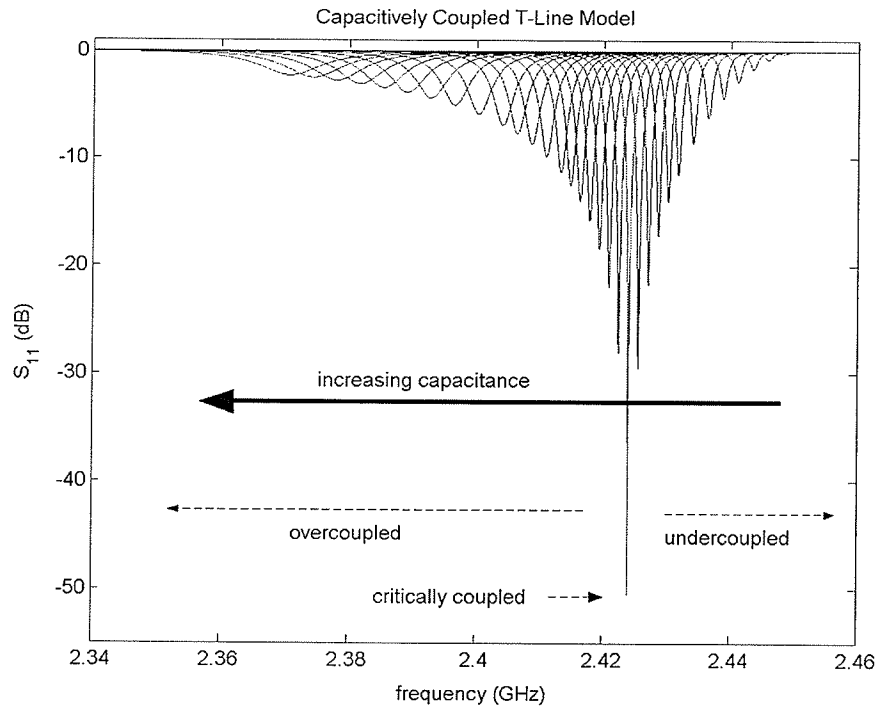


Figure 2.12 – Plot of transmission line model of resonant cavity with varying input capacitance.

The right side of the plot shows the undercoupled condition of the resonator. As coupling capacitance decreases, we expect to see resonance only as a result of the cavity, and hence, the behaviour of the resonator unloaded by external effects and input capacitance. When there is insufficient coupling into the resonator, the input impedance increases and the input to the resonator appears as an open circuit. When this occurs, the majority of the input signal is reflected back to the source. As coupling increases, the resonator will appear better matched to the input line and more power will be transferred to the resonant cavity. When the resonator is maximally matched to the feed at the resonant frequency, maximum power will be transferred from the feed to the resonator. At this point, the resonator is said to be critically coupled, and minimum power will be reflected back

towards the source. As the pin protrudes further into the cavity, an increased input capacitance will result in an impedance loading effect on the resonator as shown on the left side of the plot. In this condition, the resonator is said to be overcoupled, and as a result, the resonant frequency of the resonator drops as does the  $Q$ .

In this model, the curve at the far right of the plot corresponds to a coupling capacitance of 4 fF. The incremental change in coupling capacitance between successive curves was between 2 and 5 fF, with smaller increments closer to the critical coupling point which was found at 35 fF. The last curve at the far left of the plot corresponds to a capacitance of 106 fF. For further information, the values of coupling capacitance corresponding to each curve can be found in Appendix A.

From visual inspection, the generic t-line model appears to corroborate the measured results (Figure 2.13). To perform a quantitative analysis of the model with respect to the measured data, two curves were selected from the measured data set for comparison to the modeled results. The first curve was selected to be at the point of critical coupling and hence the highest  $Q$ . The other selected curve was selected to an overcoupled case. To compare the two curves visually on the same plot, the results of the model were translated in frequency to align the peak of the critically coupled curve. Doing so, we can see that the  $Q$  of the peaks in the model are much narrower than those actually measured. The 3 dB bandwidths, and resulting  $Q$  factors of these two curves were determined for both the

modeled results and the measured results and the values compared - confirming the visual assessment.

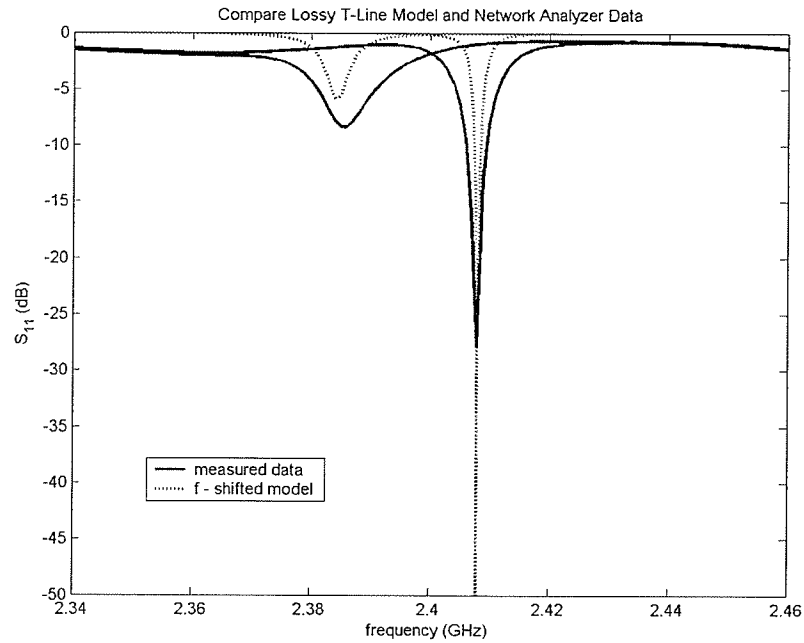


Figure 2.13 – Plot of measured data vs. modeled results showing significantly lower Q in measured results.

Q was measured and compared for the two curves for bandwidth assessed at points 3 dB from the peak/trough of the curve (3 dB BW low) and also for bandwidth at 3 dB from the lip of the curve (3dB BW high) as shown in Figure 2.14. The standard definition of bandwidth is generally accepted to be the frequency range between the two points 3 dB down/up from the peak. However, the 3 dB bandwidth from the lip of the curve was included for comparative purposes.

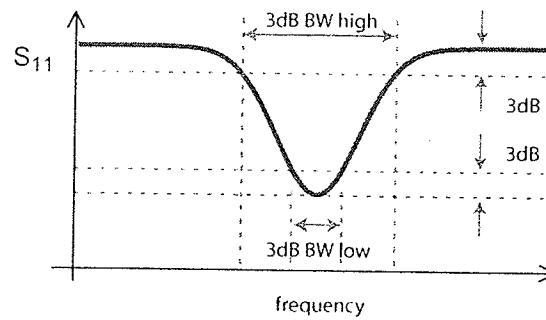
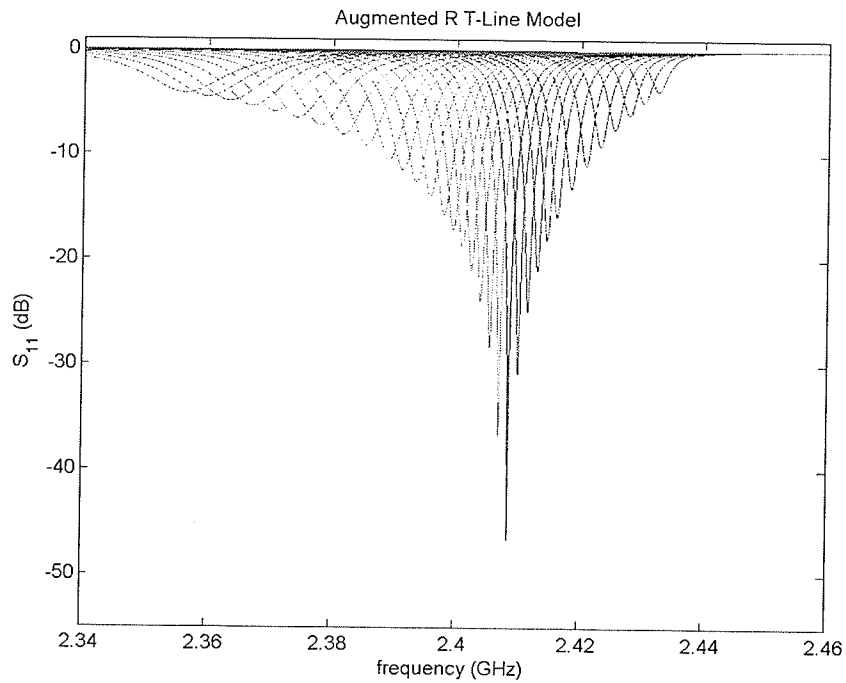


Figure 2.14 – Figure showing 3 dB bandwidth used for calculations of  $Q$  for comparing measured and modeled results.

In every case, the measured results show  $Q$  values that are considerably lower than those calculated. However, it is noted that although the general t-line model used does account for skin depth and parasitic effects of capacitance and inductance, it does not account for factors such as surface roughness and end losses. To partially reconcile the difference in the modeled vs. measured data, a first attempt was made by accounting for additional losses by augmenting the unit length resistance by a factor of 2.5. Repeating the calculations for the augmented R transmission line model (Figure 2.15), we find the model matches the measured data much more closely (Figure 2.16). In the augmented R model, the curve at the far right of the plot corresponds to a coupling capacitance of 24 fF. As before, the incremental change in coupling capacitance between successive curves was between 2 and 5 fF, with smaller increments closer to the critical coupling point which was found at 55 fF. The last curve at the far left of the plot corresponds to a capacitance of 126 fF. For further information, the values of coupling capacitance corresponding to each curve can be found in Appendix A.



**Figure 2.15 – Plot of transmission line model with of resonant cavity with varying input capacitance and additional R losses.**

The effects of added resistance include lowering the reflected power, as well as a shift in the apparent resonant frequency. Using a scaling factor of 2.5x distributed resistance, a shift of 15.3 MHz was observed between the two locations of the critically coupled point, and a shift of 14.9 MHz between the peaks of the over coupled curve.

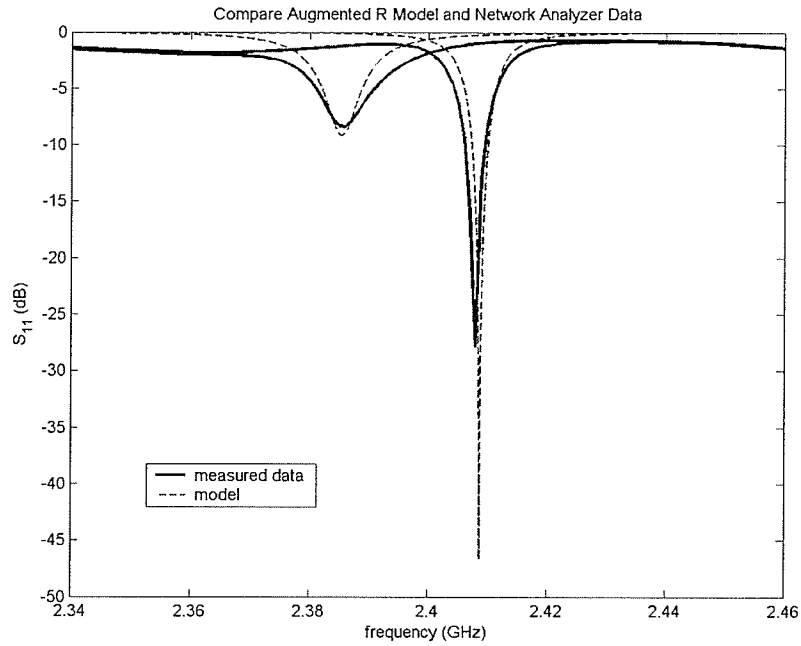


Figure 2.16 – Plot showing measured data vs. augmented model showing improved agreement.

Calculating values of  $Q$  for the augmented model, we find they much closer to those that were measured although the measured values are still much lower than those calculated.

The results of the modeled and measured bandwidths (BW) and  $Q$  factor are tabulated in Table 2.2.

Critically Coupled (CC)	A. 3dB from peak		B. 3dB from zero		
	fres (GHz)	BQ (kHz)	Q	BQ (MHz)	Q
1: lossy t-line model	2.4240	12.00	201983	3.16	767
2: modified model	2.4087	47.99	50191	7.77	309
3: measured	2.4080	995.02	2420	8.96	268

Over coupled (OC)	A. 3dB from peak		B. 3dB from zero		
	fres (GHz)	BQ (MHz)	Q	BQ (MHz)	Q
4: lossy t-line model	2.4003	4.85	495	4.66	515
5: modified model	2.3854	5.07	470	10.95	217
6: measured	2.3859	8.96	266	13.93	171

Table 2.2 – Table summarizing  $Q$  measured from 3 dB bandwidths for measured results, t-line model, and augmented loss t-line model.

The measured Q value is consistently and significantly lower than the modeled values as seen in each of the critically coupled cases. The overcoupled condition shows Q on the same order of magnitude, but still with considerable discrepancy. Given the disparate values of Q between the lossy t-line model, the modified model with additional resistive losses and the measured values, another model for determining the Q of the cavity was sought.

#### **2.4.2.1 Equivalent Lumped Circuit Model**

The Q factor of the cavity can be assessed by deriving the equivalent lumped element RLC circuit for the transmission line from the length of the transmission line, and the known distributed parameters R, L, G and C. Using the equivalent RLC circuit of lumped element components, a transient analysis of the circuit's natural response can then be performed, and a theoretical value of the Q calculated.

The values of the lumped element model can be found by manipulation of the expression (2.6) for input impedance  $Z_{in}$  [63]. As the length  $l$  of the transmission line is  $\lambda/4$  for some  $f = f_0$ , where  $f_0$  is the resonant frequency. Knowing  $\omega = 2\pi f$ , we can let  $\omega = \omega_0 + \Delta\omega$ . Assuming small loss, the expression for input impedance can be rewritten as:

$$Z_{in} = \frac{1}{\alpha l + j\pi(\Delta\omega)/(2\omega_0)} \quad (2.22)$$

Which is in the same form as the input impedance of a parallel RLC circuit is given by the expression:

$$Z_{in} = \frac{1}{(1/R) + 2j(\Delta\omega)C} \quad (2.23)$$

Therefore we can identify the equivalent lumped element circuit components to be:

$$R_{eq} = \frac{Z_0}{\alpha\ell} \quad (2.24)$$

$$C_{eq} = \frac{\pi}{4\omega_0 Z_0} \quad (2.25)$$

The equivalent inductance can then be found to be:

$$L_{eq} = \frac{1}{\omega_0^2 C} \quad (2.26)$$

And the Q factor of the resonator can be determined to be:

$$Q_{eq} = \omega_0 R_{eq} C_{eq} = \frac{\pi}{4\alpha\ell} = \frac{\beta}{2\alpha} \quad (2.27)$$

since at resonance:

$$\ell = \frac{\pi}{2\beta} \quad (2.28)$$

This lumped model was derived for both the nominal lossy t-line model as well as for the modified model with additional resistive losses included. The value of  $Q_{eq}$  for the equivalent parallel RLC circuits were found to be 1707 for the nominal lossy t-line, and 682 for the modified, augmented loss case.

Given values of R, L and C for an equivalent parallel resonant circuit, we can also perform a transient analysis of the resonant circuit's natural response by performing a nodal analysis on the lumped element circuit [65]. Using KCL, we obtain the following relationship between voltage, current, and the lumped element components in a parallel circuit.

$$C \frac{d^2 v(t)}{dt^2} + \frac{1}{R} \frac{dv(t)}{dt} + \frac{1}{L} v(t) = 0 \quad (2.29)$$

Which can be rewritten as the characteristic equation.

$$s^2 + \frac{1}{RC} s + \frac{1}{LC} = 0 \quad (2.30)$$

Solving the differential equation which governs the circuits voltage and current relationships, we obtain the roots to the characteristic equation which can be either real, or complex.

$$s_1 = -\rho \pm \sqrt{\rho^2 - \omega_0^2} \quad (2.31)$$

The values of  $\rho$  and  $\omega_0$  are determined by the R, L and C values of the parallel resonant circuit. In this case, these values are given by  $R_{eq}$ ,  $L_{eq}$  and  $C_{eq}$  respectively, and result in:

$$\rho = \frac{1}{2R_{eq} C_{eq}} \quad (2.32)$$

$$\omega_0^2 = \frac{1}{L_{eq} C_{eq}} \quad (2.33)$$

In this case, the solutions to the differential equation are complex and yield the general solution to the underdamped case yielding a natural response in the form:

$$V_o(t) = K_1 e^{s_1 t} + K_2 e^{s_2 t} \quad (2.34)$$

As  $s_1$  and  $s_2$  are complex, Euler's identity can be applied, and the resulting signal can be re-expressed as:

$$V_o(t) = e^{-\mu t} (A \cos(\omega_d t) + B \sin(\omega_d t)) \quad (2.35)$$

Where A and B are arbitrary constants as defined by the initial conditions.

Using Matlab, a simulation of the natural response was determined for both the nominal lossy t-line model and for the modified model with augmented losses. The results were then plotted as shown below in Figure 2.17. As expected, the amplitude decays much more rapidly with additional losses included in the model. For both the cases, the ring down time for varying levels of attenuation were calculated. The plot below shows values which are in line the Q factor calculated from the lumped RLC model as 95% attenuation of the signal requires approximately 1600 oscillations without additional losses, and only 620 oscillations with the added loss.

The time constant  $\tau$  represents the time required for an exponential signal to decay to  $1/e$ , or approximately 36.7% of its original value. For the augmented-R case, we can see that  $\tau$  is approximately 90 ns. We can then calculate Q by the relationship [61]:

$$Q = \omega_0 \tau \quad (2.36)$$

where  $\omega_0$  is the resonant frequency expressed in radians/second, and  $\tau$  is equal to the time constant for a decaying power signal. As power is proportional to voltage squared, we expect that time constant for a power signal to be  $\frac{1}{2}$  that of the voltage signal. Therefore, in terms of a power signal, we obtain a value for  $\tau$  of approximately 45 ns. From this, we calculate  $Q = 684$ .

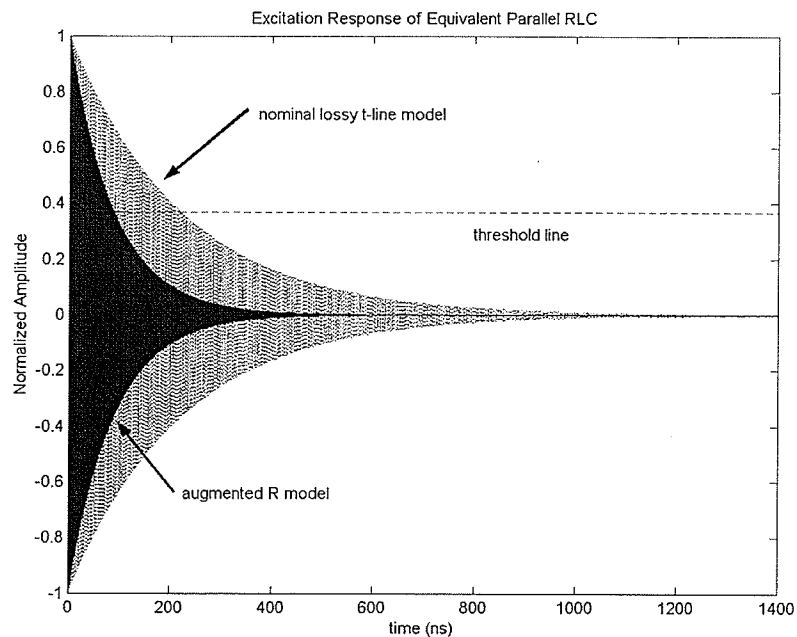


Figure 2.17 – Plot of simulated natural response for equivalent lumped RLC circuit for cavity resonator.

## 2.5 Compression Test

To validate the coaxial cavity resonator as a strain sensor, the sensor was placed in a load frame and tested under compressive strain. To do this, the sensor was first encased in a concrete cylinder. In this case, the concrete was used to provide an approximation to

actual usage conditions and not intended to be tested to critical failure. Therefore, the actual mix and strength of the concrete was not critical, and for these experiments, a simple 3:2:1 mix was hand mixed. This mix indicates the proportion of small aggregate, sand and cement respectively. The cylinder was then capped with to provide smooth flat end surfaces for even pressure distribution across the cylinder with an applied load. The concrete cylinder was then loaded into a compression frame so strain could be applied to the cylinder.

To prepare the sensor for encasement in concrete, the SMA connector was secured in place with the use of a locking nut and loctite. When the loctite has had sufficient time to cure, the seams and joints of the sensor are sealed with a layer of nitrile rubber (Figure 2.18a). The outside of the sensor is then wrapped in a thick layer of butyl rubber (Figure 2.18b) which is stretched over the sides of the sensor and over the connector, leaving only the ends of the sensors exposed to the concrete. The entire package was then centered inside a concrete cylinder (Figure 2.18c, Figure 2.18d). A traditional metal foil strain gauge is applied to the outside of the cylinder to provide a reference strain measurement.

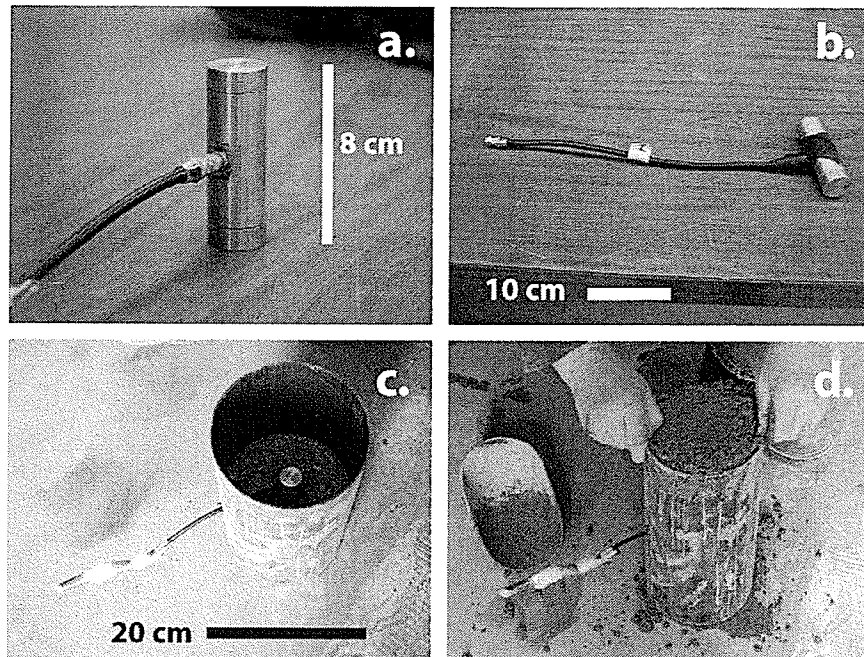


Figure 2.18 – Casting of sensor in concrete cylinder

### 2.5.1 Press Fit Sensor

An initial reading of the reflected voltage to incident voltage ratio ( $S_{11}$ ) of the sensor under no strain showed a resonant frequency at approximately 2.42 GHz as measured with an HP 8753E network analyzer. This curve can be seen in Figure 2.19.

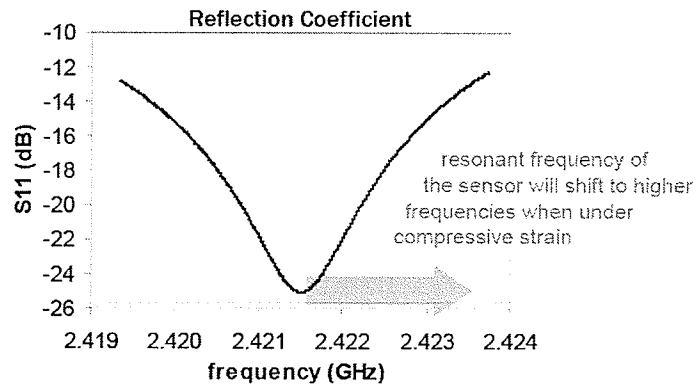


Figure 2.19 –  $S_{11}$  of resonant cavity as read from network analyzer showing predicted effects of compressive strain.

From the compression test, measurements of resonant frequency shift versus applied strain yielded the curve shown in Figure Figure 2.20. The measured response with the best fit line showed a conversion factor of 2.6 kHz per  $\mu\epsilon$ . The signal is coupled in and out of the sensor cavity through the connector shown in the with a high degree of linearity up to 130  $\mu\epsilon$ . The signal is coupled in and out of the sensor cavity through the connector shown in the. Strain levels beyond 130  $\mu\epsilon$ . The signal is coupled in and out of the sensor cavity through the connector shown in the showed an unexpected decrease in the resonant frequency shift  $\Delta f_{res}$ . This may be explained by the nature of construction of this particular cavity. As the ends are press fit on, there may be some frictional forces which are overcome beyond the 53379 N of force used to causing the cavity dimensions to change in an unpredictable manner.

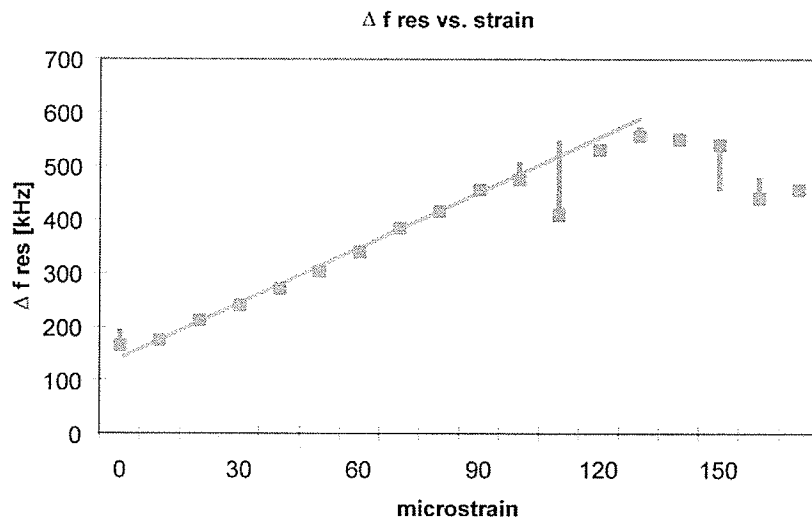


Figure 2.20 – Plot of frequency vs. strain for press fit sensor.

It was noted that the resonator did appear to exhibit hysteresis during the first few strain cycles as the zero point appeared to shift upwards in frequency until settling down at approximately 120 kHz from the initial point.

### **2.5.2 Welded Sensor**

To verify the hypothesis that the effects of hysteresis and non linearity were due to construction of the sensor with a press fit, an identical sensor was constructed but with the end pieces secured with a heliarc weld at the ends. This sensor was again treated with the same preparation and encased in a concrete cylinder like the first sensor. In this case, the load was cycled several times between 0 and 200  $\mu\epsilon$ , which corresponds to approximately 124000 N of force. A typical output plot of  $\Delta f$  vs. applied strain is shown in Figure 2.21. Testing of this sensor showed significantly less hysteresis, with the change in resonant frequency returning to zero when the load was released. As well, it did not exhibit the same effects as the unwelded resonator in demonstrating non-linear effects beyond 130 microstrain. A best fit line showed a conversion factor of 1.98 kHz/ $\mu\epsilon$  with a high degree of linearity up to 200  $\mu\epsilon$ . Although we expect to read 2.42 kHz/ $\mu\epsilon$ , applying a gauge factor may be sufficient to compensate for the difference in material elasticity between the sensor and the concrete structure.

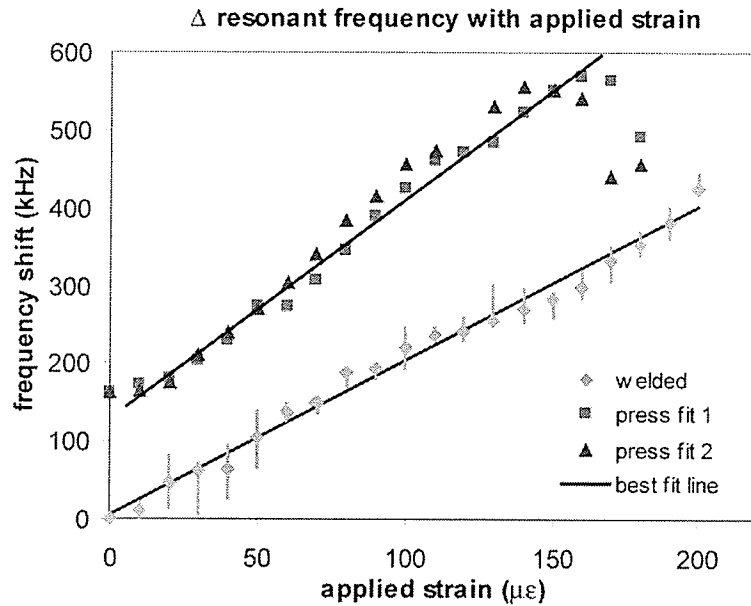


Figure 2.21 – Plot of frequency vs. strain for welded sensor compared to press fit sensor.

While the initial load cycles did not demonstrate any residual effects of compression when the load was released, they did show a resistance to meeting the expected  $\Delta f_{\text{res}}$  vs. strain relationship. The maximum strain measured on the first load cycle was 160  $\mu\epsilon$ . Although a  $\Delta f_{\text{res}}$  of approximately 500 kHz is expected, only a 210 kHz shift was recorded. With successive load cycles however, the maximum frequency shift appeared to converge towards expected values as shown in Figure 2.22. This may be explained by binding or frictional forces of the concrete when in contact with the sides of the sensor that may be relieved with a few cycles.

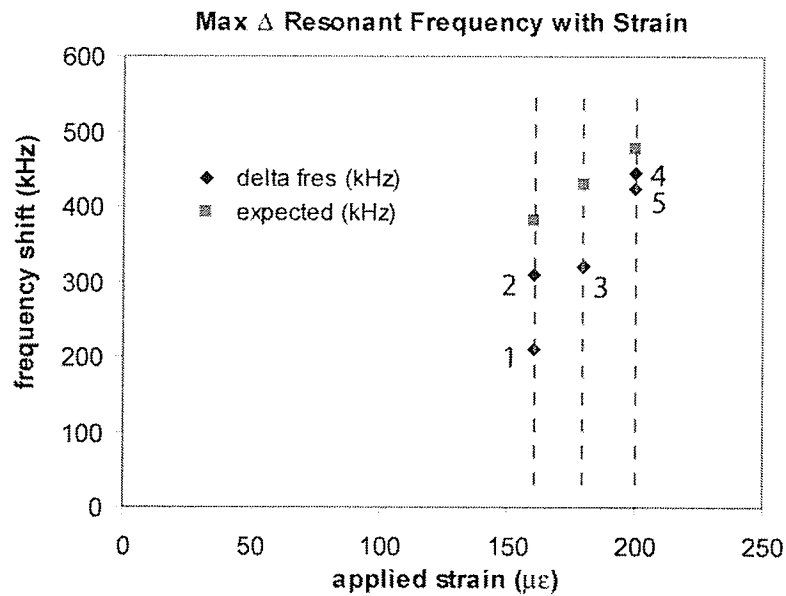


Figure 2.22 – Plot of max frequency shift with max strain for first 5 cycles.

## 2.6 Sensor Installation

Sensor installation is easier, faster, and far less labour intensive or troublesome than installation of fiber optic or metal foil strain gauges because the sensors are robust, and do not need to be bonded to the structure. As well, as there is no connection that has to run between the sensor and the data acquisition unit, cables do not have to be run through specially laid conduits. As demonstrated with the casting of the test sensor in a concrete cylinder, the sensor needs only to be positioned with the length of the sensor along the axis of interest. This can be accomplished during casting of the structure, or secured to the rebar or conduit in advance of casting.

The photograph (Figure 2.23) shows sensor placement in a full scale replica of a steel free bridge deck. This structure is a laboratory model of the North Perimeter bridge in

Winnipeg, Manitoba. In this model, the sensors were simply attached to the conduit and FRP (fiber reinforced polymer) bars with cable ties. At this time, testing has yet to be performed on the structure, and therefore no data from the sensors has yet been obtained.

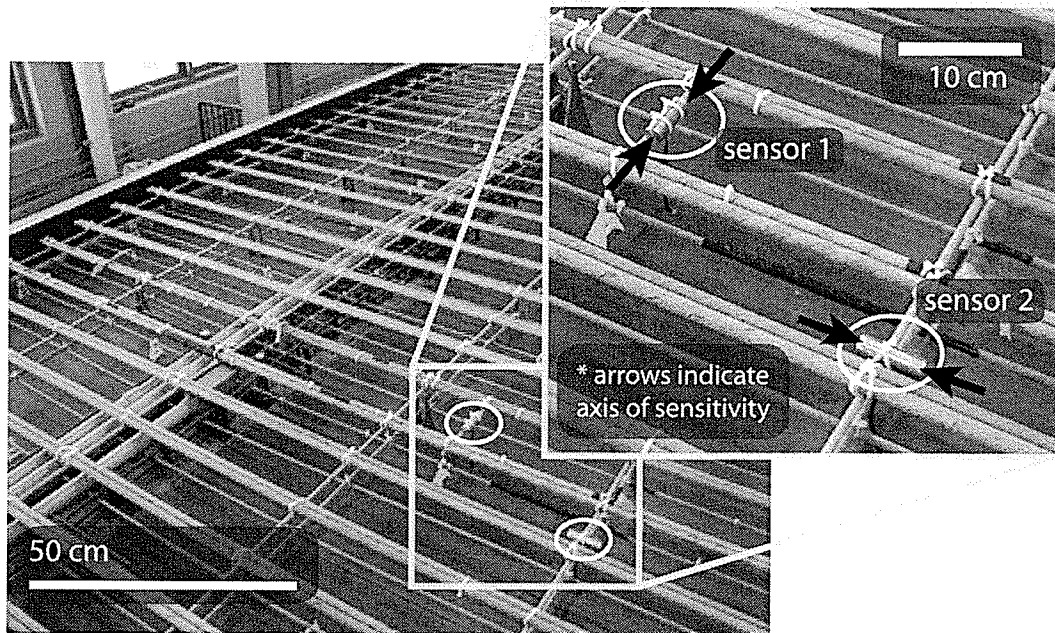


Figure 2.23- Photograph showing sensor installation in scale model bridge deck.

## 2.7 Chapter Summary

In this chapter, an overview of the theoretical basis of the sensor was described. This included a basic overview of resonant systems, transmission lines, and general resonant cavities. A discussion of the sensor used in this project was then presented. This included experimental data obtained for changing coupling capacitance of the feedline into the resonator. To quantify the effect of capacitive coupling on the sensor characteristics, a distributed parameter transmission line model of the sensor was developed in Matlab and the results compared to measured data. This model was then later augmented to account

for additional losses and to better reflect measured data. As well, from the distributed transmission line parameters, an equivalent lumped circuit model was obtained. From the lumped circuit model, a theoretical  $Q$  was calculated for both the general lossy transmission line as well as for the augmented R model. From the equivalent lumped elements a transient analysis of the resonant systems was also presented, yielding a time constant value that could again be used to measure  $Q$  of the resonant cavity. The results of two similar sensor designs under compressive strain tests demonstrated good linearity and low hysteresis could be obtained and therefore could make this device a viable strain sensor.

## Chapter 3 Interrogation System for Wireless Sensing

An interrogation system is used to wirelessly measure the resonant frequency of the embedded sensor and hence determine the amount of strain in the sensor. To do this, the interrogation system must act as both a transmitter and a receiver of an RF signal. The interrogator generates a signal that is square wave modulated, effectively allowing it to transmit an RF signal 50% of the time and receiving the signal returned from the sensor during the other 50% of the time. An antenna is attached to the sensor to pick up and transmit signals between the sensor and the interrogation system.

Functionally, the interrogation system is assuming the task performed by the network analyzer in the previous chapter – that is, determining the resonant frequency, or shift of the resonant frequency of the sensor under strain. However, it is important to distinguish between the results that they produce. The  $S_{11}$  from network analyzer is indicative of the voltage reflection from the sensor. A minimum in  $S_{11}$  implies the input line is best matched to the sensor at that frequency; meaning maximum power is transferred to the sensor, and a minimum reflected signal is detected. However,  $S_{11}$  does not account for where the energy goes. It does not distinguish between the energy transferred to a standing wave, energy which is absorbed in the conductor or otherwise dissipated as a result of impedance mismatch, cable loss, and cavity losses.

The interrogation system, on the other hand, transmits a signal to the cavity which generates a standing wave inside the sensor. When the RF signal is turned off, the energy stored inside the cavity will re-radiate out. The interrogation system then measures the power in the returned signal. Because the strength of the signal is directly proportional to the energy which was stored in the cavity, it is clearly a measure of the sensor's resonant frequency.

### **3.1 Basic Interrogation System**

A block diagram of the basic sensing system is shown below (Figure 3.1). The process starts with the transmission of a signal from a Rhodes & Schwarz RF source. This signal is passed from the function generator to the transmitting antenna (Demarc Technologies Group SPLG11F) via a 2 position switch (Minicircuits ZASWA-2-50DR RF switch). This energy is then transmitted into free space. In the diagram, the shaded regions over the signals indicates the time when the interrogation system is transmitting. Another antenna that is connected to the resonant cavity will pick up some of the transmitted signal and couple it into the sensor. Here, the energy builds an electric field which at some point in time reaches a state of equilibrium. In the case of this resonator with a  $f_{\text{res}}$  of approximately 2.42 GHz and Q determined to be greater than 600 (Chapter 2), equilibrium of the excited field will occur in approximately 100 ns. Sometime after equilibrium is reached, the interrogation unit switches from send to receive. The energy stored in resonator will re-radiate out from the resonator and out of the attached antenna in the form of a decaying RF signal. The received signal is directed through a low noise

amplifier (Minicircuits ZHL-1724MLN-SMA) and into an RF peak detector (Anritsu 73N50) such that the power in the signal can be measured. The switching rate between sending and receiving states is controlled by a TTL control signal generated by a Stanford Research Systems function generator. In this particular case, square wave between 1 and 4 MHz was used to control the switching state.

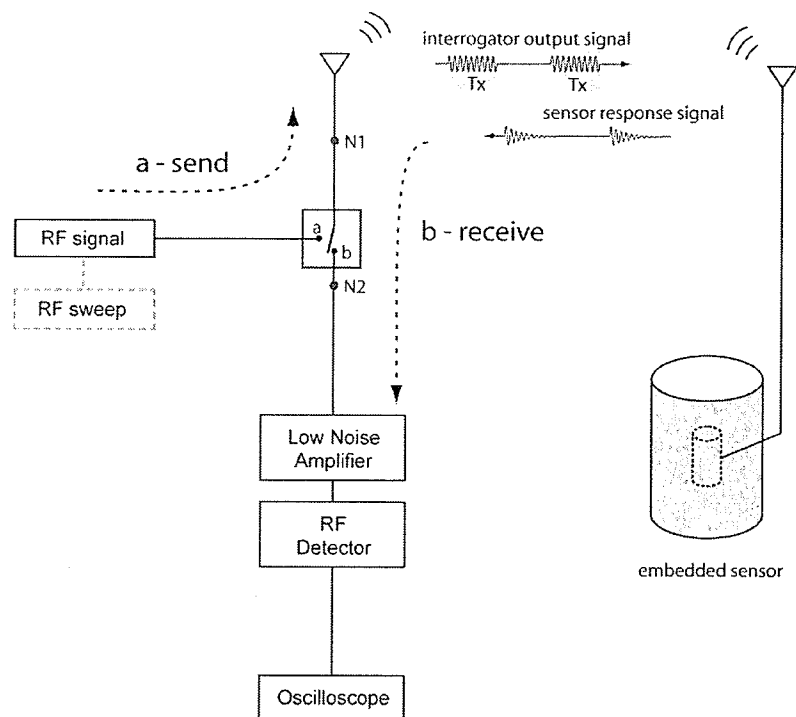


Figure 3.1 – Block diagram of the basic interrogation system discussed.

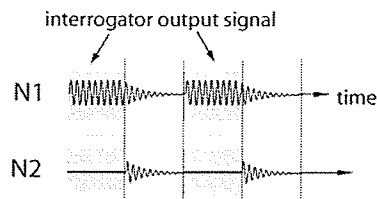


Figure 3.2 – Signal at nodes N1 and N2 as marked in the block diagram.

To find the resonant frequency, the input RF signal is swept across a range of frequencies. The returned signal is expected to have maximum amplitude and duration when the input signal is at the resonant frequency of the cavity. Using the Anritsu 73N50 detector in the small signal range, the output voltage of the detector is expected to be proportional to the detected power with a scaling factor of  $-0.35 \text{ mV}/\mu\text{W}$ . The negative relationship indicates the negative polarity of the detector.

A plot of the expected signal at the output of the RF detector is shown in Figure 3.3. It is expected that the signal would increase to a maximum when the switch first changes position into the “receive” state, as maximum power will be detected. This transition to the maximum value will be limited by the time constant of the detector. The signal is then expected to show some exponential decay as the energy in the cavity radiates out. It is expected that all time domain signals will show this basic form, but with varying magnitudes that are affected by the separation distance between the two antenna, and the input frequency relative to the resonant frequency of the cavity. When the input frequency is at the resonant frequency, maximum energy will be stored in the cavity in the form of a standing wave, and hence maximum signal should be returned. At input frequencies far from resonance, it is expected that this signal would go to zero.

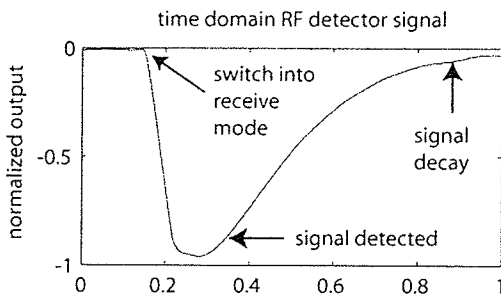


Figure 3.3 – Figure showing expected time domain signal from the RF detector.

As a rough measure of resonant frequency, the transmitted RF signal can be adjusted over a range of frequencies to find where the received power at the detector is a maximum. Performing this measurement under unstrained conditions did not yield expected results. First, the output waveforms showed considerable deviation from the expected shape. Secondly, although the waveforms were reproducible for a given frequency, this shape was not consistent through the entire frequency range. Thirdly, it did not appear that the signal attained a maximum amplitude or maximum signal duration as it passed through the sensor's resonant frequency. Typical output traces of the RF detector time domain signal are shown below in Figure 3.4 for varying input frequencies  $f_{in}$ . The encircled points are those which show unexpected or unusual results. The resonant frequency for this sensor was approximately 2.422 GHz. Because the distortions show different effects at different frequencies, it is likely that they are due to interference from superimposed signals.

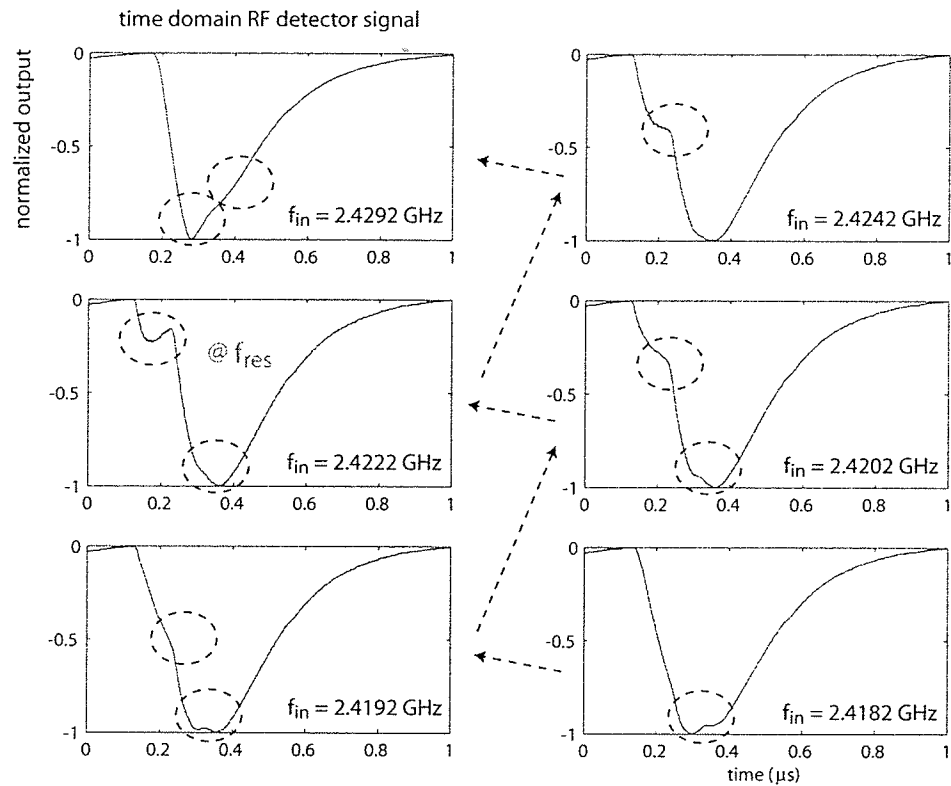


Figure 3.4 – Plots of (normalized) typical output signal of the RF detector.

Finding the total power in the signal requires integration under the curve. However, as the signal is simple in form, an approximation can be obtained by passing the output of the detector through a low pass filter to effectively measure the DC value of the output signal as shown in Figure 3.5. The low pass filter used was a simple RC circuit with a cut off frequency of 1 kHz. When sweeping across a range of frequencies, the resulting curve of DC values is expected to show roughly the same form as  $S_{11}$ . The expected output can be approximated by a Gaussian shaped curve that shows maximum signal is detected when the input frequency is at or near the resonant frequency of the sensor, and attenuated for input frequencies that are too high or too low.

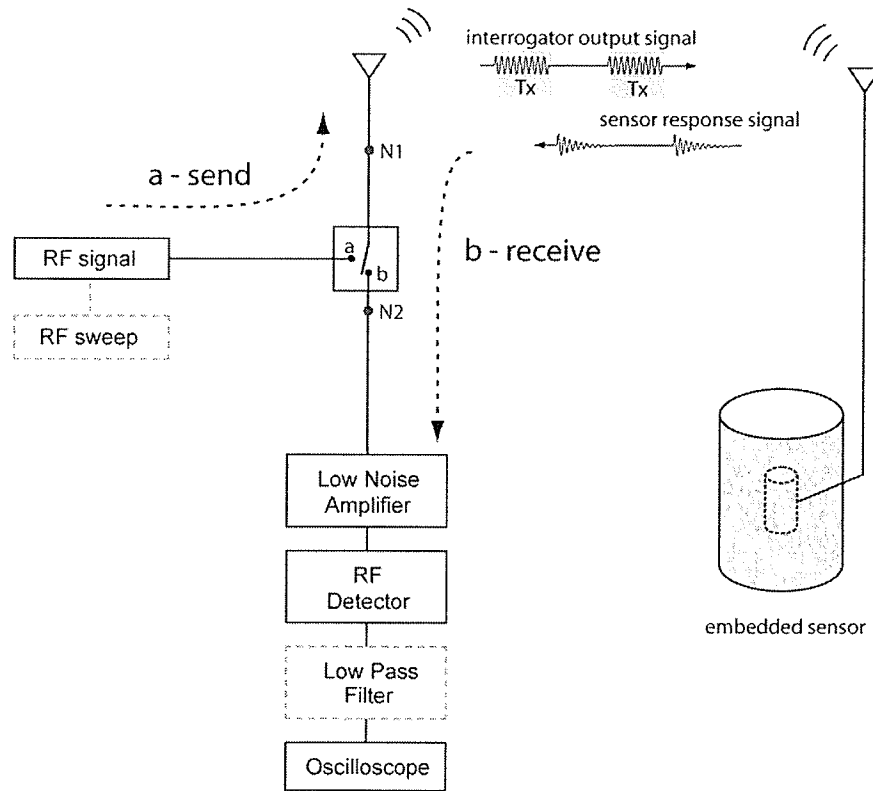


Figure 3.5 – Block diagram of basic interrogation system with low pass filter.

Sweep curves from the interrogation system did not show the expected frequency response. Rather than a smooth Gaussian shaped curve with near zero background levels, a small peak at the resonant frequency was almost indistinguishable over high background signal. A typical frequency sweep is shown in Figure 3.6.

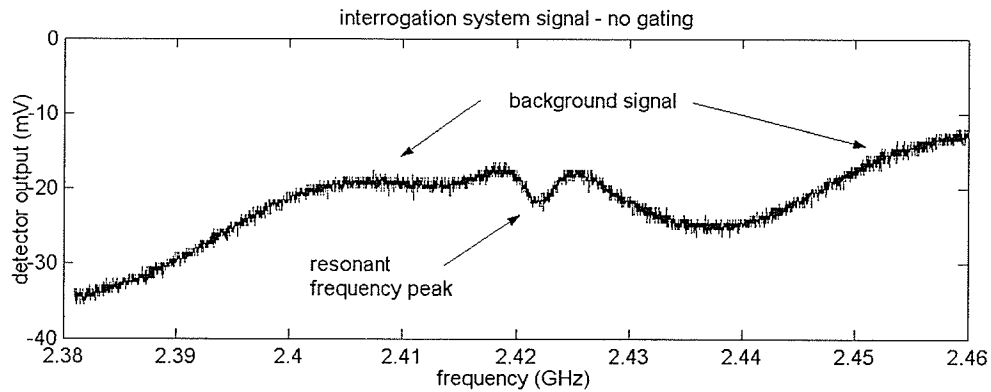


Figure 3.6 – Plot of typical output signal of low pass filter over a range of frequencies.

Because both the time domain and frequency domain signals show the effects of constructive and destructive interference, it was hypothesized that the distortions in the detected signal were due to environmental reflections and noise which were of differing frequency and phase from those returned from the resonant cavity. To investigate this hypothesis, time domain measurements were taken with the input frequency near resonance and again far off resonance where zero signal would be expected. As well, without changing any other conditions, the sensor was disconnected from the receiving antenna. The results showed that when the input frequency is far from the resonant frequency, and even when the sensor is entirely disconnected, a non-zero signal exists at the output of the RF detector.

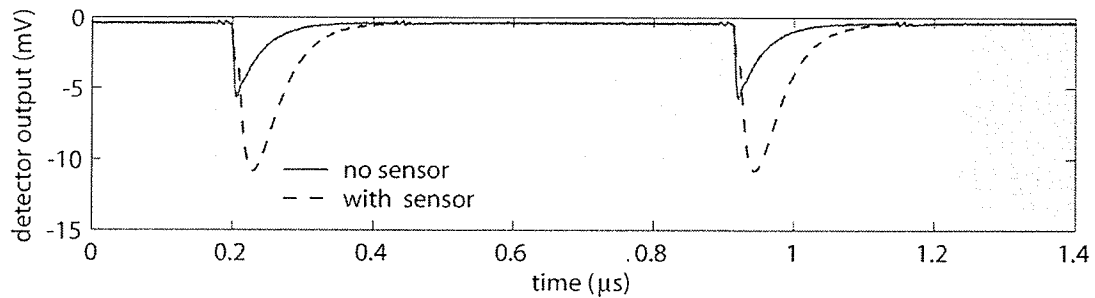


Figure 3.7 – Plot showing time domain signal from RF detector with and without sensor connected.

This non-zero response strengthened the belief that the sharp corners in the time domain signal and the background levels in the frequency sweeps were due to out of phase additive signals from sources other than the RF signal that was returned from the cavity. As demonstrated with SAW devices [41], the effects of environmental reflections can be reduced with the use of time domain gating. In the next section we will describe how time domain gating was used to reduce the effects of these effects and produced results which closely match idealized expectations.

### 3.2 Gated Interrogation system

A time domain gated detection circuit was implemented by the addition of a second RF switch as shown in Figure 3.8. Again, a Minicircuits ZASWA-2-50DR RF switch was selected such that the transition times of the switch could be assumed to be identical. Then by controlling the TTL signals for the switches, a variable time lag can be inserted between the “receive” state of the primary switch, and the passing of the received signal to the detector. This effectively discards the first few nanoseconds of the detected signal where the environmental reflections occur. Because the cavity is highly resonant, it will

continue to emit a signal from the stored energy well after the energy from environmental effects have been sufficiently attenuated. A diagram of the signals at nodes N1, N2 and N3 as marked the block diagram can be seen in Figure 3.9. A photograph of the interrogation system and experimental setup can be seen in Figure 3.10.

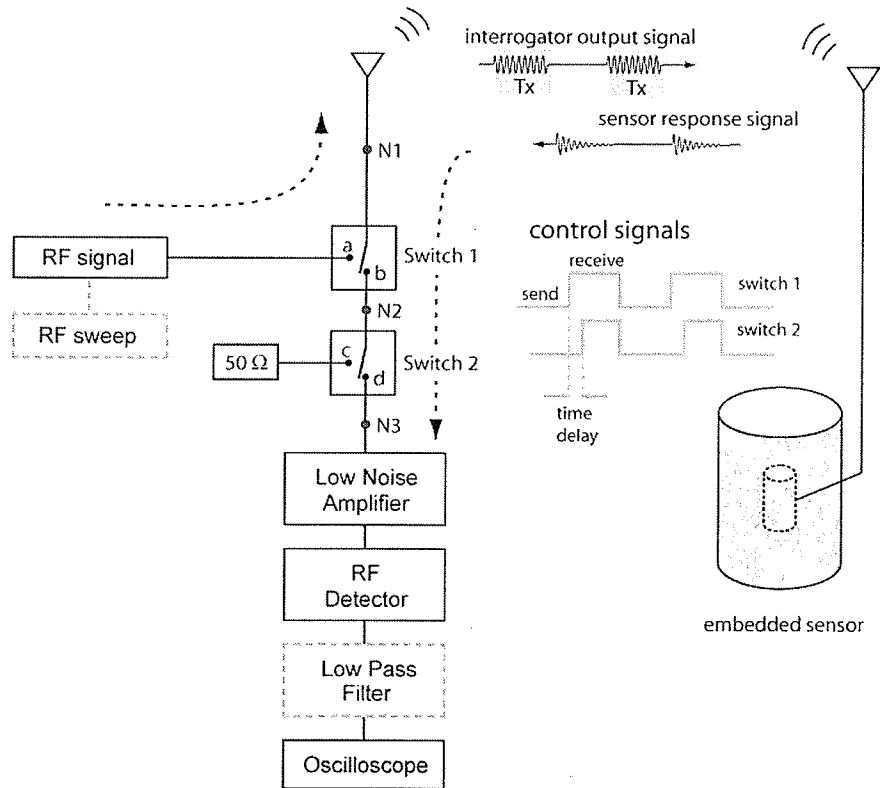


Figure 3.8 – Block diagram of circuit and control signals for time domain gating.

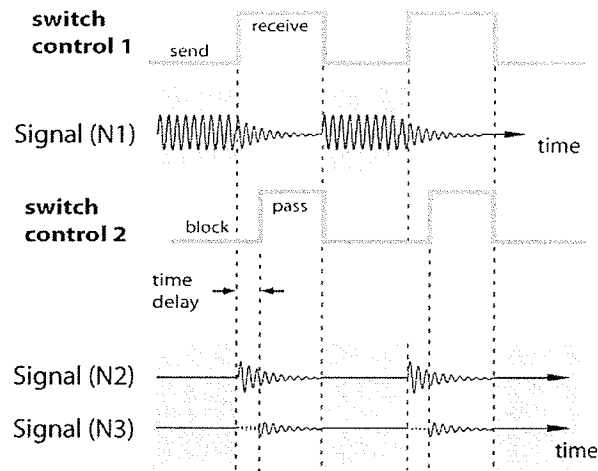


Figure 3.9 – Time domain signals at nodes N1 and N2 and N3 as marked in the block diagram showing effects of time domain gating.

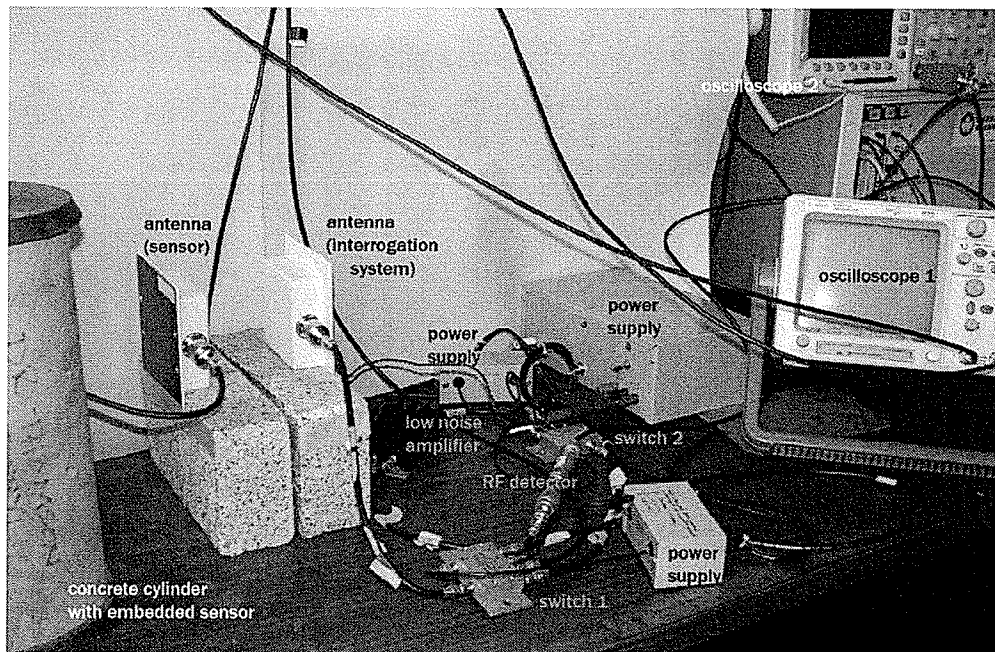
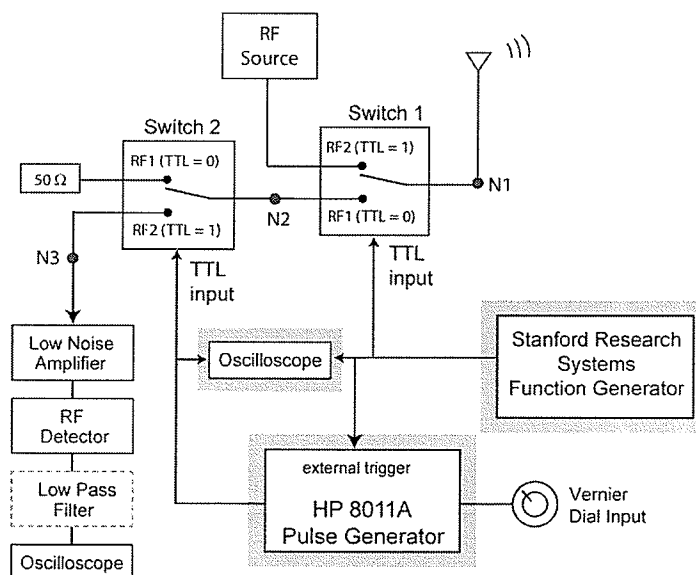


Figure 3.10 – Photograph of interrogation system and experimental setup.

To be able to control the timing of the two switches, two methods of generating the second TTL signal were investigated. Initially the TTL signal for Switch 2 was implemented with the addition of a HP 8011A pulse generator which could generate a

variable duty cycle square wave with period determined by an external trigger (Figure 3.11). A 'T' from the Stanford Research Systems function generator allowed the TTL control signal from Switch 1 to also serve as the input trigger for the pulse generator. The output of the pulse generator was then used to control the state of Switch 2. The time delay between the two signals was viewed and measured using an oscilloscope while the actual delay time (pulse width) was controlled with a vernier dial on the pulse generator.

Difficulties in using the pulse generator included only being able to trigger on the positive edge of the input signal. Therefore, both switches could not pass on the high signal. To implement a variable time delay between the two switches, Switch 1 was set to receive on the TTL = high signal, and Switch 2 was set to pass signals to the detector on a TTL = low signal as illustrated below (Figure 3.12).



**Figure 3.11 – Block diagram showing use of HP 8011A pulse generator for timing control of two switches.**

However, because of this arrangement, the time delay between the signals is actually determined by the time between the transition to the “send” state of Switch 1, and the “pass” state of Switch 2, rather than between the transition to the “receive” state of Switch 1 and the “pass” state of Switch 2. For a 1 MHz TTL signal, the time between “send” and “receive” is 500 ns. Because we are concerned with a time delay of only a few ns between the “receive” state of Switch 1 and the “pass” state of Switch 2, the actual time delay of interest is only a few parts per hundred of the set value. Therefore, we can see that the timing for Switch 2 is difficult to control as a small amount of jitter in the timing signal could have a significant effect on the transition time of the second switch. As well, the vernier dial was very sensitive, and difficult to set accurately because of mechanical effects in the actual dial.

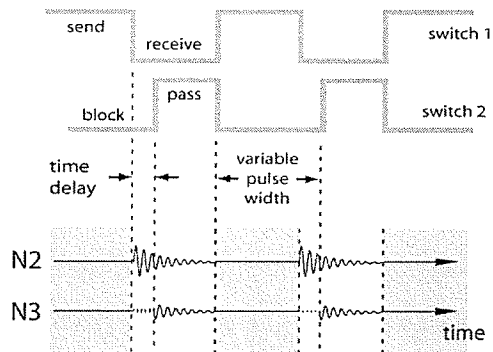


**Figure 3.12 – Diagram showing TTL control signals for the two switches and the resulting signals at N2 and N3 as marked on the block diagram using a HP 8011A pulse generator.**

As an alternative solution, a HP 8016 word generator was used to generate the TTL signals. This instrument allowed for a time delay between the two signals to be controlled with a vernier dial. Because this instrument is designed for timing control between

signals and does not depend on varying pulse width to create the time delay, it is much more stable and less prone to drift.

One of the problems with using this instrument as the switching signal was the pulse width could not be controlled using this method. Given the TTL signals generated by the word generator (Figure 3.13), it can be seen from the block diagram (Figure 3.8) that the when Switch 1 first moves back to position a, (sending RF signal to antenna), Switch 2 is still in position d (passing signal to the detector) for some time before switching to position c. Although theoretically there is no incoming signal from Switch 1, initially it was thought that signals would be passed from the RF source to the detector if there was insufficient isolation between the switch's input ports. However, experimental results do not indicate that this is a problem.

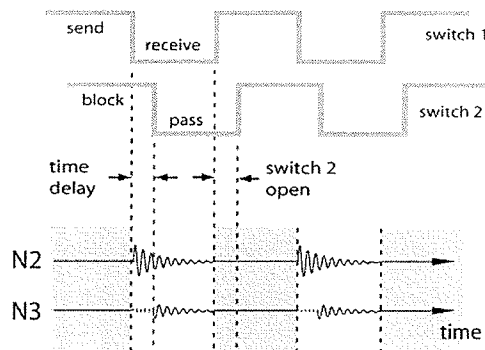


**Figure 3.13 – Diagram showing TTL control signals for the two switches and the resulting signals at N2 and N3 as marked on the block diagram using a HP 8016A word generator.**

With the additional switch in place, the time delay was manually adjusted until the environmental reflections were eliminated. This occurred at approximately 8 ns. At this point, the detector output signal is near zero levels when the resonator is removed, and

also when the input frequency is far from the resonant frequency of the cavity (Figure 3.14). As the switching time of the Minicircuits ZASWA-2-50DR switch is specified to be 7 ns (typical, 10 ns maximum) between 50% of the control signal and 90% RF (turn on), and 3 ns (typical, 10 ns maximum) between 50% of the control signal and 100% RF (turn off) the signal distortion may actually be a result of pass through of the RF source signal. As well, another factor to consider is the resonance of the antenna. The Demarc SPLG11F patch antenna has a specified bandwidth of 80 MHz, with a center frequency of 2.4 GHz. This corresponds to a Q of 300. Since this is a highly resonant element, the antenna may continue to resonate for some time after the interrogator has switched from “send” to “receive”.

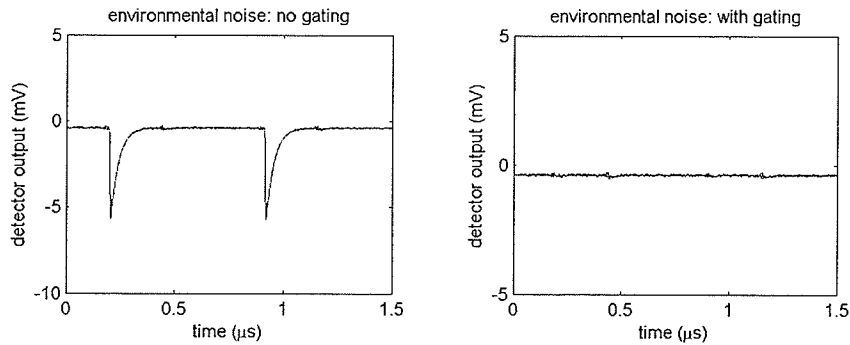


Figure 3.14 – Plot showing environmental noise at output of RF detector with and without gating.

Improvements in the signal with the use of gating can be clearly seen in both the time domain and frequency domain output signals. In the time domain, the signal is considerably smoother (Figure 3.15). However, the improvement in signal form is accompanied by decreasing signal amplitude as gating time increases. Although the

signal amplitude decreases considerably, we see later that the signal to noise ratio (SNR) is actually improved.

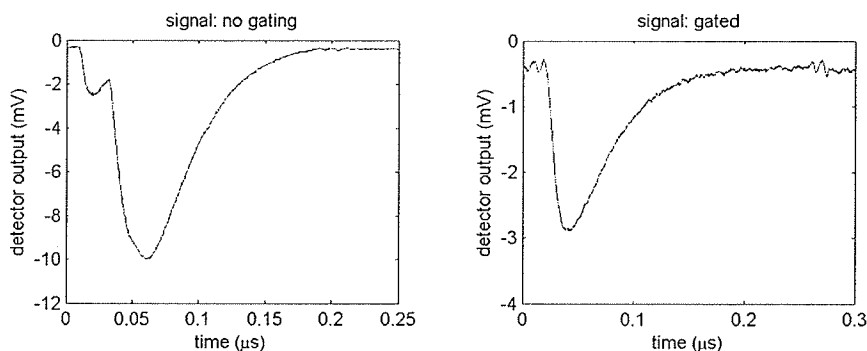


Figure 3.15 – Plot showing time domain signal from RF detector output with and without gating.

With no gating, the decay constant of the noise signal (Figure 3.14 left) was determined to be approximately 37 ns. The decay constant of the detected signal for the single switch (Figure 3.15 left) and double switch (Figure 3.15 right) cases were determined to be 55 ns and 56 ns respectively.

In the frequency domain, the returned spectrum shows a much more Gaussian form with near zero background levels as expected (Figure 3.16). A reading of the sensor's  $S_{11}$  was also obtained from the HP 8753E Network Analyzer and superimposed over the gated signal. We can see that although there is good agreement with respect to resonant frequency, there appears to be significant difference in measuring the apparent Q of the sensor.

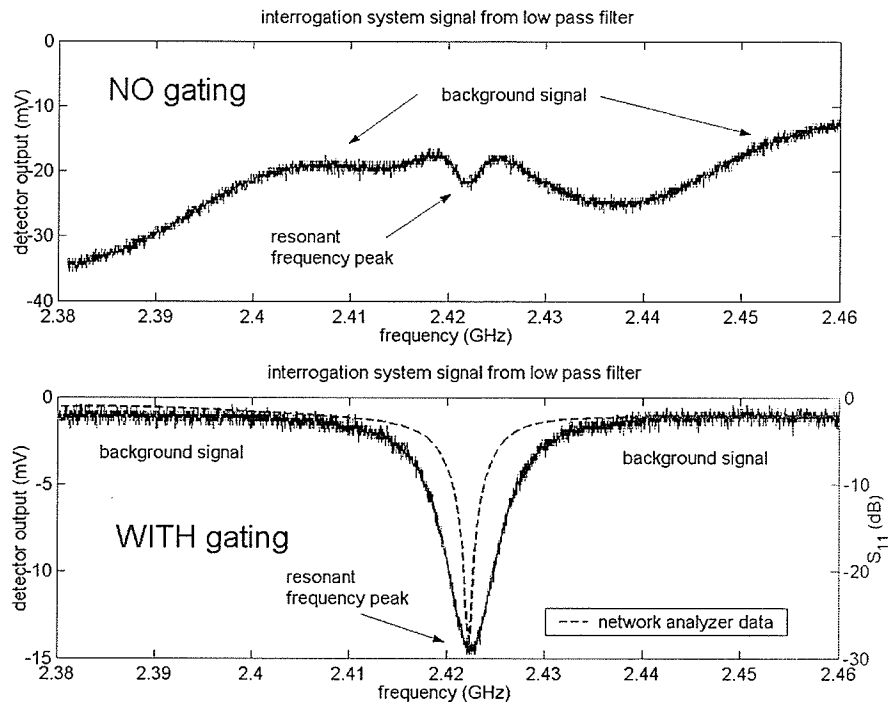


Figure 3.16 – Plot showing frequency sweep of sensor without gating, and with gating showing results much closer to ideal.

### 3.2.1 Effects of Increasing Time Delay Between Switches

Noticeable reductions in background levels with increasing time delay can be seen up to the point the environmental noise is entirely gated out. However, increasing the time delay further after this point does not result in improved signal quality, but results only in a decrease in signal amplitude. Effects of increased time delay on output signal amplitude are shown in the composite plot below (Figure 3.17). Each subplot is a sweep of the input frequency from 2.40 to 2.44 GHz with the output plotted in mV. In these plots the data has been multiplied by -1 and shown as positive values.

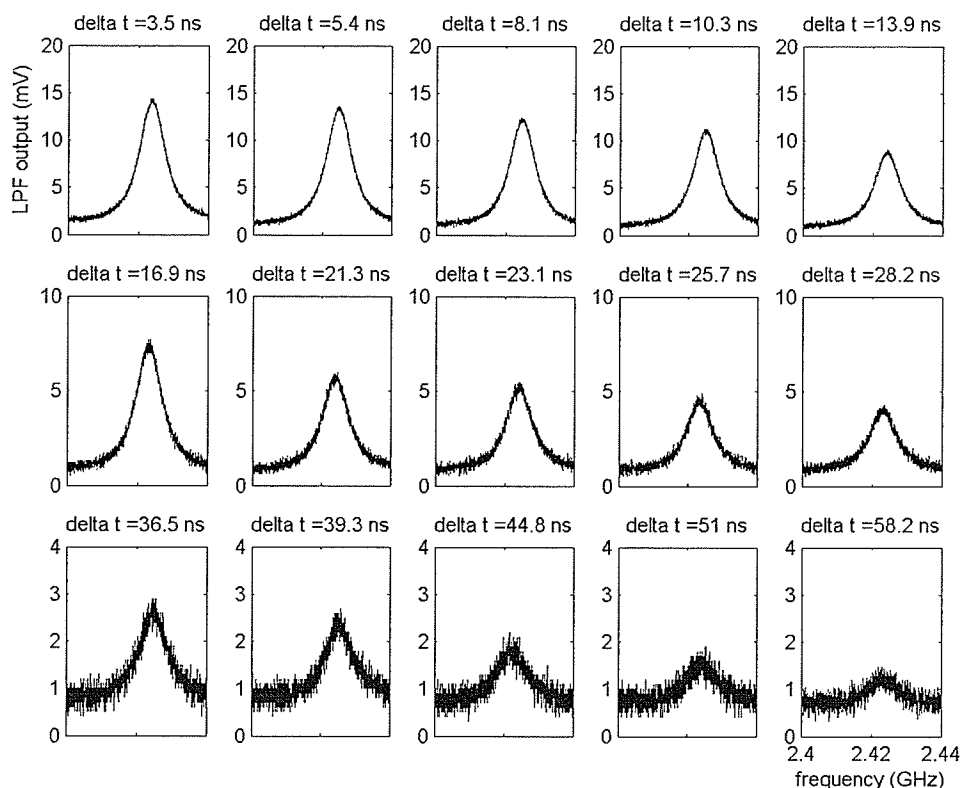


Figure 3.17 – Composite plots of frequency sweeps with increasing time delay.

The amplitude of the signals were then plotted versus their respective lag in switching signals (Figure 3.18). Using the Matlab curve fitting toolbox, this data was then fit with the expected exponential relationship.

$$f(x) = ae^{-bx} + c \quad (3.1)$$

where  $a$ ,  $b$ , and  $c$  are constants. Goodness of fit was evaluated using an R-square value. R-square is essentially a measure of how well the fitted curve accounts for variability in the observed data. It is the square of the correlation between the response values and the predicted response values. It is also called the square of the multiple correlation

coefficient and the coefficient of multiple determination. It is determined by the ratio of the sum of squared differences between the predicted data and the mean, over the sum of squared differences between the sampled data and the mean.

In this case, the R-square value was calculated to be .9933, meaning the model accounts for over 99.33% of the variability in the data set. A R-square value of 1 would indicate a perfect fit.

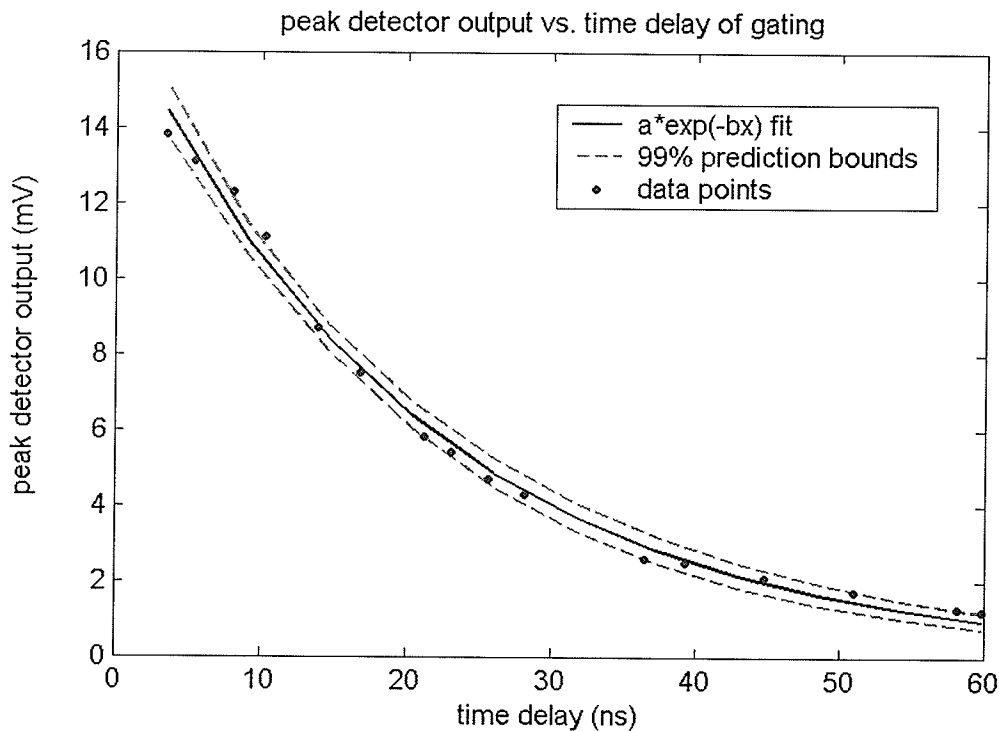


**Figure 3.18 – Plot of maximum amplitude vs. gating delay showing inverse exponential relationship.**

As shown before in chapter 2, time constant can be used to determine Q factor. The time constant  $\tau$  is a measure of the time required for the signal power to fall to  $1/e$

(approximately 37%) of the maximum value. With an initial value of  $\sim 14.5$  mV,  $\tau$  corresponds to the time required for the signal to fall to approximately 5.3 mV. We can see that this occurs at approximately 22 ns. In this case, we again invoke the relationship [61]:

$$Q = \omega_0 \tau = 2\pi f_0 \tau \quad (3.2)$$

where  $\omega_0$  and  $f_0$  are the center frequency, in radians and Hz respectively, and  $\tau$  is the time constant. Therefore with a  $\tau$  of 22 ns, and a center frequency of approximately 2.42 GHz, we calculate the Q of the system to be approximately 334. This is approximately off by a factor of 2 from the Q calculated in Chapter 2 from the lumped element model. However, it is important to note that although it did include an augmented factor of resistive loss, the lumped element model did not consider the effects of capacitive coupling, which can not be isolated in the measured case. However, it is also noted that this  $\tau$  is also significantly less than that measured from the time domain signals in Section 3.2. This can not be explained at the present time and will be the subject of future investigation.

### **3.2.2 Signal Level vs. Antenna Separation Distance**

As before, the sensor cavity was disconnected from the antenna and the time delay between the two switches was manually adjusted until time domain signal from the RF detector was reduced to zero. With the minimum time delay necessary to remove the environmental reflections, the system was maintained under constant operating parameters while the two antennas were moved to varying separation distances. The results of the interrogation system output for varying antenna separation can be seen in

the composite plot (Figure 3.19). Each subplot shows the output of the low pass filter over a 40 MHz frequency sweep between 2.40 and 2.44 GHz. In these plots the data has been multiplied by -1 and shown as positive values plotted in mV.

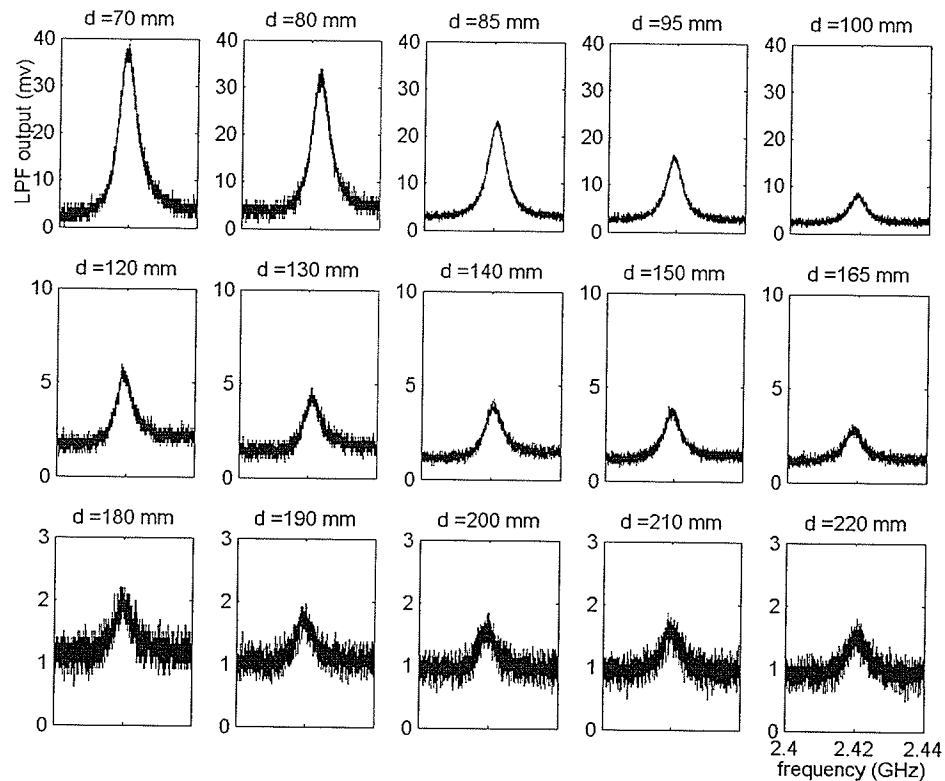


**Figure 3.19 – Composite plot showing effect of increasing separation distance between two antennae. All y-axis in mV, all x-axis span 2.4 GHz to 2.44 GHz sweep.**

The amplitude of each trace was then plotted vs. separation distance. The resulting curve of peak detector output vs. separation distance was fit with a curve describing the expected decrease in signal with distance (Figure 3.20). In this case, it was a  $x^{-4}$  fit as described by:

$$f(x) = \frac{a}{x^4} + c \quad (3.3)$$

where  $a$  and  $c$  are constants. In general power density is expected to be inversely proportional to  $x^{-2}$ . However, in this case, because the power is not simply reflected by the sensor but received, stored, and re-transmitted, the signal is actually decreased by a factor of  $x^{-2}$  in both directions. The goodness of fit for the  $x^{-4}$  curve was evaluated to have an R-square value of .9595, indicating that over 95% of the data variability is accounted for in the model. It is noted that although the data shows a reasonable fit over the entire data set, strictly speaking, the  $x^{-4}$  relationship is only valid in the far field region of the antenna. This region is defined where the angular field distribution is independent of distance from the source [69]. For most applications, this region can be assumed to exist at distances greater than integer multiples of the transmitted wavelength.

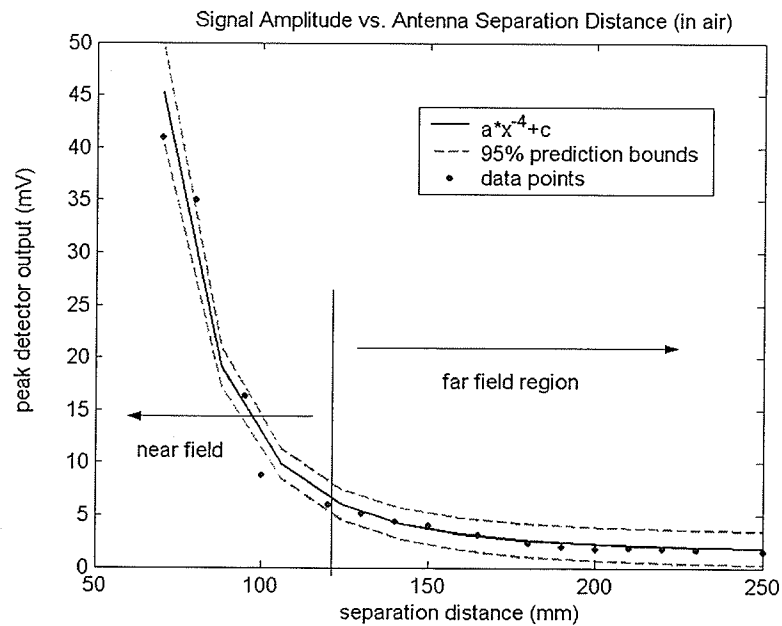
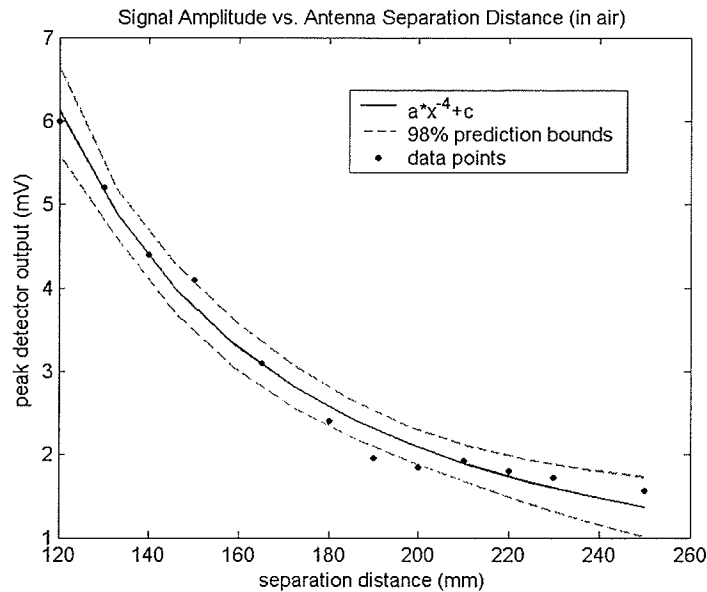


Figure 3.20 – Plot of maximum amplitude vs. antenna separation distance (in air) showing inverse  $x^4$  relationship.

Considering only data points at distances greater than  $\lambda$  ( $\sim 12$  cm), we again apply the  $x^{-4}$  fit as described by Equation 3.3. In this case, the goodness of fit was evaluated to have an R-square value of .9843, indicating that over 98% of the data variability is accounted for in the model.



**Figure 3.21 – Plot of maximum amplitude vs. antenna separation distance (in air) showing inverse  $x^4$  relationship for far field region only.**

The  $r^{-4}$  relationship between separation distance and received power has obvious consequences. The significant implications include the system's design requirements for power output and antenna gain, as SNR will drop off rapidly with separation distance between the interrogator and sensor. At the distances required for practical use, which are expected to be in the 40 to 60 cm range, this might necessitate the enhancement of SNR through different antenna designs which can improve gain and lower attenuation factors.

As well, the interrogation system may be modified to make use of curve fitting techniques to accurately determine the peak frequency under conditions of low SNR.

### 3.2.3 Measuring Q with Effects of Coupling Capacitance

As before in chapter 2, the effect of capacitive coupling of the input to the resonator can be explored by setting the input feed at varying distances from the center conductor and measuring the detected power over a range of frequencies. However, in this case, the sensor is queried using the wireless interrogation system for varying pin depths. From the resulting curves (Figure 3.22), Q factor can be obtained from the relationship [61]:

$$Q = \frac{\omega_0}{BW} = \frac{2\pi f_0}{BW} \quad (3.4)$$

Where  $\omega_0$  and  $f_0$  represent the center frequency of the peak in radians and Hz respectively, and BW generally refers to the 3 dB bandwidth of the curve (Figure 3.23). The 3 dB bandwidth is used for signals of voltage or current, and corresponds to the point where the signal has fallen to  $1/\sqrt{2}$  (approximately .707) of its maximum value. Because power is proportional to  $V^2$  or  $I^2$ , on a power plot the 3 dB bandwidth would correspond to when the signal has fallen to  $1/2$  of the maximum signal since  $(1/\sqrt{2})^2 = 1/2$ . As the voltage at the RF detector output is a representation of the power received, in this case the full width half max bandwidth is used [61]. From this value, the Q can then be calculated. Since the measurement is the power in the signal that is returned from the sensor, rather than simply an absence of a reflected energy, we are more convinced that the measure for the obtained curves is a measure of the cavity's resonance than in the case of  $S_{11}$ . In  $S_{11}$ ,

the absence of a reflection indicates the resonant system is closely matched to the feedline, and maximum power transfer occurs. However, it is not necessarily a good measure of the amount of energy that is stored in the resonant device as shown by the disparity between the apparent Q and the signal decay time discussed in Chapter 2. In this case, the quantity measured is not the ratio of reflected power to incident power, but rather a measure of energy accumulation of the cavity. When the interrogation system is switched from “send” to “receive”, the detected signal is indicative of the actual energy which has been stored in the cavity in the form of a standing wave.

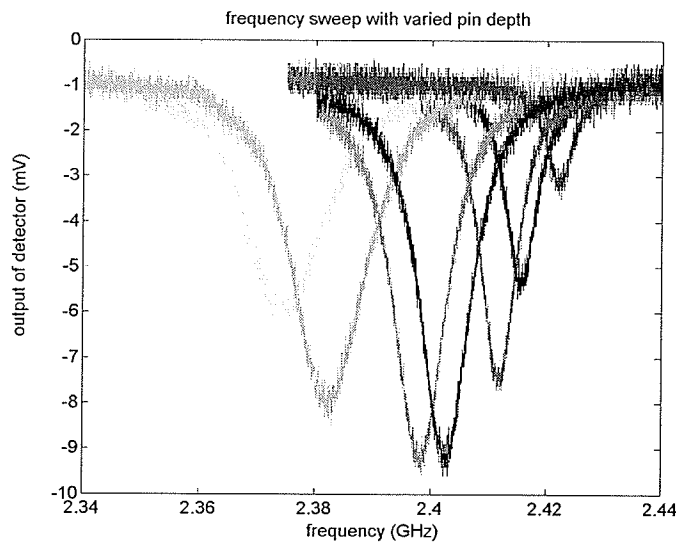


**Figure 3.22 – Plot of detector output through low pass filter with varied pin depth. Frequency decreases with increasing pin depth (increased coupling capacitance).**

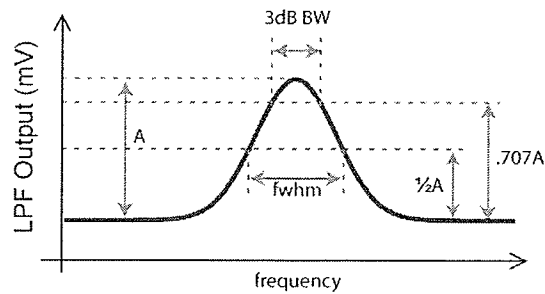
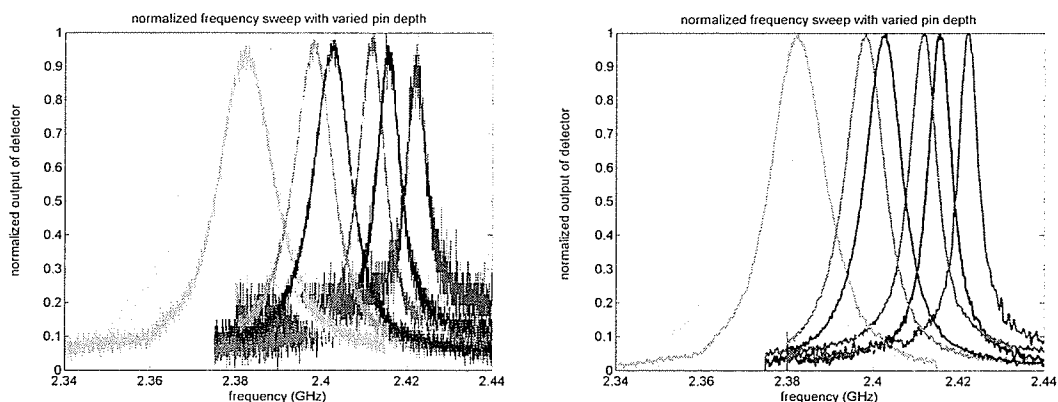


Figure 3.23 – Plot showing 3 dB and full width half max thresholds and bandwidths.

The data shows bandwidth of the curves increases linearly with the coupling capacitance (Figure 3.25), and that  $Q$  increases with decreasing coupling capacitance. At high and low coupling capacitances, the slope for the both the bandwidth and  $Q$  curves decreases as expected. When the coupling capacitance is small, it plays a smaller role in loading the resonator and hence does not significantly change the reactance of the equivalent circuit. When it is large, its effects will dominate over those of the resonator.

Bandwidth and  $Q$  was calculated for the data and then repeated after the data was smoothed with a 16 point moving average filter (Figure 3.24). As additive noise can make the peak appear much broader than it actually is, the purpose of the filter was to reduce these effects and to obtain an accurate measure of the bandwidth. This is more important for curves of smaller amplitude, where the signal to noise ratio is considerably lower. Clear examples of effects of noise on apparent bandwidth can be seen in the composite plots from increasing time constant and increasing antenna separation in Figure 3.17 and Figure 3.19 respectively.



**Figure 3.24 – Plot showing data normalized and inverted before and after smoothing filter.**

With the exception of the curve of smallest amplitude (Figure 3.22 far right), no significant change was found between resulting  $Q$  for smoothed and unsmoothed data. In each case, the resulting  $Q$  and BW of the smoothed data set for this curve has been indicated by a different marker. The dashed line indicates possible continuation of the curve for lower values of coupling capacitance considering the smoothed and unsmoothed data points. Unfortunately, this is only what can be predicted as the expected value, since there is insufficient data to conclude how much higher the  $Q$  will rise before tapering off.

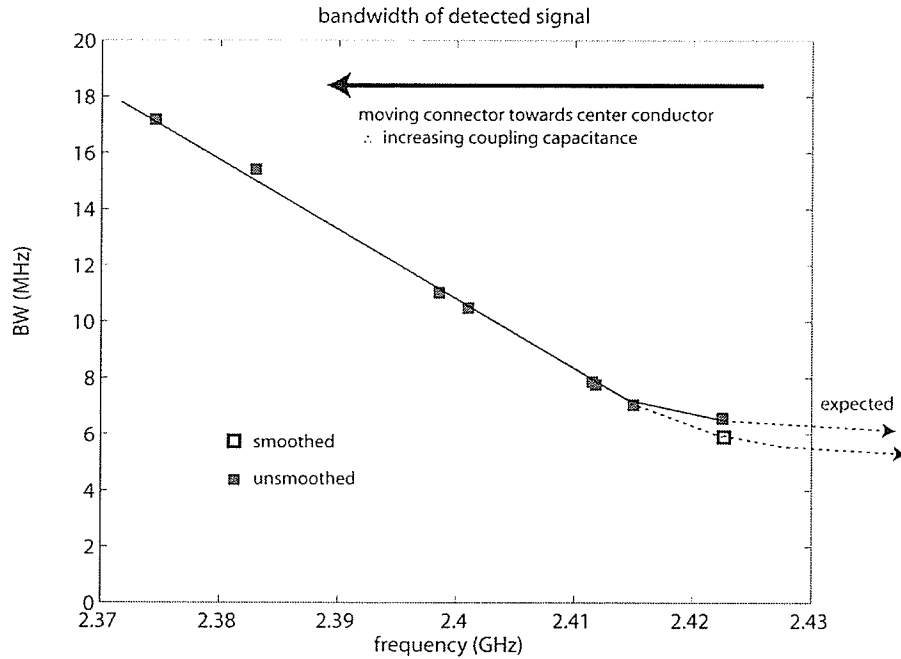


Figure 3.25 – Plot of output bandwidth for pin depth. Frequency decreases with increasing pin depth (increased coupling capacitance).

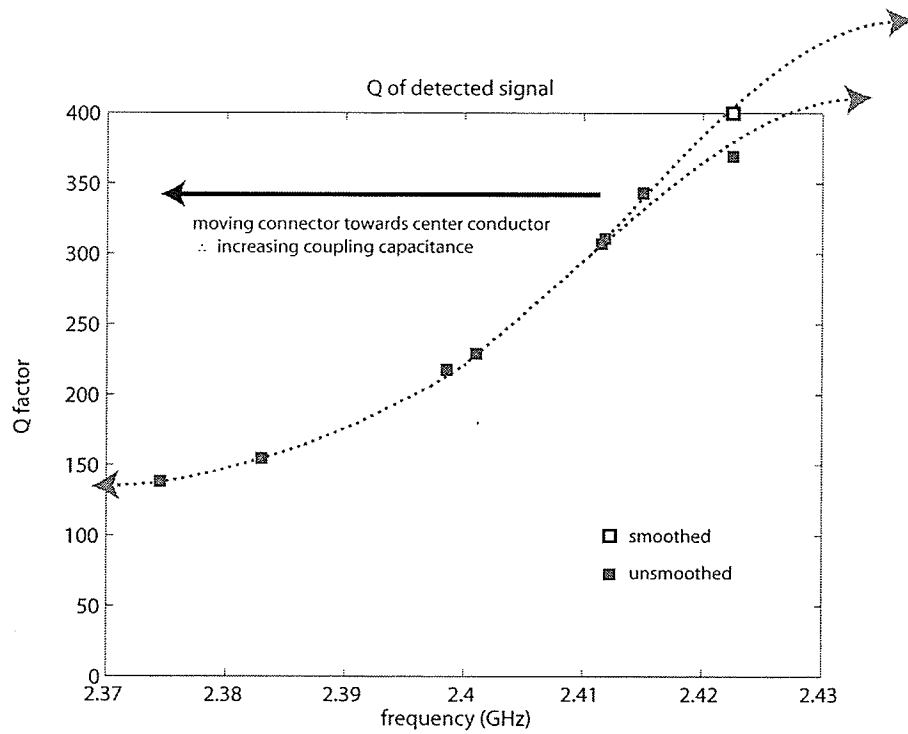
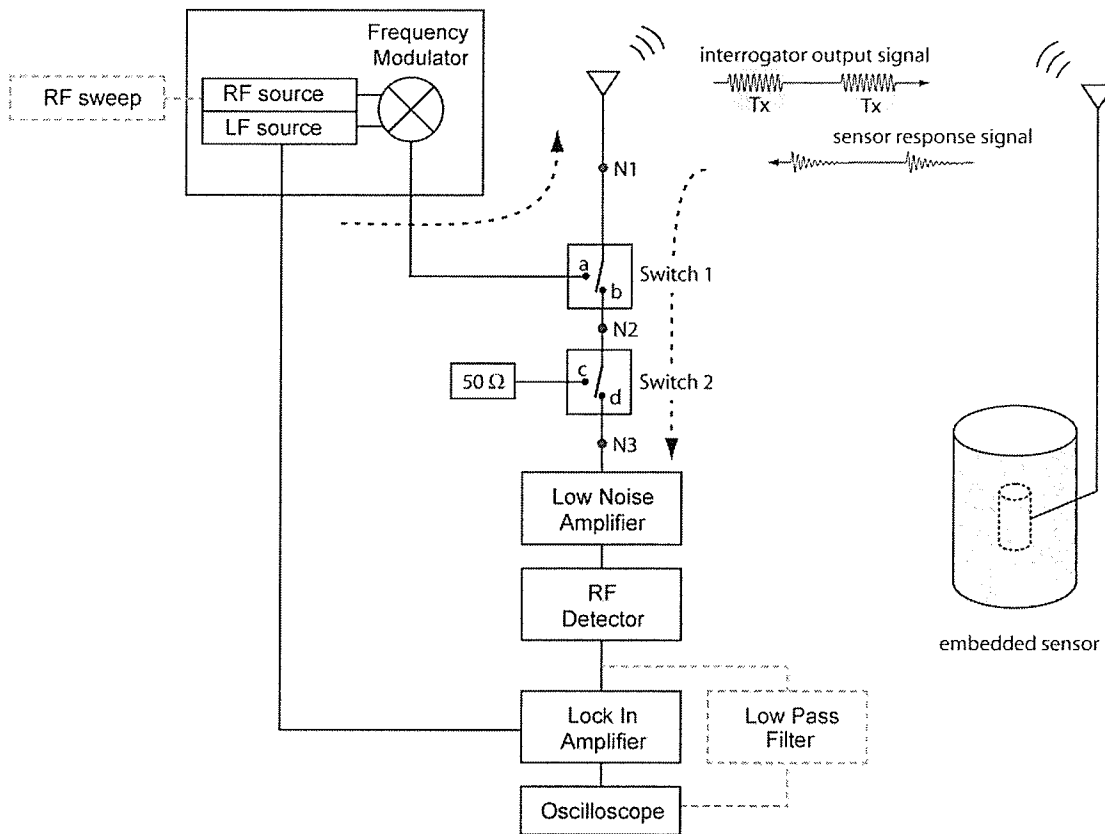


Figure 3.26 – Plot of Q for varying pin depth. Frequency decreases with increasing pin depth (increased coupling capacitance).

From the plot of  $Q$  we can see that the coupling capacitance that results in greatest power in the returned signal does not necessarily imply greatest resonance. Although to date it has been attempted to set the connector to a position where the greatest signal amplitude is detected, it may be desirable to use sensor in undercoupled condition to take advantage of a higher resonance factor. Future work should also include a repetition of this experiment with more data points taken in the undercoupled condition to confirm the limit of  $Q$ .

### ***3.3 Phase Sensitive Detection***

Phase sensitive signal detection techniques were employed to minimize the effects of most types of noise. To do this, a few modifications were made to the basic interrogation system. First, the high frequency signal from the Rhodes & Schwarz signal generator is frequency modulated (FM) with an internally generated low frequency signal. This modulated signal is then transmitted to the sensor through same switch and antenna as used in the basic system. Secondly, when the signal is received, the output of the RF detector is passed into a lock-in amplifier and referenced to the low frequency signal from the Rhodes & Schwarz signal generator. The output of the lock-in amplifier then gives a reading that is proportional to strain. A block diagram of the phase sensitive detection set-up is shown in Figure 3.27.



**Figure 3.27 – Block diagram of the interrogation system modified to use phase sensitive detection techniques using a lock-in amplifier.**

Frequency modulation varies a signal's frequency around a center frequency  $f_{\text{mod}}$ . The amount by which the frequency changes from its center frequency is called the FM deviation. The FM period is the time required to go through one complete deviation cycle, and is the inverse of the FM rate (Figure 3.29). For a square wave FM modulation, the frequency of the signal changes instantaneously between two frequencies  $f_1$  and  $f_2$ . For a sinusoidal FM modulation, the output frequency of a signal follows a sinusoidal pattern between two frequencies  $f_1$  and  $f_2$  (Figure 3.28).

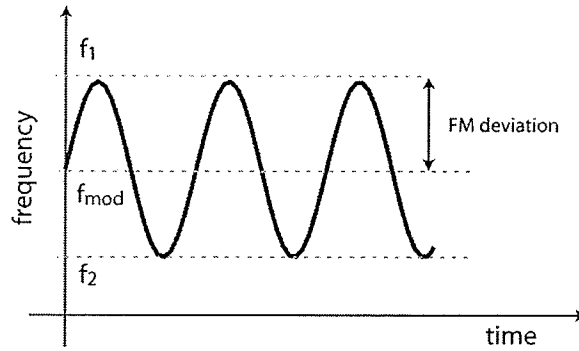


Figure 3.28 – Diagram of sinusoidal frequency modulation.

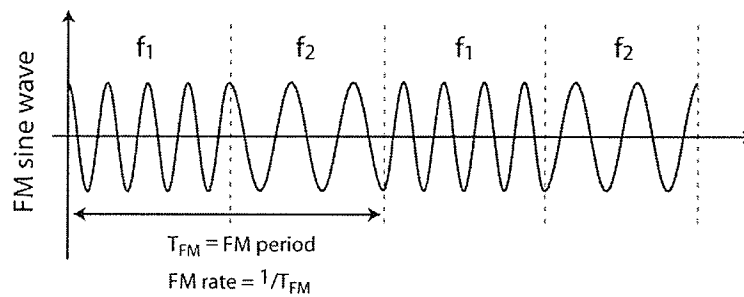


Figure 3.29 – Diagram of FM rate.

In this system, the high frequency signal from the signal generator was frequency modulated at a rate of 15 kHz with a deviation of 2 MHz.

A method of visualizing the function of the lock in amplifier is to first consider the relationship between frequency and the received signal power that describes the sensor response (Figure 3.30). As before, this relationship can be measured from the DC value of the detector output signal when the input frequency is swept over a range of frequencies and will be unique for a given set of operating conditions which include antenna separation distance, time delay, input power and coupling capacitance. Frequency modulation of a signal near the peak of the curve effectively performs a

frequency sweep over the peak as performed before, but this time over a much narrower frequency band (Figure 3.30). Therefore, when a sinusoidal frequency modulation of period  $T=T_{FM}$  is applied to the underlying RF signal, the resulting signal  $f(t)$  in the time domain is a periodic waveform where every point in time corresponds to a point on the power vs. frequency curve (Figure 3.31).

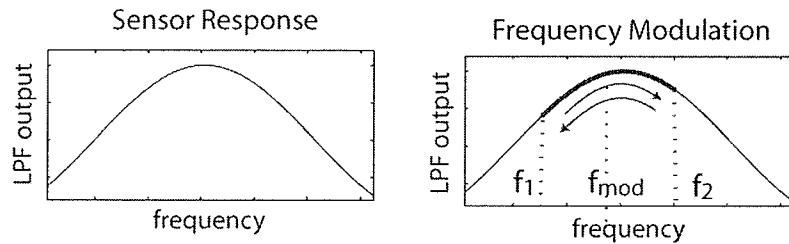


Figure 3.30 – Figure showing frequency modulation effect of detector output through low pass filter.

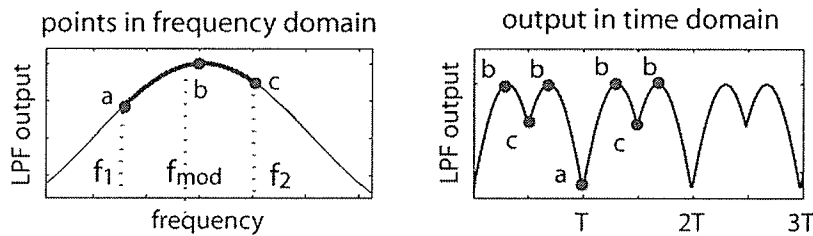


Figure 3.31 – Figure showing time domain output signal of RF detector through low pass filter with FM modulation applied to signal.

Taking the Fourier transform of the time domain signal, we can see the frequency components of the signal  $f(t)$ , where the fundamental frequency is  $f = 1/T$ . This frequency  $f$  is the rate of the FM modulation, and is the frequency of the sinusoidal signal used as the reference signal by the lock-in amplifier.

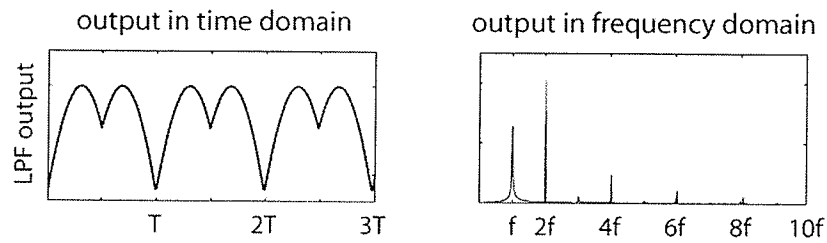
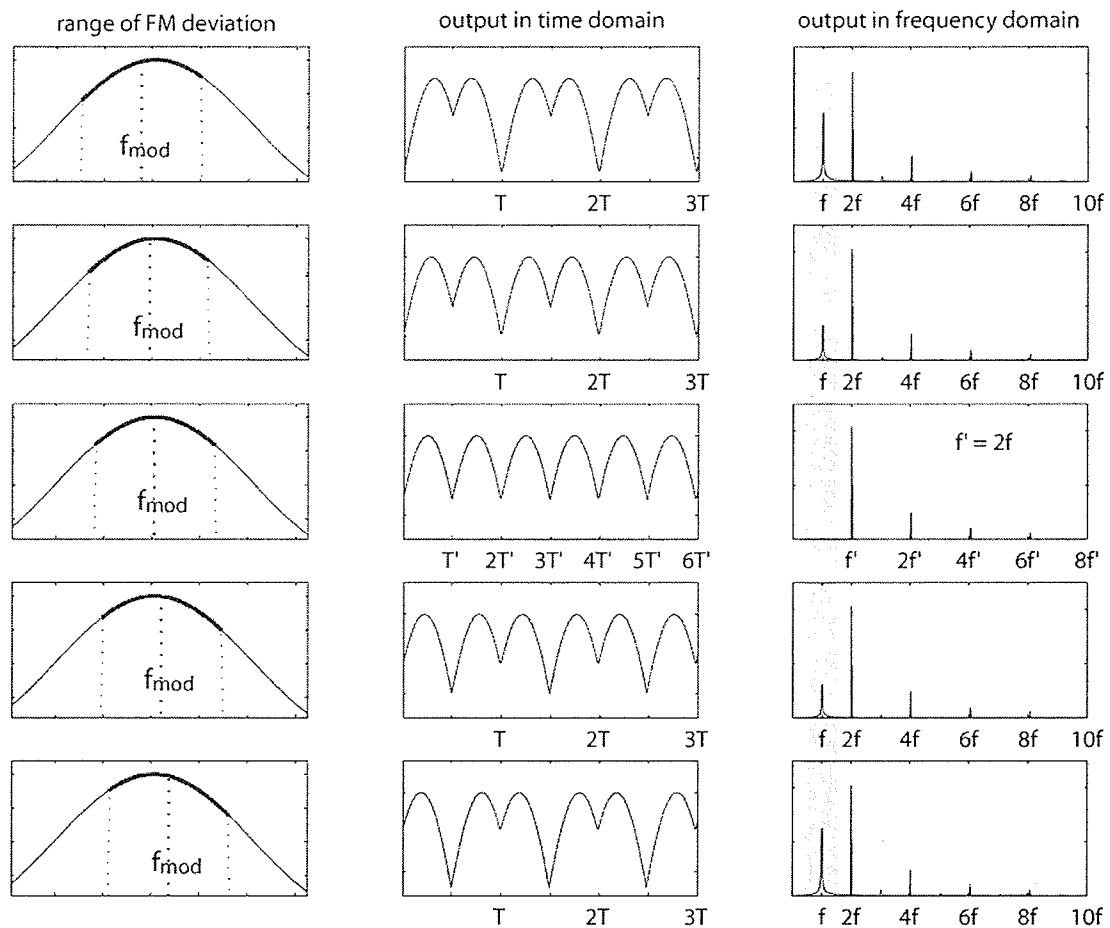


Figure 3.32 – Figure showing frequency spectrum of RF detector signal with FM modulation.

Assuming a fixed sensor response, we can vary the center frequency  $f_{\text{mod}}$  and observe its effects on the output signal and resulting frequency spectrum (Figure 3.33). It can be seen that the low frequency component at frequency  $f$  is minimized when the center of the FM modulated signal is at the resonant frequency of the sensor. When the modulation frequency is perfectly matched at the center frequency of the peak, the time domain output will be a rectified sinusoid signal with a fundamental frequency of  $f' = 2f$ . The frequency spectrum of this signal will compose only of frequency components at multiples of  $2f$ , and no lower frequency components will exist.



**Figure 3.33 – Diagram of changing  $f_{\text{mod}}$  with respect to peak of detector power curve and effects on time domain output of detector and frequency spectrum of output signal.**

Therefore, using phase sensitive detection, when the RF interrogation signal is centered at the resonant frequency  $f_r$ , a signal of 0V is expected at the output of the lock in amplifier since no signal exists at the reference frequency  $f$ . All other values of  $f_{\text{mod}}$  will result in a non-zero values at the output of the lock-in amplifier; where the magnitude of the signal is dictated by the absolute separation of the RF interrogation frequency from the resonant frequency, and the sign of the signal is dictated by their relative positions. For small separations in frequency, the output of the lock-in amplifier is expected to be directly

proportional to the change in frequency between  $f_{\text{mod}}$  and  $f_r$ , and hence the strain in the sensor. This can be shown by plotting the magnitude of the spectral line at  $f$  vs. the center frequency of the modulation  $f_{\text{mod}}$  (Figure 3.34).

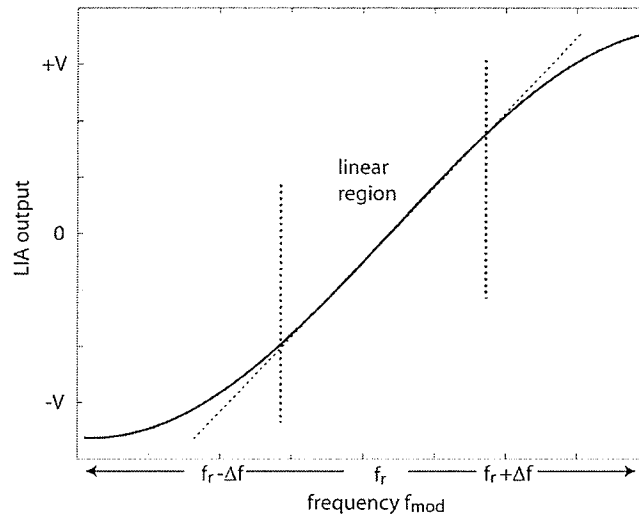


**Figure 3.34 – Figure showing magnitude of low frequency component  $f$  of detector output signals for varying values of  $f_{\text{mod}}$ .**

Typical outputs of the lock-in amplifier and low pass filter signals show reduced noise in the lock in signal. It is clear from the figure that a voltage of 0 volts is expected when the RF input signal passes through the resonant frequency of the sensor, but is non-zero otherwise for frequencies that are close to resonance, therefore to find the resonant frequency is simply a matter of looking for the zero crossing as opposed to a peak frequency.

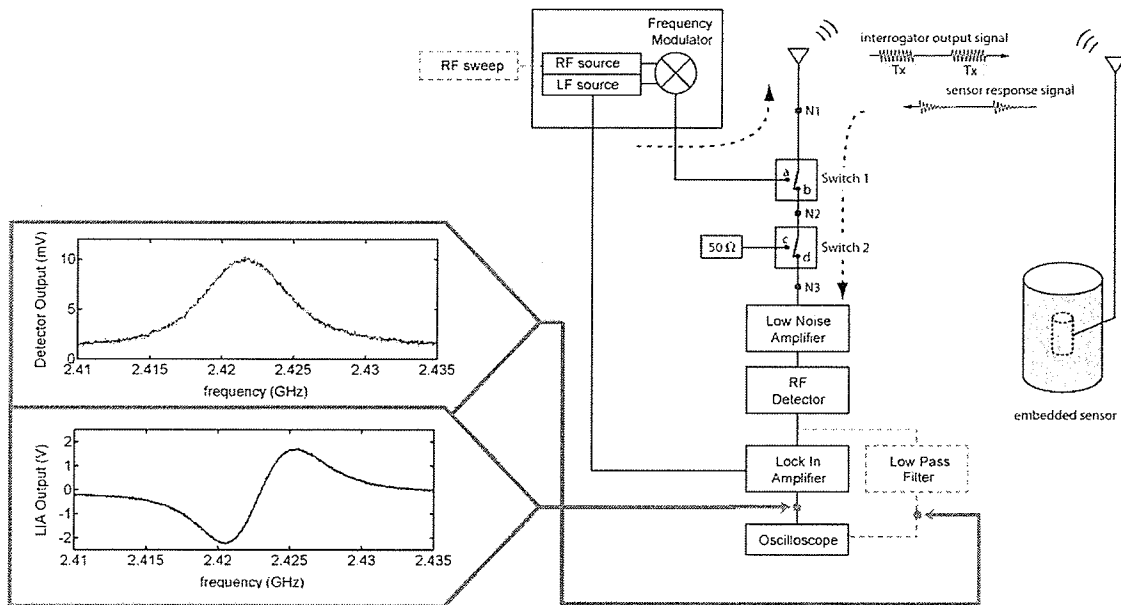


Figure 3.35 – Block diagram showing typical output of low pass filter and lock-in amplifier for a wideband sweep in frequencies.

### 3.3.1 Calculation of System Resolution

The resolution and noise limitations of the phase sensitive detection scheme used can be understood by considering the diagrams in Figure 3.36.

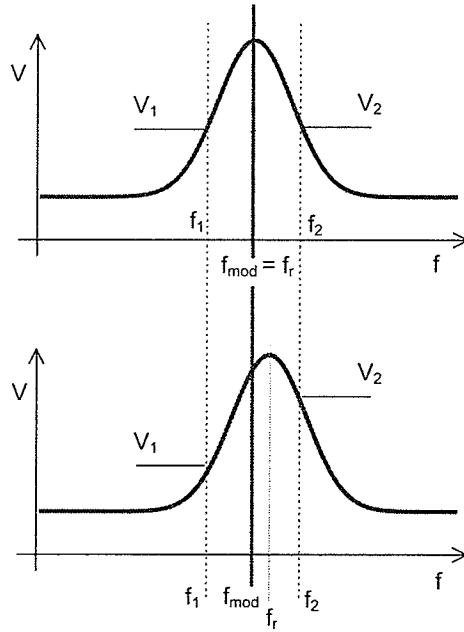


Figure 3.36 – Diagram of square wave frequency modulation on RF signal.

Considering the simplest case, the RF signal is square wave modulated between  $f_1$  and  $f_2$  where:

$$f_r - f_1 = f_2 - f_r \quad (3.5)$$

then assuming a symmetric function around  $f_r$ , the voltage out of the detector at the modulation frequency will be:

$$V|_{f=f_{\text{mod}}} = V|_{f=f_1} - V|_{f=f_2} = 0 \quad (3.6)$$

However, if the resonant frequency is shifted by strain by amount  $\Delta f$ , then the voltage out of the detector at the modulation frequency will be:

$$V_{p-p}|_{f=f_{\text{mod}}} = V_1 + \Delta f \frac{dV_1}{df_1} - \left( V_2 - \Delta f \frac{dV_2}{df_2} \right) \quad (3.7)$$

since the function is symmetrical, for small signals we can write:

$$V_{p-p} \Big|_{f=f_{\text{mod}}} = 2\Delta f \frac{dV}{df} \quad (3.8)$$

since this is square wave modulation the RMS amplitude will be given by:

$$V_{RMS} \Big|_{f=f_{\text{mod}}} = \Delta f \frac{dV}{df} \quad (3.9)$$

Since from Chapter 2 we have:

$$strain = \frac{\Delta h}{h} \approx \frac{\Delta f}{f_r} \quad (2.13)$$

and:

$$\Delta f = strain \times f_r \quad (2.14)$$

we can substitute equation (2.14) into (3.9) and rewrite the equation to get:

$$V_{RMS} \Big|_{f=f_{\text{mod}}} = strain \times f_r \frac{dV}{df} \quad (3.10)$$

$$strain = \frac{V_{RMS} \Big|_{f=f_{\text{mod}}}}{f_r \frac{dV}{df}} \quad (3.11)$$

The resolution of this measurement will be limited by many sources of noise. If we assume that thermal noise from the characteristic impedance of the system is the dominant form of noise, then minimum measurable change in strain will be:

$$\delta strain_{th} = \frac{V_{th}}{f_r \frac{dV}{df}} \quad (3.11b)$$

where  $V_{th}$  is thermal noise signal, and is given by the expression:

$$V_{th} = \sqrt{4kRT(BW)} \times \text{AmpVoltageGain} \quad (3.12)$$

where R is resistance in ohms ( $50\Omega$ ), k is Boltzmann's constant, T is the absolute temperature given in Kelvin, BW is the system bandwidth in Hertz, and AmpVoltageGain is the voltage gain on the low noise amplifier between the switch and the detector.

A theoretical estimate for  $dV/df$  can be derived from Figure 3.36. The peak amplitude of the Gaussian signal can be estimated to be:

$$V_{\max} = V|_{f=f_c} = P_{RF} \times \text{DutyCycle} \times |S_{21}|^2 \times \text{AmpPwrGain} \times \text{ConvFactor} \quad (3.13)$$

where  $P_{RF}$  is the power level of the RF signal, Duty Cycle is the percentage of time that the RF signal is being transmitted from the interrogation system,  $S_{21}$  is the transmission characteristics of the two antennas at the operating frequency, AmpPwrGain is the power gain of the low noise amplifier, and the ConvFactor is the conversion factor of Watts to Volts of the RF detector. For a gaussian shaped peak, the two points of maximal slope on the curve are given by the relationships:

$$\left. \frac{dV}{df} \right|_{x=x_1} = \frac{-V_{\max} 2\sqrt{2\ln(2)}}{FWHM} \exp\left(\frac{-1}{2}\right) \quad (3.14)$$

$$\left. \frac{dV}{df} \right|_{x=x_2} = \frac{+V_{\max} 2\sqrt{2\ln(2)}}{FWHM} \exp\left(\frac{-1}{2}\right) \quad (3.15)$$

For a typical case, this gives:

$$\left. \frac{dV}{df} \right|_{\max} = \frac{10^{-3} W \times .1 \times |.01|^2 \times 1000 W / W \times 200 mV / mW}{2.5 \times 10^6 \text{ Hz}} \times \frac{2\sqrt{2 \ln(2)}}{\exp(1/2)} \quad (3.16)$$

$$\left. \frac{dV}{df} \right|_{\max} = 8 \times 10^{-10} mV / \text{Hz} \times 1.43 = 1.14 mV / \text{MHz} \quad (3.17)$$

For a typical  $dV/df$  of  $1 \text{ mV/MHz}$  at  $f_r = 2.5 \text{ GHz}$ , we find  $\delta \text{strain}_{\text{th}} = 8 \text{ n}\epsilon / \sqrt{\text{Hz}}$ .

### 3.3.2 Measured Resolution

To measure applied strain, the frequency  $f_{\text{mod}}$  can be fixed at one point, and any changes to strain in the sensor would be reflected in the output voltage of the lock-in amplifier. Similarly, by sweeping the input frequency to the sensor and detecting a zero crossing in the output signal, the center frequency can be determined. Under unstrained conditions, this center frequency was determined to be around  $2.42183 \text{ GHz}$ . To simulate the effect of strain, and to estimate the resolution of the system, the input frequency was first set near the resonant frequency by adjusting the input frequency until the output of the lock-in was near zero. A step of  $100 \text{ kHz}$  was then made on the input frequency to the sensor from the RF source with the sensor with no change in strain conditions. To the lock-in amplifier, this effectively reproduces the same separation of frequencies as driving the sensor at a constant frequency while the device is subject to a strain of approximately  $40 \mu\epsilon$ . This measurement was performed with both the ungated and the gated switch configurations (Figure 3.37).

For the ungated (one switch) case, a  $100 \text{ kHz}$  shift in frequency produced a change of  $\sim 440 \text{ mV}$  in the output, giving a conversion ratio of approximately  $11 \text{ mV} / \mu\epsilon$ . Peak to

peak noise is approximately 50 mV, corresponding to a resolution limit of 4.5  $\mu\epsilon$ . RMS noise is 10 mV, giving a RMS resolution limit of better than 1  $\mu\epsilon$ . For the gated (two switch) case, a 100 kHz step produced approximately 260 mV change in the output signal. This corresponds to a conversion ratio of 6.5 mV/ $\mu\epsilon$ . Peak to peak noise is ~14 mV, corresponding to a resolution limit of 2.15  $\mu\epsilon$ . RMS noise was found to be ~2.5 mV giving a resolution limit of less than .5  $\mu\epsilon$ . SNR is ~18 using peak to peak noise, and 144 using RMS noise values. This is still considerably larger than the thermal noise limit and is believed to be due to environmental noise but may also be due to frequency variation in the RF source. The results of this measurement can be found summarized in .

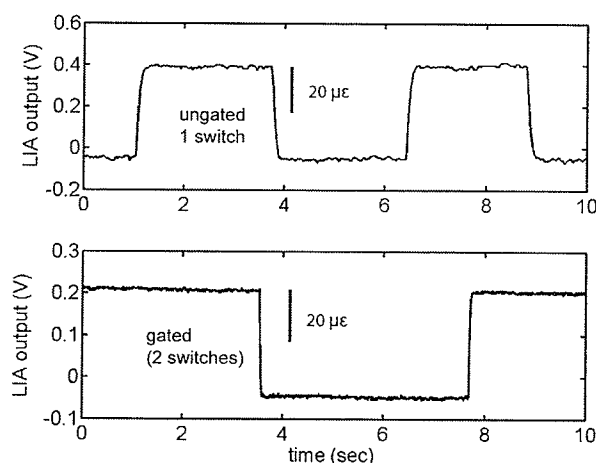


**Figure 3.37 – Plot of lock-in amplifier output with 100 kHz steps in input RF frequency. Gated system showing much lower signal level, but improved signal to noise ratio.**

	$\Delta V$ per 100 kHz	Conversion Ratio	Peak to Peak Noise	SNR	RMS Noise	SNR
1 Switch	440 mV	11 mV/ $\mu\epsilon$	50 mV = 4.5 $\mu\epsilon$	8.8	10 mV = .9 $\mu\epsilon$	44
2 Switches	260 mV	6.5 mV/ $\mu\epsilon$	14 mV = 2.2 $\mu\epsilon$	18	2.5 mV = .5 $\mu\epsilon$	144

**Table 3.1 – Summary of calibration test for lock-in output with 100 kHz steps in input frequency.**

Background noise levels of the system were measured against varying time constants on the lock in amplifier (Figure 3.38). As expected, total noise levels increase with increases in bandwidth. It can be seen that the RMS noise level falls below  $1 \mu\epsilon$  for  $\tau$  equal to or greater than 30 ms.

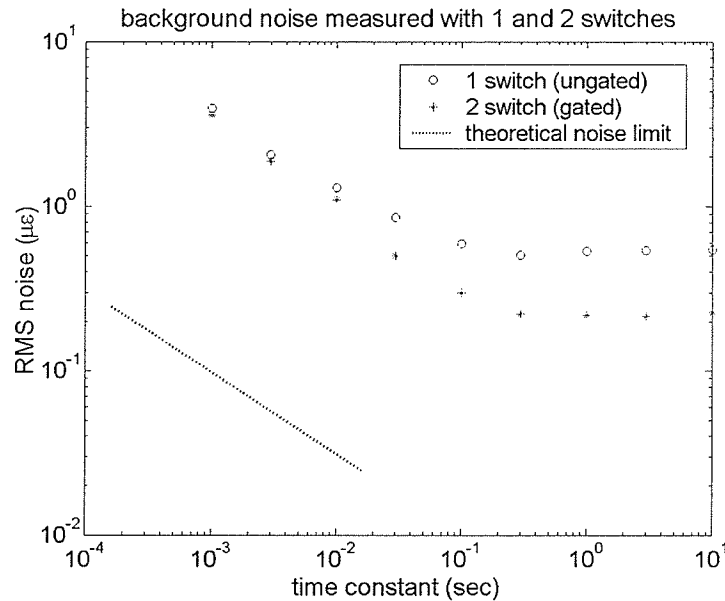


Figure 3.38 – Plot of background noise measurement vs. time constant on lock-in amplifier with theoretical noise limits.

Although signal to noise in the present example are adequate for many purposes, they are still above thermal noise limits as indicated in the plot. This implies that improvements in bandwidth, and hence minimum measurement time required can theoretically be obtained. Reducing measurement time is necessary if this system is to be feasible for measurements from a vehicle moving at highway speeds. However, before this is possible, the exact nature and magnitude of the noise sources will need to be studied, and will be the focus of future work.

### 3.4 Results from Compression Test

To validate the strain measuring capabilities of the interrogation system, a load frame was again used to apply a compressive force to the concrete cylinder and strain the concrete cylinder and embedded sensor (Figure 3.39).

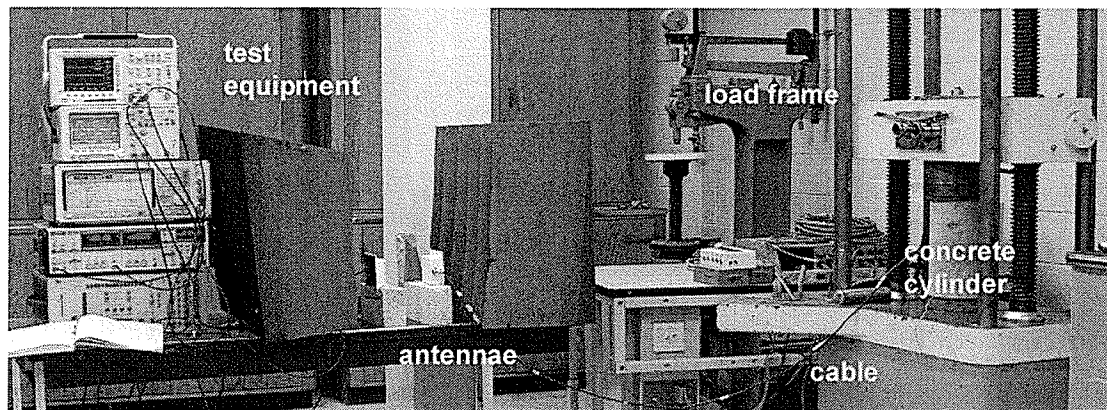
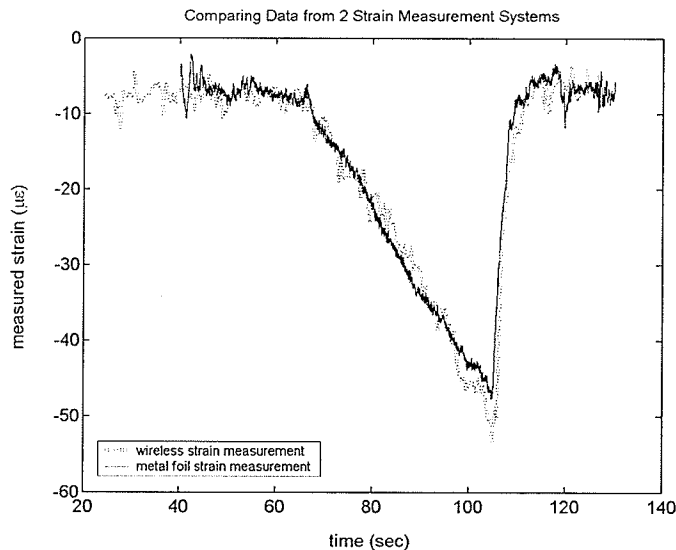


Figure 3.39 – Photograph of equipment set up for compressive load test of sensor with measurements obtained using wireless interrogation system.

This time the measurements were taken with the interrogation system rather than with the network analyzer. A cable extension connected the sensor embedded in the concrete cylinder to the receiving antenna. Absorbing foam was placed around the two communicating antenna to isolate them from environmental effects. Using an oscilloscope, the output of the lock-in amplifier was recorded onto floppy disks for post processing and analysis. Strain measurements were also simultaneously obtained from a metal foil strain gauge applied on the outside of the concrete cylinder as a reference measurement of applied strain through a data acquisition system. Strain measurements were obtained by cycling in compressive strain. Tests were performed with a steady ramp up of strain at varying rates with an abrupt release in pressure. Typical measurements

from the two measurements show good agreement between the shape and scaling. To compare the results on the same scale, the output voltage from the lock in amplifier was converted to a strain measurement by applying two scaling factors. First, to convert from voltage to the equivalent frequency shift (260 mV/100 kHz as calibrated above), and then by applying the expected relationship between strain the frequency shift (2.42 kHz/microstrain) as determined by Equation 2.14 in Chapter 2. In some cases, the resulting curve was translated to be aligned with the plot of metal foil strain data. Comparing the strain measured by the metal foil strain gauge and the output of the lock in amplifier, we can see that there is good agreement between the measured values as they show consistency in shape and do not diverge greatly from one another (Figure 3.40).



**Figure 3.40 – Plot showing typical output from the lock-in amplifier and metal foil strain gauge plotted together showing good agreement between measurements (negative values indicate compressive strain).**

Plotting the measured values of strain against the corresponding measured value from the interrogation system, we get a best fit line with a slope of .94 (Figure 3.41). We expect to see a slope of 1 for perfect agreement between the two. However, this may be explained by the fact that the two sensors are measuring strain in different materials (brass vs. concrete) and in different places in the cylinder (center vs. external wall). To determine if this is the case, the experiment should be repeated with a metal foil strain sensor applied directly to the side of the sensor cavity as well as on the side of the concrete cylinder to determine if there is any difference in strain in the two locations and/or materials as an additional gauge factor may be necessary to accurately determine strain.

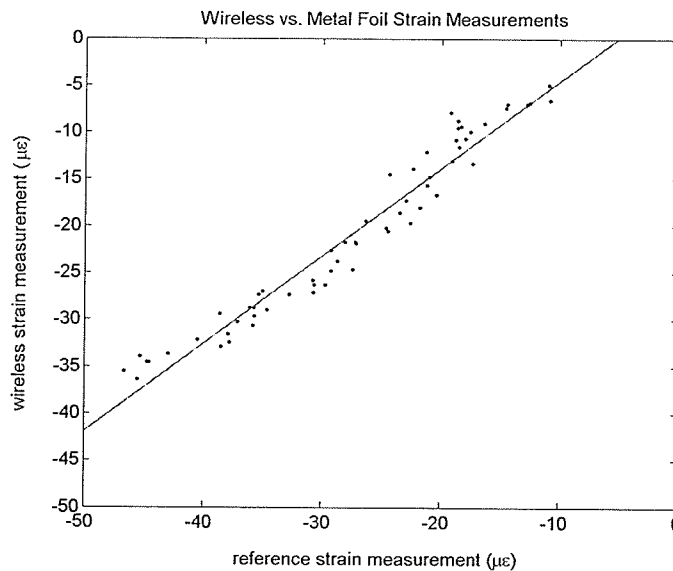


**Figure 3.41 – Plot of strain measurement from wireless interrogation system plotted vs. metal foil strain gauge measurement.**

### **3.5 Chapter Summary**

In this chapter, a basic interrogation system for wirelessly determining the strain in a resonant cavity sensor was described. In section 3.2 reduction of environmental reflections and noise through the use of time domain gating were discussed and demonstrated. With gating in place, the effects of varying gating time, antenna separation distance, and coupling capacitance were investigated and fit to with expected relationships showing good agreement. It was shown that the amplitude of the received signal decreased with increasing antenna separation at a rate proportional to  $x^{-4}$ , therefore having significant implications in the limitations in system range. As well, a measure of the cavity  $Q$  was assessed with the obtained data. Although the  $Q$  measured in this chapter did not agree with value of  $Q$  obtained in Chapter 2, it was determined that  $S_{11}$  is not a very good measure of the cavity's resonance as the obtained values for  $S_{11}$  signal bandwidth clearly do not match with the ringdown time from the lumped element model of a resonant transmission line, nor does it match with the measured results of decaying signal amplitude with varying time constant. Section 3.3 presented phase sensitive signal detection with a theoretical basis for its use, calculations of resolution and background noise limits, as well as measured results showing resolution of better than  $1 \mu\epsilon$ . A description of the wireless interrogation system as used in compressive strain tests was presented in section 3.4 showing good agreement between data from metal foil strain sensors and those obtained from the wireless system.

## Chapter 4      Conclusions and Future Work

The purpose of this thesis was to investigate a novel strain measuring system for use in civil Structural Health Monitoring (SHM) applications. To that end, a wireless strain sensor and associated interrogation system has been presented. This sensor presented is a metal coaxial cavity that is robust, inexpensive to manufacture, and easy to install and use.

Chapter 1 presented the state of current strain sensors for civil SHM purposes, as well as the need to improve on their utility through improved robustness, cost effectiveness, ease of installation, and ease of use. The major flaws of current sensing systems being the time consuming and labour intensive installation procedure, as well as necessity for a physical connection between sensors and their respective interrogation systems. This is problematic because it is costly and disruptive to the construction process. As well, the presence of data carrying cables in the concrete complicates any subsequent maintenance.

As well, a review of current wireless sensing technologies was presented detailing their methodology, applications, and potential weaknesses for use in civil structures. A brief overview of the strain sensor investigated in this thesis was then presented as a potential solution to developing cost effective solutions for strain monitoring systems appropriate for use in civil applications.

In Chapter 2, a theoretical basis for the sensor's operation was presented along with circuit modeling to describe the sensor's behaviour to parameters such as input frequency and coupling capacitance. It was found that the general transmission line equations can be used to obtain a reasonable approximation of the sensor's frequency response, however, there are additional losses in the system which are not considered in the model. To get a closer representation of the measured data, the distributed parameter R in the model was augmented by a factor of 2.5. An equivalent lumped element model of the transmission line was also presented – giving a calculated theoretical Q factor of the cavity of approximately 680.

At the end of the chapter, a brief explanation was given for how the sensor would be installed and used in concrete structures. As a test of the sensor's response to strain, a sensor embedded in concrete, and measurements of the resonant frequency vs. applied were obtained. These measurements were referenced to those obtained from a metal foil strain gauge, and demonstrated high linearity with low hysteresis up to 200  $\mu\epsilon$ .

Chapter 3, presented the basic interrogation system necessary to interrogate the sensor and determine the resonant frequency. It was observed that the effects of environmental reflections caused considerable distortion in the output signals. This then led to the addition of time domain gating which improved the output considerably. It was found that a time delay of approximately 8 ns was sufficient to reduce additive noise. Although initially this noise was believed to be due to environmental reflections, it may also be due

to effects of RF pass through in the switch, or caused by resonance in the antennas used in the experiment. These factors need to be further investigated to fully understand their effect.

Measuring the decay time on the time domain signals from the detector, we found time constants of 55 ns and 37 ns for the cavity signal and noise effects respectively. Effects of changing the time delay of the gating, gave an exponential decay with a time constant of approximately 22 ns. This difference requires further investigation as it can not be adequately explained at this time. The time constant of 22 ns corresponds to a Q of 334 which was considerably lower than the theoretical Q presented in Chapter 2. From this, it could be concluded that although the bandwidth of the  $S_{11}$  curve gave a clear indication of where the feed was best matched to the sensor cavity, it did not give a very reasonable approximation of Q as a measure of the cavity's ability to store energy of a particular frequency. It was shown experimentally that increasing coupling capacitance has the effect of decreasing Q of the resonant system. Therefore, it was found that although maximum signal strength is obtained at critical coupling, it may be worth investing the use of the sensor in the undercoupled condition.

Observing the effects of varying separation distance between the antenna for the interrogation system and the antenna for the sensor, it was found that the power actually decreases proportionally to  $x^{-4}$ . This is because the signal is transmitted and received with an attenuation factor of  $x^{-2}$  in both directions. This has significant consequence for the

design requirements regarding maximum separation distance, minimum power output of the interrogator, and antenna gain.

Phase sensitive detection using a frequency modulated input signal and a lock in amplifier was also detailed. Experimental results show a strain resolution of better than 1  $\mu\epsilon$  resolution with a bandwidth of 30 Hz. However, background noise levels were measured and found to be well above the theoretical noise limits calculated, implying that the necessary measurement time can be decreased. As well, through phase sensitive detection, improvements in signal to noise ratio were shown with the use of a gated detection network over an ungated network despite a severe reduction in received power.

As well, results of compressive strain on the sensor using the phase sensitive interrogation system demonstrated good agreement with results obtained with a metal foil strain gauge. Clearly there exists the potential for this device to be a viable alternative to current strain sensors for civil applications of structural health monitoring.

#### ***4.1 Recommendations for Future Work***

It is recommended that future research in this area include:

1. A thorough analysis of noise sources and methods of attaining levels closer to theoretical noise limits.
2. Improvements in the circuit model with representations of other losses and parasitic effects to better represent measured data.

3. Further investigate the source of signal distortion without second switch including effects of switching time in the switches, and antenna resonance.
4. Reconcile difference in time constant as measured from the time domain signal and from the maximum amplitude of signals with varying time delay between switches. In the former, we measure a time constant of approximately 55 ns, in the latter a time constant of approximately 22 ns.
5. Perform measurements for  $\Delta f_{\text{res}}$  vs. strain with a metal foil strain sensor applied to the outside of the resonant cavity as well as on the outside of the concrete cylinder to get a better measure of what effects are occurring.
6. Repeat strain measurements with a sensor set in the undercoupled condition to see if improved Q improves signal to noise at the output.
7. Implement peak detection algorithms to improve accuracy of detection of resonant frequency.
8. Development of an antenna for use with the embedded sensor.

## References

1. Frangopol, D. M., "New Directions and Research Needs in Life-Cycle Performance and Cost of Civil Infrastructures", Proc. 4th International Workshop on SHM, Stanford, DESTech Pub, Sept 15 – 17, 2003, pp 53 – 63.
2. Wang, J. Y., "Local Damage Detection of Bridges Using Signals of Strain Measurements", Proc. 1st International Conference SHMII, Tokyo, Nov. 13 – 15, 2003, A. A. Balkema Pub., pp 1081 – 1088.
3. Carkhuff, B.; Cain, R., "Corrosion sensors for concrete bridges", IEEE Instrumentation & Measurement Magazine, Volume: 6, Issue: 2, June 2003, pp 19 – 24.
4. Liu, S.C., Tomizuka, M., "Vision Strategy for Sensors and Smart Structures Technology Research" Proc. 4th International Workshop on SHM, Stanford, DESTech Pub, Sept 15 – 17, 2003, pp 42 – 52.
5. Kinawi, H.; Taha, M.M.R.; El-Sheimy, N. "Structural health monitoring using the semantic wireless: a novel application for wireless networking", Local Computer Networks, 2002. Proceedings. LCN 2002. 27th Annual IEEE Conference on, 6-8 Nov. 2002, pp 770 – 778.
6. Harichandran, R. S., "EIS-based NDE of bond integrity in concrete bridges strengthened with CFRP", Proc. 1st International Conference SHMII, Tokyo, Nov. 13 – 15, 2003, A. A. Balkema Pub., pp 1183 – 1190.
7. Elgamal, A., Conte, J. P., Masri, S., Fraser, M., Fountain, T., Gupta, A., Trivedi, M., El Zarki, M., "Health Monitoring Framework for Bridges and Civil Infrastructure" Proc. 4th International Workshop on SHM, Stanford, DESTech Pub, Sept 15 – 17, 2003, pp 123 – 130.
8. Chase, S., Ghasemi, H., "A Vision for Highway Bridges for the 21st Century" Proc. 4th International Workshop on SHM, Stanford, DESTech Pub, Sept 15 – 17, 2003, pp 205 – 213.
9. Inaudi, D., "State of the Art in Fiber Optic Sensing Technology and EU Structural Health Monitoring Projects", Proc. 1st International Conference SHMII, Tokyo, Nov. 13 – 15, 2003, A. A. Balkema Pub., pp 191 – 198.
10. Yun, Chung Bang, "Recent R&D Activities on Structural Health Monitoring for Civil Infra-Structures in Korea", International Workshop on Advanced Sensors, Structural Health Monitoring, and Smart Structures, 10-11 November 2003.

11. P. Thomson, J. Marulanda C., J. Marulanda A, J. M. Caicedo, "Real-time health monitoring of civil infrastructure systems in Colombia", Proceedings of the 6th Annual International Symposium on NDE for Health Monitoring and Diagnostics, Newport Beach, California, March 4-8, 2001.
12. Inada, H., Ishii, K., "Application of Carbon Fiber Sensor for Monitoring Damage to Concrete Piles", Proc. 1st International Conference SHMII, Tokyo, Nov. 13 – 15, 2003, A. A. Balkema Pub., pp 1287 – 1294.
13. Wu, Z. S., "Structural Health Monitoring and Intelligent Infrastructures in Japan", Proc. 1st International Conference SHMII, Tokyo, Nov. 13 – 15, 2003, A. A. Balkema Pub., pp 153 – 167.
14. Ito, S., Onishi, H., Matsui, S., Okuno, M., "Study on Monitoring of Deterioration of RC slab with Optical Fiber", Proc. 1st International Conference SHMII, Tokyo, Nov. 13 – 15, 2003, A. A. Balkema Pub., pp 247 – 251.
15. Wenzel, H., "E-MOI – European Monitoring Initiative", Proc. 1st International Conference SHMII, Tokyo, Nov. 13 – 15, 2003, A. A. Balkema Pub., pp 145 – 152.
16. Ou, J. P., "Some Recent Advances in Intelligent Health Monitoring Systems for Civil Infrastructure in Mainland China", Proc. 1st International Conference SHMII, Tokyo, Nov. 13 – 15, 2003, A. A. Balkema Pub., pp 131 – 144.
17. Wang, C. Y., Wang, H-L., Wu, C-Y., Chen, C-H., "Development of bridge health monitoring systems in Taiwan", Proc. 1st International Conference SHMII, Tokyo, Nov. 13 – 15, 2003, A. A. Balkema Pub., pp 1067 – 1072.
18. Brownjohn, J.M.W., "Lessons from Monitoring the Performance of Highway Bridges", International Workshop on Advanced Sensors, Structural Health Monitoring, and Smart Structures, 10-11 November 2003.
19. Liu, D. H., Jin, W. L., Shao, J. W., "Applying Brillouin Health Monitoring Network for Civil Engineering", Proc. 1st International Conference SHMII, Tokyo, Nov. 13 – 15, 2003, A. A. Balkema Pub., pp 237 – 240.
20. Measures, R. M., M. M. Ohn, S. Y. Huang, J. Bigue, N. Y. Fan, 1998. "Tunable Laser Demodulation of Various Fiber Bragg Grating Sensing Modalities", Smart Mater. Struct., 7 No 2 (April 1998): 237-247.
21. Inaudi, D., S. Vurpillot, N. Casanova, P. Kronenberg, 1998. "Structural Monitoring by Curvature Analysis Using Interferometric Fiber Optic Sensors", Smart Mater. Struct., 7 No 2 (April 1998): 199-208.
22. Tennyson, R. C., A. A Mufti, S. Rizkalla, G. Tadros, B. Benmokrane, 2001, "Structural Health Monitoring of Innovative Bridges in Canada with Fiber Optic Sensors", Smart Mater. Struct., 10 No 3 (June 2001): 560-573.

23. Doyle, C., Staveley, C., Henderson, P., "Structural Health Monitoring Using Optical Fibre Strain Sensing System", Proc. 4th International Workshop on SHM, Stanford, DEStech Pub, Sept 15 – 17, 2003, pp 944 – 951.
24. Xia, Y., Aoki, S., Abe, M., Fujino, Y., "A Remote Intelligent Monitoring System (RIMS) for Infrastructures", Proc. 1st International Conference SHMII, Tokyo, Nov. 13 – 15, 2003, A. A. Balkema Pub., pp 359 – 363.
25. Omega Process Measurement and Control:  
[<http://www.omega.com/literature/transactions/volume3/strain.html>]
26. Wang, D.H.; Liao, W.H.; "Instrumentation of a Wireless Transmission System for Health Monitoring of Large Infrastructures", Instrumentation and Measurement Technology Conference, 2001. IMTC 2001. Proceedings of the 18th IEEE , Volume: 1 , 21-23 May 2001, pp 634 – 639.
27. Robbins, A. H., Millar, W. C., Circuit Analysis Theory and Practice, Delmar Publishers, 1995, pp 297 – 304.
28. Dewang Chen; Xiaoyan Gong; Changqing Zheng, "A wireless traffic information collection system in Beijing urban freeways" Intelligent Transportation Systems, 2002. Proc. IEEE 5th International Conference on , 2002, pp 387 – 391.
29. Wang, A.; Chandrakasan, A., "Energy-efficient DSPs for wireless sensor networks" Signal Processing Magazine, IEEE , Volume: 19 , Issue: 4 , July 2002, pp 68 – 78.
30. Chamberland, J.-F.; Veeravalli, V.V., "Decentralized detection in sensor networks", Signal Processing, IEEE Transactions on, Volume: 51 , Issue: 2 , Feb. 2003 pp 407 – 416.
31. Vieira, M.A.M.; Coelho, C.N., Jr.; da Silva, D.C., Jr.; da Mata, J.M. "Survey on wireless sensor network devices", Emerging Technologies and Factory Automation, 2003. Proceedings. ETFA '03. IEEE Conference , Volume: 1 , 16-19 Sept. 2003, pp 537 – 544.
32. Jerome P. Lynch, Arvind Sundararajan, Kincho H. Law, Anne S. Kiremidjian, Thomas W. Kenny, and Ed Carryer (2003), "Embedment of Structural Monitoring Algorithms in a Wireless Sensing Unit," Structural Engineering and Mechanics, Techno Press, 15(3): 285-297.
33. Mason, A.; Yazdi, N.; Chavan, A.V.; Najafi, K.; Wise, K.D., "A generic multielement microsystem for portable wireless applications", Proceedings of the IEEE , Volume: 86 , Issue: 8 , Aug. 1998, pp 1733 – 1746.
34. Raghunathan, V.; Schurgers, C.; Sung Park; Srivastava, M.B., 2002, "Energy-aware wireless microsensor networks" Signal Processing Magazine, IEEE , Volume: 19 , Issue: 2 , March 2002, pp 40 – 50.
35. Bult, K.; Burstein, A.; Chang, D.; Dong, M.; Fielding, M.; Kruglick, E.; Ho, J.; Lin, F.; Lin, T.H.; Kaiser, W.J.; Marcy, H.; Mukai, R.; Nelson, P.; Newburg, F.L.; Pister, K.S.J.; Pottie, G.; Sanchez, H.; Sohrabi, K.; Stafsudd, O.M.; Tan, K.B.; Yung, G.; Xue, S.; Yao, J., "Low power systems for

- wireless microsensors”, *Low Power Electronics and Design*, 1996., International Symposium on , 12-14 Aug. 1996, pp 17 – 21.
36. Roundy, S., Wright, P. K., and Rabaey, J., 2003. “A Study of Low Level Vibrations as a Power Source for Wireless Sensor Nodes”, *Computer Communications*, vol. 26, no. 11, pp 1131 – 1144.
  37. University of California Berkeley - Office of Technology Licensing, *Technology Business Opportunity: Non-Confidential Disclosure, Ambient Vibration-Based Power Generator*, (UCB Case No.: B04-046)
  38. Lonsdale, A., “Dynamic Rotary Torque Measurement Using Surface Acoustic Waves” *Sensor Magazine*, October 2001  
[<http://www.sensorsmag.com/articles/1001/51/main.shtml>]
  39. Kwok, H. L., *Electronic Materials*, PWS Publishing Company, Boston, 1997, pp 124, 378
  40. Solymar, Walsh, *Lectures on the Electrical Properties of Materials*, Oxford Science Publications, 5th Edition, 1993, pg 283.
  41. Reindl, L. M., “Wireless Passive SAW Identification Marks and Sensors”, *IEEE Ultrasonics, Ferroelectrics, and Frequency Control Society Tutorial*  
[<http://www.ieee-uffc.org/fcmain.asp?view=review#tutor>]  
[[http://www.ieee-uffc.org/freqcontrol/tutorials/Reindl\\_2002\\_files/frame.htm](http://www.ieee-uffc.org/freqcontrol/tutorials/Reindl_2002_files/frame.htm)]
  42. Drafts, B., “Acoustic Wave Technology Sensors”, *Sensor Magazine*, October 2000  
[<http://www.sensorsmag.com/articles/1000/68/main.shtml>]
  43. Transense Technologies  
<http://www.transense.co.uk/physics.html>
  44. Hautamaki, C., Zurn, S., Mantell, S., Polla, D., “Experimental Evaluation of MEMs Strain Sensors Embedded in Composites”, *Journal of Microelectromechanical Systems*, Vol 8, No. 3, September, 1999, pp 272 – 279.
  45. Varadan, V. K., Varadan, V. V., “Microsensors, Microelectromechanical Systems (MEMS), and Electronics for Smart Structures and Systems”, *Smart Mater. Struct.* 9, IOP publishing, (2000), pp 953 – 972.
  46. Jain, M., Cai, Q., Grimes, C., “A wireless micro-sensor for simultaneous measurement of pH, temperature, and pressure” *Smart Mater. Struct.* 10, IOP publishing, (2001), pp 347 – 353.
  47. Bulst, W., Fischerauer, G., “State of the Art in Wireless Sensing with Surface Acoustic Waves”, *IEEE Trans. Industrial Electronics*, Vol. 48, No. 2, April 2001, pp 265 – 271.
  48. Varadan, V. V., Varadan, V. K., Bao, X., Ramanathan, S., Piscotty, D., “Wireless passive IDT strain microsensor”, *Smart Mater. Struct.* 6, IOP publishing, (1997), pp 745 – 751.
  49. Seifert, F., Pohl, A., Steindl, R., Reindl, L., Vellekoop, M. J., Jakoby, B., “Wirelessly Interrogable Acoustic Sensors”, 1999 Joint Meeting EFTF – IEEE IFCS, pp 1012 – 1018.

50. Grossmann, R., Michel, J., Sachs, T., Schrufer, E., "Measurement of Mechanical Quantities Using Quartz Crystals", European Frequency Time Forum, March 5-7 1996, Conference Publication No 418, pp 376 – 381.
51. Cheng, W., Dong, Y., Feng, G., "A Multi-Resolution Wireless Force Sensing System Based upon a Passive SAW Device", IEEE Trans. Ultrasonics, Ferroelectrics, and Frequency Control, Vol. 48, No. 5, September 2001, pp 1438 – 1441.
52. Varadan, V. K., Teo, P. T., Jose, K. A., Varadan, V. V., "Design and development of a smart wireless system for passive temperature sensors", Smart Mater. Struct. 9, IOP publishing, (2000), pp 379 – 388.
53. Schimetta, G., "A Wireless Pressure-Measurement System Using a SAW Hybrid Sensor", IEEE Trans. Microwave Theory and Techniques, Vol. 48, No. 12, December 2000, pp 2730 – 2735.
54. Fischerauer, G., "Surface Acoustic Wave Devices," in: W. Göpel, J. Hesse, J. N. Zemel, H. Meixner, R. Jones (Eds.), Sensors. A Comprehensive Survey, Vol. 8. Weinheim: VCH, 1995.
55. Hayt, W. H., Kemmerly, J. E., Engineering Circuit Analysis, McGraw-Hill Book Company Inc., New York, 1962, pp. 481 – 506.
56. Butler, J. C., Vigliotti, A. J., Verdi, F. W., Walsh, S. M., "Wireless, passive, resonant-circuit, inductively coupled strain sensor", Sensors and Actuators A 102 (2002), pp 61 – 66.
57. Ong, K. G., Grimes, C. A., Robbins, C. L., Singh, R. S., "Design and application of a wireless, passive, resonant-circuit environmental monitoring system", Sensors and Actuators A 92 (2001), pp 33 – 43.
58. Akar, O., Akin, T., Najafi, K., "A wireless batch sealed absolute capacitive pressure sensor", Sensors and Actuators A 95 (2001), pp 29 – 38.
59. Todoroki, A., Miyatani, S., Shimamura, Y., "Wireless strain monitoring using electrical capacitance change of tire: part II - passive", Smart Mater. Struct. 12, IOP publishing, (2003), pp 410 – 416.
60. Stanford Research Systems SC10 High Stability Ovenized 10 MHz Quartz Oscillator Datasheet  
<http://www.srsys.com/html/sc10.html>  
<http://www.srsys.com/html/sc10specs.html>
61. Feynman, R. P., Leighton, R. B., Sands, M., The Feynman Lectures on Physics, Mainly Mechanics, Radiation and Heat, Addison Wesley Publishing Company, Reading Massachusetts, 1963, 1977, Chapter 23 -25.
62. Serway, R. A., Physics for Scientists and Engineers, 3rd edition, Saunders College Publishing, 1992, pp 341 – 345, 478 – 490.
63. Pozar, D. M., Microwave Engineering, John Wiley & Sons, Inc, New York, 1998, pp, 1, 56 – 69, 87-94, 104 – 146, 258, 259, 300 – 323, 332 – 336.

64. Sadiku, M. O., Elements of Electromagnetics, Oxford University Press, 2001, 3rd edition, pp. 410 – 428, 473 – 489, 576.
65. Dorf, R. C., Svoboda, J. A., Introduction to Electric Circuits, 3rd Edition, John Wiley and Sons, 1996, pp 429 – 468, pp 650 – 654.
66. Toselli, A., “Some Results on Schwarz Methods for a Low Frequency Approximation of Time Dependent Maxwell's Equations in Conductive Media”, Contemporary Mathematics, Volume 218, Contemporary Mathematics, Volume 218, 1998.  
[<http://www.ams.org/conm/218/articles/B0-8218-0988-1-03053-3.pdf>]
67. Transmission line diagram  
<http://www.sm.luth.se/~urban/master/Theory/4.html>
68. Integrated Publishing – Navy NEETS modules online  
[<http://www.tpub.com/content/neets/14182/>]
69. Institute for Telecommunication Sciences (R and D branch of National Telecommunications and Information Administration(NTIA), part of the U.S. Department of Commerce (DOC))  
[http://www.its.bldrdoc.gov/fs-1037/dir-015/\\_2167.htm](http://www.its.bldrdoc.gov/fs-1037/dir-015/_2167.htm)

## Appendix A

appendix\_coupling\_cap\_lossyTLine.txt

Values of Coupling Capacitance used to generate curves in nominal lossy t-line model

Coupling Capacitance in model for each trace (starting at lowest value = RHS):

```
>> CC'  
ans =  
1.0e-012 *  
0.004000000000000  
0.007000000000000  
0.010000000000000  
0.013000000000000  
0.016000000000000  
0.019000000000000  
0.022000000000000  
0.025000000000000  
0.027000000000000  
0.029000000000000  
0.031000000000000  
0.033000000000000  
0.035000000000000 <-- Critical Coupling Point  
0.037000000000000  
0.039000000000000  
0.041000000000000  
0.043000000000000  
0.045000000000000  
0.047000000000000  
0.049000000000000  
0.052000000000000  
0.055000000000000  
0.058000000000000  
0.061000000000000  
0.066000000000000  
0.071000000000000  
0.076000000000000  
0.081000000000000  
0.086000000000000  
0.091000000000000  
0.096000000000000  
0.101000000000000  
0.106000000000000
```

>>

Per unit length capacitance

>> C

C =

5.056884592371320e-011

>>

appendix\_coupling\_cap\_augR.txt

Values of Coupling Capacitance used to generate curves in augmented R model

Coupling Capacitance in model for each trace (starting at lowest value = RHS):

```
>> CC'  
ans =  
1.0e-012 *  
0.0240000000000000  
0.0270000000000000  
0.0300000000000000  
0.0330000000000000  
0.0360000000000000  
0.0390000000000000  
0.0420000000000000  
0.0450000000000000  
0.0470000000000000  
0.0490000000000000  
0.0510000000000000  
0.0530000000000000  
0.0550000000000000 <-- Critical Coupling Point  
0.0570000000000000  
0.0590000000000000  
0.0610000000000000  
0.0630000000000000  
0.0650000000000000  
0.0670000000000000  
0.0690000000000000  
0.0720000000000000  
0.0750000000000000  
0.0780000000000000  
0.0810000000000000  
0.0860000000000000  
0.0910000000000000  
0.0960000000000000  
0.1010000000000000  
0.1060000000000000  
0.1110000000000000  
0.1160000000000000  
0.1210000000000000  
0.1260000000000000
```

```
>>  
Per unit length capacitance  
>> C  
C =  
5.056884592371320e-011  
>>
```